DESKTOP GENERATED MICROPLANAR X-RAY BEAMS AND THEIR BIOLOGICAL EFFECTS

Soha Bazyar

A dissertation submitted to the faculty at the University of North Carolina at Chapel Hill in partial fulfillment of the requirements for the degree of doctor of philosophy in the joint department of biomedical engineering in the North Carolina State University and the University of North Carolina at Chapel Hill.

Chapel Hill
2018

Approved By:

Yueh Z. Lee

Otto Zhou

David Lalush

Joel E. Tepper

Maureen Su

ABSTRACT

Soha Bazyar: Desktop Generated Microplanar X-ray Beams and Their Biological Effects
(Under the direction of Yueh Z. Lee)

Cancer affects 1 in 2 men and 1 in 3 women in the US and about half of all cancer patients receive some type of radiation therapy sometime during the course of their treatment. Normal tissue toxicity is the most important dose-limiting side effect of radiotherapy. This effect not only occurs after conventional broad beam radiotherapy (BB) but also following new radiation modalities namely, intensity modulated radiotherapy and proton therapy.

Microbeam radiotherapy (MRT) is a novel preclinical approach for radiotherapy, which delivers spatially fractionated submillimeter lines of the collimated quasi-parallel of a single high-dose (100Gy<) radiation (peaks), separated by wider nonirradiated regions (valleys). Interestingly, the preclinical studies on animal models have consistently demonstrated the selective tumoricidal effect of MRT with the ability to even cure the aggressive orthotopic tumor models while sparing the normal tissue.

Most of the MRT studies have been conducted in spars synchrotron facilities around the world. To make this technology more available for preclinical biomedical studies and facilitate the translation of this promising modality to the clinic, here a desktop approach for applying MRT has been sought. My dissertation goal was to develop a more accessible microbeam approach, study its effectiveness and evaluate some of the hypothetical underlying radiobiological mechanism of the desktop MRT approach.

In this work, the effect of MRT and BB on normal mouse brain will be first evaluated using battery of neurocognitive tests, up to 8-months post irradiation. Next, a novel method for applying microbeams using an industrial cabinet animal irradiator will be introduced and a detailed description of its final characteristics will be given, including a comprehensive evaluation of the treatment geometry and a full-scale phantom-based quantification of its dosimetric output. Subsequently, the *in vitro* and *in vivo* efficacy of this new approach will be investigated. Later, the role of the acquired immune system will be evaluated in the tumor response after MRT. Finally, future project directions will be described briefly. Based on the results of this work, the author's belief that our approach for applying MRT can be easily reproduced in other research facilities for radiobiological research and has definite clinical translation potential.

To my best friend and my husband Ali. I couldn't have done this without you.

To my mentor Dr. Yueh Z. Lee who believed in me. Thank you for your endless support along the way.

ACKNOWLEDGMENTS:

First, I would like to thank my graduate advisors, Drs. Yueh Z. Lee, Otto Zhou, Joel E. Tepper, Maureen Su and David Lalush. Without their inspiration, support and trust in me none of this work would have been possible.

Next, I would like to thank the entirety of the Zhou Group in the University of North Carolina at Chapel Hill (UNC-CH) Physics Department for their help during this project, in particular, Dr. Jianping Lu and Ms. Christina Inscoe. The foundations for this work is the groundbreaking research of those in this group that came before me, specially Drs. Michael John Hadsell, Lei Zhang and Pavel Chtcheprove. I am incredibly grateful for the opportunity to follow their leads.

I wish to acknowledge the support of different groups and people at the UNC-CH who contributed directly to my research: to Drs. Timothy E. O'Brien and Elaine M. Zeman for all of their support, kindness and devotion to my own education; to Drs. C. Ryan Miller and Robert S. McNeil at UNC Translational Neuro-oncology Laboratory and Dr. Pearl Bakhru at Su Lab for their generous help and guidance with the cells culture; to the Animal Histopathology & Lab Medicine Core and Translational Pathology Laboratory staff for their help in preparing, scanning, and interpretation of the histology slides; to the Physics Shop and Makerspace staff for making the mouse holder, shielding and Barns Maze platforms; to the staff at the Division of Laboratory Animal Studies at Marsico Hall, Animal Studies Core and Tissue Culture Facility at Lineberger Comprehensive Cancer Center for their assistance throughout *in vivo*

studies; to Mark Bruckner at Environmental Health department for his collaboration during dosimetry evaluation.

I am so grateful of UNC-CH mouse behavioral phenotype core continuous support during neurocognitive studies.

I wish to acknowledge the great work of Drs. Otto Zhou and Sha Change for developing the 1st generation of carbon-nanotube based desktop mirobeam irradiator, US Patent No.: US8,600,003B2, that was utilized during neurocognitive studies.

Finally, and most importantly, I would like to appreciate the continuous encourage and support of my family, to my parents, Aliasghar and Mansoureh Bazyar, who thought me the value of hard working and to my sister, Sahar, who showed me how to enjoy the most difficult moments, and to love of my life, my husband, Ali. Because of him I had the courage to apply for PhD in an engineering field. I am truly thankful of him for all sacrifices he made during our adventurous life journey.

TABLE OF CONTENTS

LIST OF FIGURES

LIST OF TABLES

LIST OF ABBREVIATIONS AND SYMBOLS

ANOVA = Analysis of Variance

APC = Antigen Presenting Cell

BB = Conventional Broad Beam Radiotherapy

CNT = Carbon-nanotube X-ray Technology

CRT = Conventional Radiation

CTL = Cytotoxic Lymphocyte

ED50 = Dose of a Treatment Observed to Yield Half-Maximal Efficacy

FSD = Focus-Surface Distance

FWHM = Full Width Half Maximum

HLA = Human Leukocyte Antigen

HVL_{Al} = Aluminum Half-Value-Layer

IACUC = Institutional Animal Care and Use Committee

IF = Immunofluorescence

IMRT = Intensity Modulated Radiotherapy

IP = Intraperitoneal

MHC = Major Histocompatibility Complex

MRT = Microbeam Radiotherapy

NK cell = Natural Killer Cells

PDD = Percentage Dose Drop

PVDR = Peak-to-Valley Dose Ratio

RBED = Radiobiological Equivalent Dose

RT = Radiation Therapy

SF = Surviving Fraction

SC = Subcutaneous

TCR = T-cell Receptor

TD50 = Dose of a Treatment Observed to Yield Half-Maximal Toxicity.

TH = Helper T-cells

Treg = Regulatory T-cell

UNC-CH = The University of North Carolina at Chapel Hill

CHAPTER 1 INTRODUCTION

1.1 Background:

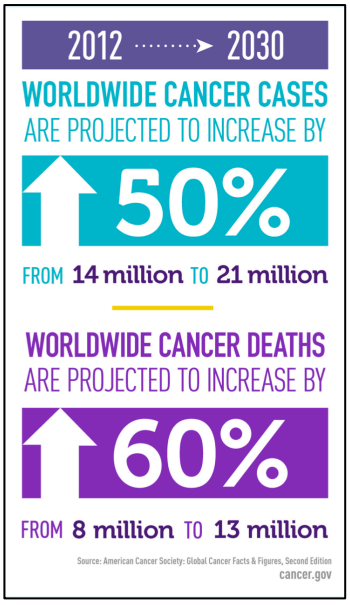

Figure 1-1: Cancer statistics and facts

Despite tremendous breakthrough discoveries in the field of cancer treatment during the last century, an estimated 1,735,350 new cases of cancer will be diagnosed and 609,640 people will die from this disease, in 2018 in US alone[1] (Fig 1-1). Approximately, 50 percent of all cancer patients will benefit from radiotherapy (RT) sometimes during their course of treatment[2]. Consequently, RT remains the most widely utilized treatment modality in the clinical management of cancer and any enhancement in the efficacy of this treatment modality will benefit a large number of patients. RT deposits significant energy in the target tissue, which damages the DNA of cells either directly or indirectly through the formation of free radicals (Fig 1-2).

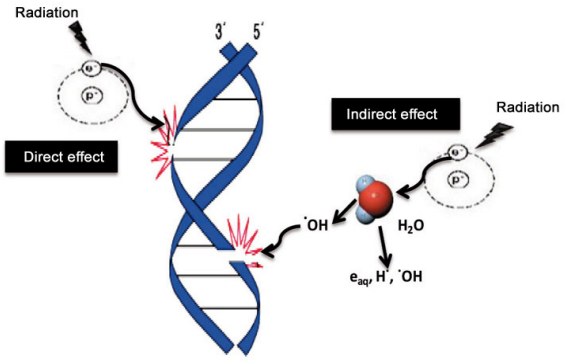

Figure 1-2: The illustration of direct and indirect effect of ionizing radiation on DNA

Cells whose DNA is damaged beyond repair stop dividing or die. Extensive studies pioneered by Bergonié and Tribondeau (1960) have shown that the

most sensitive cells to RT are those that are undifferentiated, rapidly dividing and highly active metabolically. As a result, the cancer cells are more sensitive to the effects of RT. Unfortunately, RT does not only destroy the cancer cells, but it may also damage the normal cells (Fig 1-3). Therefore, although increasing the dose of radiation increases the degree of tumor control, normal tissue toxicity becomes the major confounding limitation. The type, severity and clinical presentation of the toxic side effects from RT depend on the area of the body being treated, the dose given per day, the total dose given, the patient's general medical condition, and other treatments given at the same time. For instance, therapeutic doses of radiation to the brain almost always produces some level of side-effects, ranging from headache to cognitive dysfunction to frank brain necrosis.

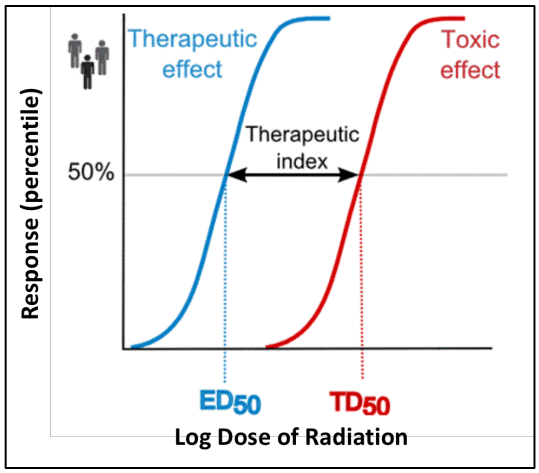

Figure 1-3: The dose-response curve for the radiation therapy.

During last few decade, efforts have been made to optimize the therapeutic index of RT (Fig 1-3). Temporal fractionation was one of the initial major advances in side effect reduction. It is based on the ability of normal tissue to repair sub-lethal damages between sequential treatments. Lately, modern technologies enabled the application of the more advanced modalities namely intensity modulated RT (IMRT), image guided RT and stereotactic RT, all of which have significantly reduced the dose derived to tumors adjacent tissue. However, most recent studies have demonstrated that even advanced modalities like IMRT and proton therapy can damage the healthy tissue [3]. As a result, further improvements are needed.

1.2 What is MRT?

More than 50 years ago, a study by Zeman et al. revealed a surprising fact that formed the principle idea of microbeam radiotherapy. These researchers observed that the deposition of over 4000Gy by single-particle, high-energy beams of heavy ions over a 25μm path caused no tissue damage in mouse brain cortex. Radiating 1mm of the same tissue with only 7% of this dose caused massive tissue necrosis (Fig 1-4)[4]. In 1992, researchers at Synchrotron Light Source of Brookhaven National Laboratory, Upton, NY exploited these

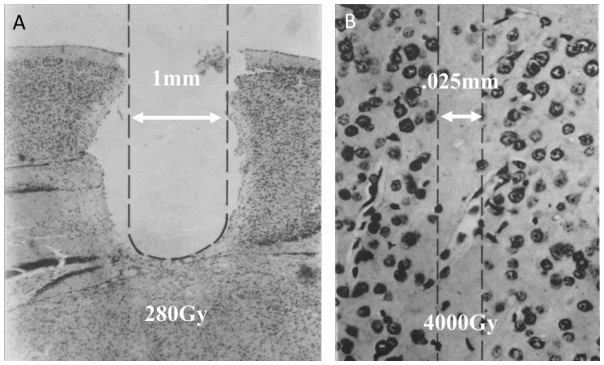

Figure 1-5: A: Cystic cavitation of tissue along the beam path; B: Complete loss of cell bodies along the beam path while the normal tissue has maintained its integrity.

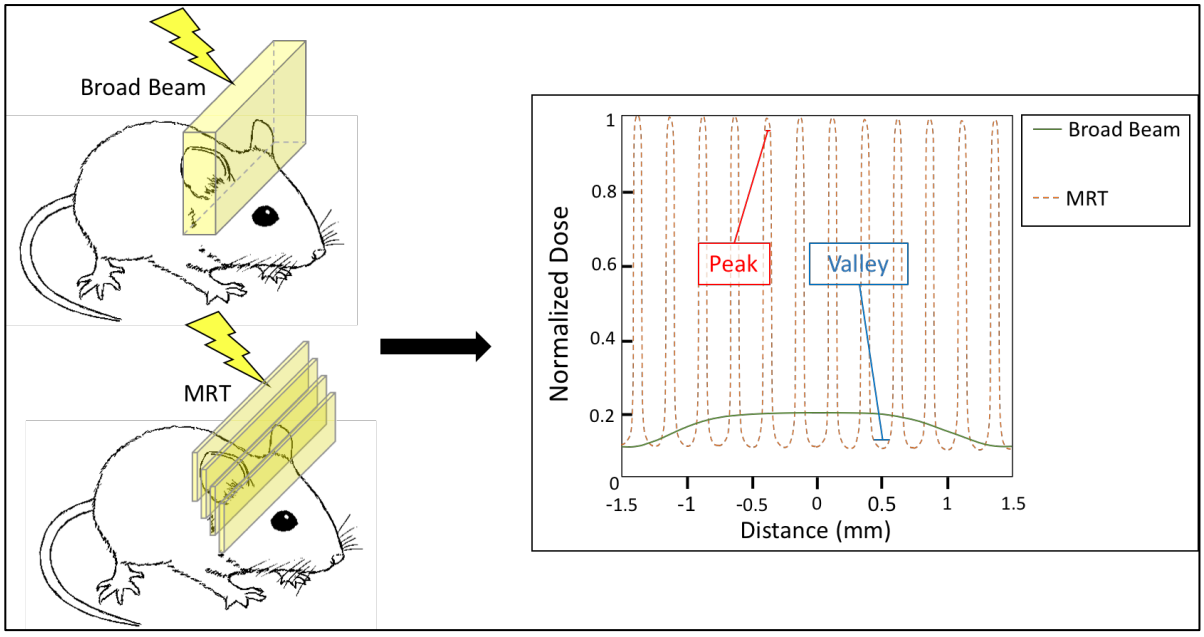

Figure 1-4: Schematic picture of conventional broad beam radiation therapy (BB) versus spatially fractionated microbeam radiation therapy (MRT). In BB, a homogeneous single dose of irradiation is delivered to the target (top mouse and continuous line in the graph), while in MRT, a single high dose of irradiation deposits in micrometer beams (peak) that are separated by non-irradiated regions (valley) (bottom mouse and dashed line in the graph).

findings and used a multi slit collimator to convert synchrotron light source to 25µm microbeam. They denominated this method "Microbeam radiation therapy" or MRT[5].

In contrast to conventional radiation which delivers a spatially homogenous radiation dose to the target, MRT is an array of ultra-high dose (in magnitude of hundreds of Gy) of micrometer (under 1mm; usually <200µm) quasi-parallel beams, which generate 'peaks'. These beams are separated by wider not directly irradiated regions (two to four times wider than peak), referred to as 'valley' (Fig 1-5). Although in MRT most of the tissue that are placed in the valley area would only receive scattered dose, preclinical studies have consistently demonstrated that tumor control or cure can be achieved, even in radioresistant orthotopic murine models of cancers (Fig 1-6) [6–8].

Furthermore, the tolerance of normal tissues to this type of irradiation has been observed in several preclinical experiments. For instance, the tolerance of normal tissues to MRT was surprisingly high in the rat skin [9], fast-growing immature tissues such as the duck brain *in ovo*[10], the chick chorioallantoic membrane [11], the cerebella of normal, suckling rat pups[12], as well as adult rat and mouse brains[6,13–15] and in normal weanling piglet cerebella[16–18] (Fig 1-7).

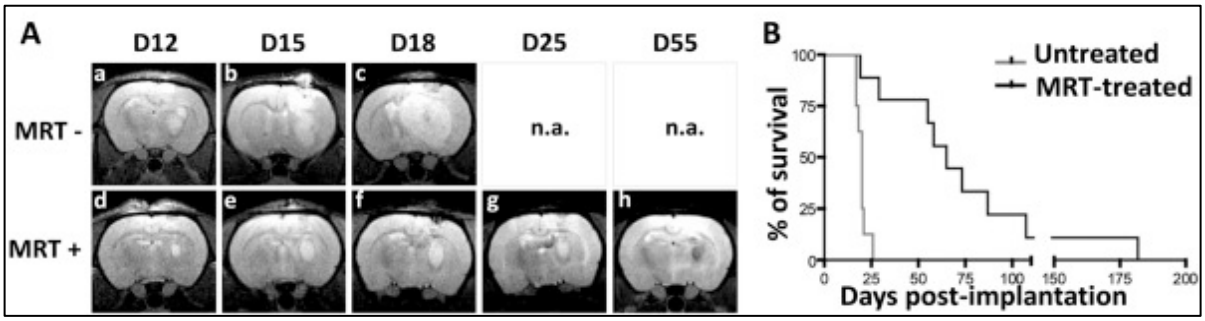

Figure 1-6: Effects of synchrotron MRT on rats bearing an orthotopic 9GLS tumor. Brain tumor growth control and increase in rat survival. A: T2-weighted MR imaging follow-up illustrates the evolution of the lesion size: untreated (a–c) or treated by MRT (d–h). B: Kaplan Meier curves showing the survival of 9LGS tumor bearing rats. Untreated controls are represented in grey, while animals treated by MRT are plotted in black. MRT induced a significant increase in the median survival time of animals (D65 versus D20, log rank test, p=0.0003).

1.3 Synchrotron based MRT studies?

Since the 1990s, MRT has been vastly implemented and studied at third generation synchrotron sources mainly the European Synchrotron Radiation Facility (ESRF), in Grenoble, France. There are multiple technical reasons that make the synchrotron sources most suitable for applying microbeams:

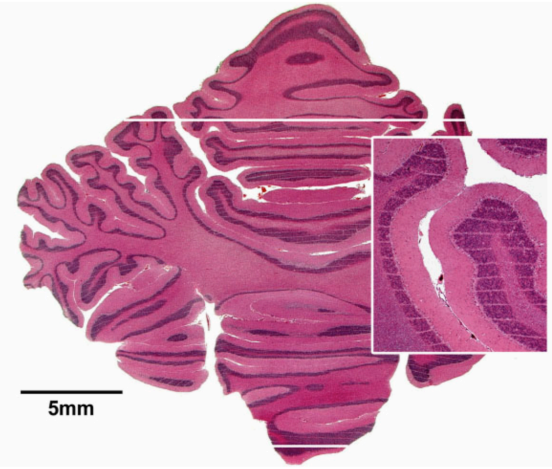

Figure 1-7: Cerebellum of a piglet ~15 months after irradiation (skin entrance dose: 300 Gy), stained horizontal tissue section. The tissue maintains its normal architecture. The thin white horizontal parallel stripes, clearly visible in the inset, correspond to the paths of the microbeams; the beam spacing was ~210 μm. Two thick white horizontal lines show the anteroposterior limits of the array of microplanes.

1. The goal microbeam width during the synchrotron studies was typically less than 100μm. To maintain the beam separation of the microbeams deep in the tissue, orthovoltage X-ray energies are used instead of megavoltage. As shown in Fig 1-8, at megavoltage energy the amount of energy deposition by secondary electrons is high, which would increase the valley dose and diminish the narrow penumbra of the beams. At kilovoltage energies, in conventional irradiators, X-ray production occurs through Bremsstrahlung radiation, resulting in more than 99% of the electrons depositing their energy as heat at the anode, which lowers the potential dose rate of conventional X-ray tubes. In synchrotron sources, X-ray is generated by inserting devices called wigglers into the electron beam storage ring that cause the electrons to oscillate under the influence of a varying magnetic field[19,20]. The output of these wigglers is typically a spectrum of X- rays that has a median and maximum energy of around 100keV and 600keV,

respectively[21]. All of the X-ray photons are compressed into a field with a tiny angle. Consequently, synchrotron sources are able to generate orthovoltage X-ray beams at the rate of hundreds of Gy per second.

2. During the microbeam treatment, even a slight motion (mm or less), would smear the peak and valley doses. This problem would arise not only from the gross movement of the subject, but also due to physiological motion of the target tissue. For instance, even the brain experiences a few mm of motion under normal cardiac and respiratory pulsation. The ultra-high dose rate of synchrotron sources could limit the total duration of radiation and, consequently, the chance of motion.

3. Conventional irradiators, in contrast to synchrotron sources, generate divergent X-ray photons. Based upon the definition of MRT as quasi parallel micrometer X-ray beams, industrial irradiators are generally considered inappropriate source for applying MRT, unless significant collimation is applied, that further limits the dose rate.

1.4 Constraints of synchrotron microbeam radiation therapy:

As described previously, the use of synchrotron radiation to implement MRT is seemingly ideal, but it has also hindered the translation of this interesting modality to the clinic. Most of the studies of this novel modality have been limited to the four 3rd generation synchrotron laboratories around the world, and currently only two of them actively run microbeam studies. The limited availability minimized the potential for other groups to replicate studies. Furthermore, there are considerable cost and safety roadblocks to clinical implementation. Methods for estimating absolute dosimetry are also limited, having been based almost entirely on simulation.

It has not been shown conclusively in radiobiological studies that the ultra-high dose rates at synchrotron sites are necessary for successful treatment. The high dose rate, although decreasing the chance of smearing of the beam at the fixed target, results in the potential for high dose deposition within the valleys and creating a homogenous radiation field after even a slight motion.

1.5 Aims:

To step beyond the limitations synchrotron sources introduced to the field, the overarching goal of my dissertation was to develop a compact MRT treatment approach to allow implementation in physical, radiobiological and preclinical research. The following are the crucial steps that will guide technical development and alongside these developments, facilitate the appropriate clinical application of MRT:

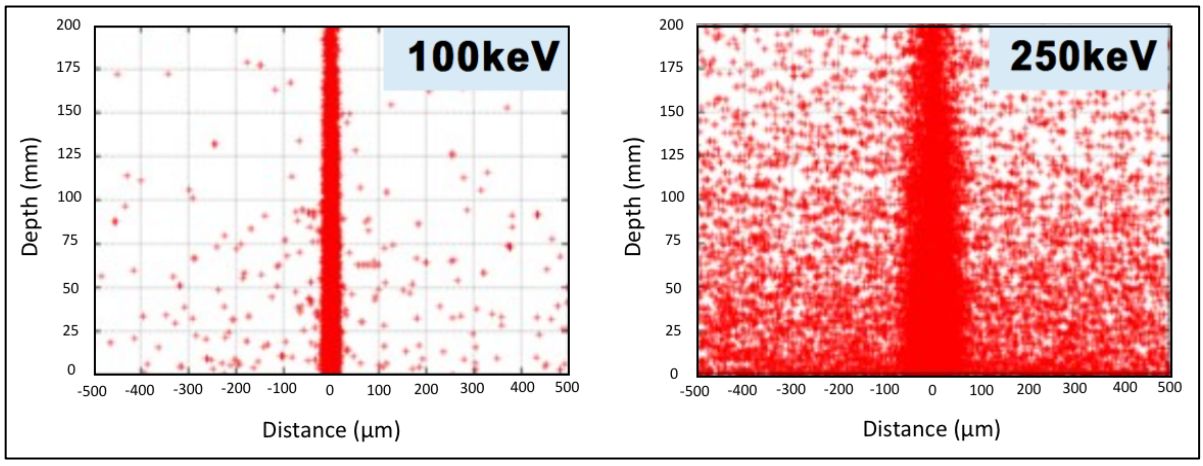

Figure 1-8: Increasing the X-ray mean energy markedly increases the amount of energy deposits in valley area by scatter[22].

1. Evaluate the normal tissue toxicity of microbeam radiotherapy in the brain.

2. Investigate an efficient and feasible desktop approach to evaluate the treatment potency of microbeam radiotherapy.

a. Develop a collimator based microbeam radiotherapy approach for an industrial cabinet irradiator.

b. Evaluate the biological equivalence of MRT to BB *in vitro* and *in vivo*.

c. Evaluate the microbeam treatment efficacy in orthotopic melanoma mouse models

3. Preliminary studies into the mechanisms of the microbeam radiotherapy effect on immune response; including investigating the differential tumor response in intact vs. immune-deficient mouse models.

CHAPTER 2 EVALUATING THE NORMAL TISSUE TOXICITY OF MICROBEAM RADIOTHERAPY IN THE BRIAN

2.1 Rationale:

Annually, approximately 200,000 new cases of malignant brain tumors are diagnosed in the US alone[23,24]. RT has remained an important treatment modality for intracranial tumors despite the inevitable normal tissue toxicity. As a result, as treatment modalities have improved, patients live long enough to experience radiation-induced brain injury[25,26]. Accordingly, the American Cancer Society has stressed that future research should focus on reducing the complications of radiotherapy to maximize the quality of life for patients after treatment[26].

Preclinical MRT has demonstrated the normal tissue sparing of this modality. However, most of these studies on the effect of MRT on normal brain tissue are focused on the short-term outcome after whole- or one-hemisphere-brain MRT[27–29]. Consequently, more recently, many groups, including Smyth et al., have emphasized the importance of evaluating chronic irradiation-induced changes by MRT treatment on a confined area of the brain[30]. Under current radiation approaches, acute (days to weeks after irradiation) and subacute (1–6 months post-irradiation) radiation-induced brain injuries are rare and reversible, while the delayed injuries (6 months to 1-year post-irradiation) are irreversible and progressive[31]. In addition, the volume of normal brain that is irradiated (the field size) is an important determinant of toxicity.

To make this technology more available for preclinical biomedical studies, the Chang and Zhou groups at UNC-CH have developed the first desktop MRT device based on the spatially distributed carbon nanotube X-ray technology (CNT)[32], which enables delivering a high dose of radiation in a laboratory setting. This system uses multiple concurrently activated cold cathodes sources arranged in a line (Fig 2-1). By distributing the electron beam along a very long and narrow line on the anode instead of a single point, significantly better heat dissipation and therefore, higher dose delivery rates can be achieved as compared to conventional point-focused X-ray tubes. Furthermore, the radiation beam can be readily gated with physiological signals during irradiation [33]. Previous studies found that applying image-guided MRT using this desktop setting was able to induce tumor control in an intracranial murine tumor model, without causing any significant histological changes up to 30 days post-irradiation[34,35]. However, the histological evaluations indicated that BB might cause more normal brain tissue damage than MRT in later time-points[34]. Consequently, I hypothesized that applying image-guided MRT using this novel method would elicit less neurocognitive impairment than equivalent BB irradiation in long-term follow-up. Here, the goal was to evaluate the potential effects of MRT on normal brain tissue and compare it with conventional broad beam (BB) post-irradiation in acute, subacute and more importantly, the chronic time intervals.

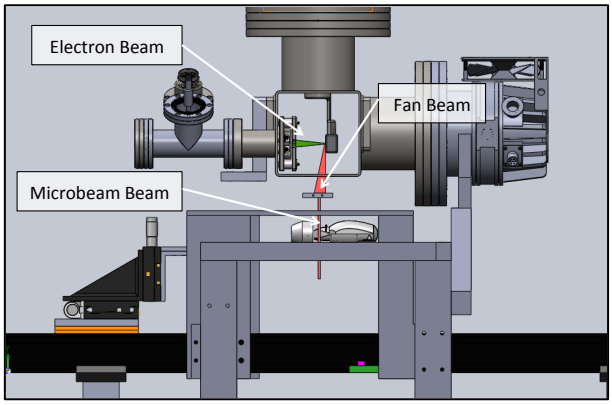

Figure 2-1: CAD drawing showing the detailed configuration of the microbeam radiation therapy system with the electron beam and X-ray beam indicated. The X-ray beam is collimated by a microbeam collimator to 300μm beamwidth.

2.2 Approach:

2.2.1 Animals:

Four-week-old male C57BL/6J mice (Jackson Laboratory, Bar Harbor, ME) were acquired and allowed to acclimate for a week before study initiation.

The mice were housed in the University of North Carolina at Chapel Hill (UNC-CH) Division of Laboratory Animal Medicine pathogen free designated environment and cared for in accordance with the United States Department of Health and Human Services Guide for the Care and Use of Laboratory Animals; all procedures were approved by UNC-CH Institutional Animal Care and Use Committee (IACUC). Mice were housed in a temperature and light-controlled environment with 12-h light/dark cycle (lights on at 7 AM) and provided food and water.

2.2.2 Irradiation:

Mice were randomly assigned to three treatment groups: microbeam radiotherapy (MRT), broad-beam radiotherapy (BB) and sham. All the mice underwent treatment at eight weeks old under anesthesia with 1%-2.5% isoflurane in medical-grade oxygen at 0.8-1 L/min flow rate. All mice kept anesthetized for an equal duration of time (two hours) to normalize the influence of isoflurane on behavioral tests outcomes[36,37].

2.2.2.1 Dosimetry:

GAFCHROMIC™ EBT3 (Ashland Advanced Materials, Covington, KY, US) film was placed at the dose entrance plane for dosimetry and evaluating the dose profiles. The key technical features of GAFCHROMIC™ EBT3 films that make them suitable for our purpose

included the minimal response difference over a wide photon energy range and high spatial resolution (25μm or higher)[38]. As a result, several MRT studies have used these radiochromic films for the dosimetry evaluations[32,39,40].

The film was cross-calibrated to an ion chamber and scanned[41,42]. Scanned films were processed using in-house written Matlab script (R-2015a, The MathWorks, Inc, Natick, MA) using principles described by Borca et al[43].

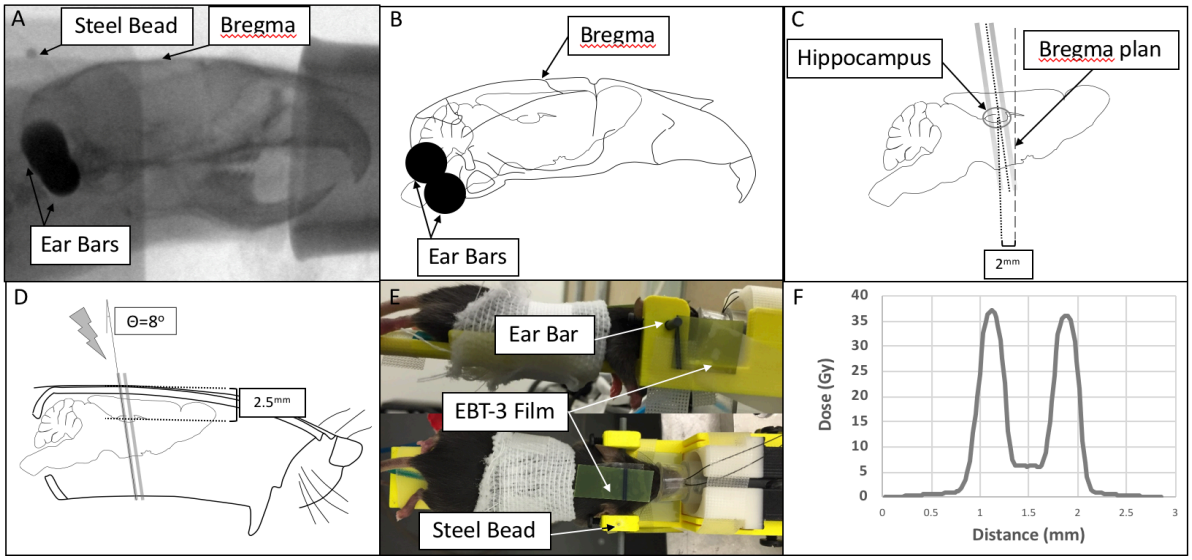

Figure 2-2: Image-guided Microbeam Radiotherapy Method Abstract. A: Lateral radiograph of mouse head was taken to locate the bregma. The head was stabilized using two ear-bars and teeth wire. Embedded steel bead served as the fiducial marker. B: The skull outlines were sketched over the same radiograph. The anatomical place of the hippocampus is shown regarding the bregma. D: Schematic lateral view of mouse skull with a cut along the corpus callosum at midline. The gray lines demonstrate the two microbeams. In our device, the microbeam planes intersect with the vertical plane at a slight angle of 8 degrees. The center of the treatment was placed 2mm posterior to the bregma (C) and 2.5mm inferior to the top of the skull. E: The side (top) and top view (bottom) of a mouse under irradiation. The head was fixed by ear bars and teeth wire. Gafromic EBT-3 film was placed on top of the mouse head (entrance plan) to record the two beams and generate the dose profile (F).

2.2.2.2 Microbeam Radiotherapy:

Image-guided MRT was applied on normal mice brains by desktop CNT-based MRT system[41]. Lateral X-ray projections were taken using onboard micro-CT scanner to locate the bregma (Fig 2-2a,b). An embedded steel bead (1/32 inch ≈ 0.8 mm) in the holder was used as the fiducial landmark (Fig 2-2a). Since the microbeam plane intersects with the vertical plane at a slight angle of 8 degrees (collimator angle)[42], it was crucial to calculate the distance to the center of hippocampus from the registered images in both anterior-posterior and superior-inferior directions (Fig 2-2c,d).

After imaging, the mice were mechanically translated from the imaging to the irradiation position. Detailed descriptions of the device and dosimetry have been previously reported[42]. Two arrays of microbeams were delivered unidirectional along the coronal plane across each mouse brain (Fig 2-2e). Each microbeam was 300 μm wide, spaced at 900 μm center-to-center distance and the radiation field was centered on the hippocampus (2mm posterior and 2.5 mm inferior to bregma) (Fig 2-2c,d). The peak dose was 36 Gy and 5 Gy dose of X-ray was manually deposited in valley area (Fig 2-2f).

2.2.2.3 Broad-Beam Radiotherapy:

An industrial X-ray machine (X-RAD 320, PXi, North Branford, CT) was used for the BB irradiation. The dose rate, after 1.5 mm aluminum, 0.25 mm copper, plus 0.75mm tin filter, was 1.06 Gy/min at a focal surface distance of 47 cm (Fig 2-3a). For BB irradiation, the hippocampal area was irradiated with 10 Gy of X-ray over 2.5 mm irradiation field, creating an integrated equivalent dose to the MRT beams. The beam was collimated down to 10 mm wide using an industrial 4-leaf adjustable collimator (PXi, North Branford, CT) and then

further collimated to 2.5 mm using fabricated collimator out of 1.5 cm plates of lead (Fig 2-3a,b). The setting applicability was pretested and the dose was measured using GAFCHROMIC™ EBT3 film (Fig 2-3c,d). During the experiment, the mice were positioned such that their heads were in close contact with the fabricated collimator and stabilized using ear bars and nose cone (Fig 2-3b). The collimator was placed 1 mm anterior to the interaural line to target hippocampus. The orientation of beam was same as MRT.

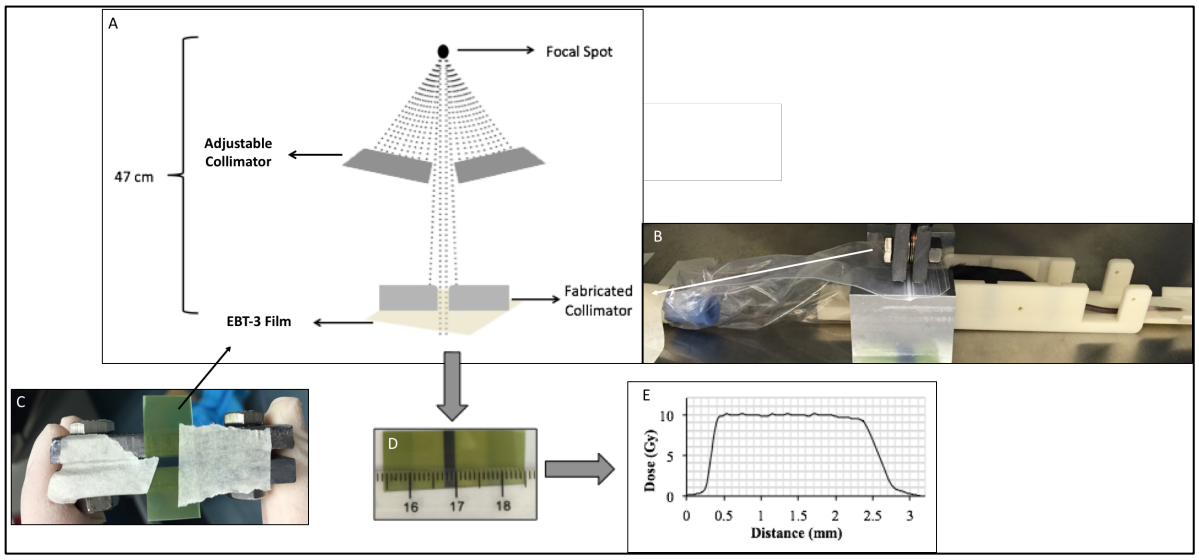

Figure 2-3: Broad-beam (BB) Irradiation Method Abstract. A: The schematic picture demonstrates the steps to collimate down the beam to 2.5mm (D). B: The fabricated collimator was placed in close contact with the mouse head. C: The Gafchromic™ EBT-3 film attached to fabricated collimator to record the entrance dose (D) and generate the beam profile (E).

2.2.3 Neurocognitive Testing:

Mice were assessed using a battery of neurocognitive function tests at baseline and at each month after treatment and weighed using a scale with the accuracy of 10^{-1} grams weekly for the duration of the study. To minimize the effects of social influences on the behavior, mice were housed three in a cage, in each, there was one member of each group. All the experiments were performed between 9:00 am-3:00 pm during consecutive days of a week. The baseline

weight and measurements of rotarod, open-field, and marble burying were compared between treatment groups, to make sure no baseline difference existed among treatment groups. A pretest was performed during which mice were evaluated pre-treatment and every week up until one month and every month post-irradiation up until three months to evaluate the appropriate time point to perform the behavioral test.

2.2.3.1 Rotarod:

Mice were placed on a cylinder, which slowly accelerates to a constant rotating speed. While the heads of the mice are placed against the direction of the rotating rods, normal mice learn to walk forward as the rod rotating-speed increases. For each trial, revolutions per minute (rpm) were set at an initial value of 3 and progressively increased to a maximum of 30 rpm across 5 min. In all test sessions, the time latency before the mouse lost its balance was measured in seconds, up to maximum 300 sec.

2.2.3.1.1 Pre-treatment training:

An accelerating rotarod (Acceler. Rota-rod (Jones & Robertson) for mice, model 7650, Ugo Basile, Varese, Italy) was used for the acquisition of the task. For the first session, mice were given 3 trials, with 45 secs between each trial. A second test session with 2 trials was conducted 48 hours later, to evaluate consolidation of motor learning.

2.2.3.1.2 Post-treatment evaluation:

A similar accelerating rotarod was used for the re-evaluation of motor coordination. For each test, mice were given 2 trials, with 45 secs between each trial.

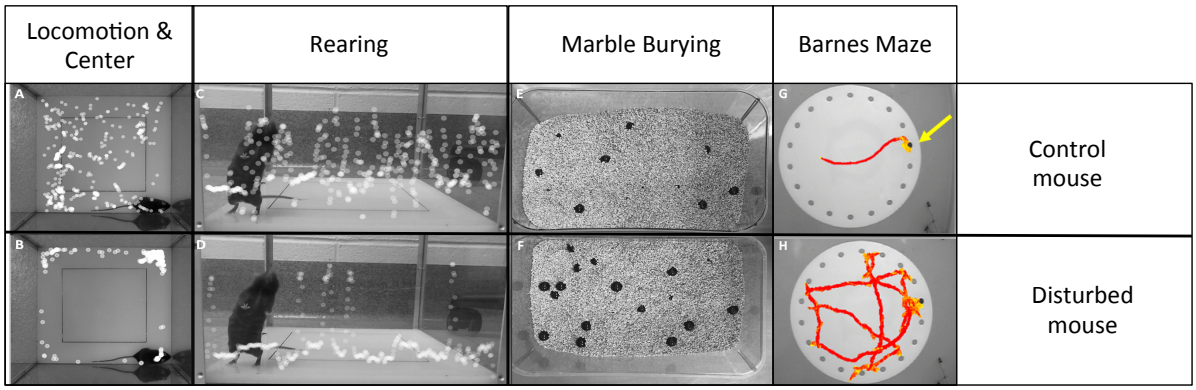

Figure 2-4: Comparison of Normal Mouse (top row) vs. Impaired One (bottom row). The white dots are the position of mouse neck (junction of head and body) at each second during first 10 min of open-field activity test (superimposed scatter plots are generated using idTracker[44]). The impaired mouse spends more time at the periphery (A vs. B) and did less rearing (C vs. D) and buried fewer marbles after 30min test (E top vs. bottom).

2.2.3.2 Open-Field Activity:

Novel environment exploration, general locomotor activity, and anxiety-related behaviors in rodents were assessed systematically within a square 41 cm x 41 cm Plexiglas® box. Mice were filmed during the 30 min trial. Measures were taken of the number of the rearing events (frequency with which the mice stood on their hind legs) and duration of time they spend doing locomotion and in the central square (29 cm x 29 cm, 50% of field area) vs. periphery in both baseline and post-treatment assessments.

A high duration of locomotion behavior and time spent in the central square indicate increased exploration and a lower level of anxiety[45]. It had been shown that anxiolytics administration increases exploration time in the center of the open-field while stressful stimuli decrease the number of center visits (Fig 2-4.a-b)[45]. Open-field activity, therefore, represents

a valid measure of marked changes in "anxiety-like" behaviors[46]. In addition, rearing frequency corresponds with hippocampal electrical activity (Fig 2-4.c-d)[47].

2.2.3.2.1 Pre-treatment:

Mice were assessed by 30 min trial in an open-field arena, crossed by a grid of photobeams. Counts were taken of the number of photobeams broken during the half an hour trial either horizontally or vertically (VersaMax, AccuScan Instruments).

2.2.3.2.2 Post-treatment:

Mouse activity was recorded during 30 min experiment in the same size arena and assessed for the same parameters using different software (The Observer XT 10, Noldus Bv, Wageningen, The Netherlands).

2.2.3.3 Marble Burying:

Digging is a species-specific behavior of mice. It has been shown that hippocampal lesions markedly reduce the number of buried marbles to the point that cages of mice with hippocampal lesions appears to have had no mice in them at all (Fig 2-4.d)[48]. To quantify this behavior, twenty 9/16" (14.3mm) black glass marbles were placed in equally distance five row and four columns in a 28 x 17 x 10 cm clear plastic cage, two third of which was filled with bedding. The cages were covered thoroughly after putting the mice in them. The number of buried marbles was counted after 30 min. Buried marble was defined as the one that more than half of it was in the bedding.

2.2.3.4 Barnes Maze:

During the test, a mouse was placed at the center of a 92 cm circular table around which there were 20 holes each 5 cm along the edges. Animals escaped from a brightly lit open arena into a small basket located under one of the openings. The opening to place the basket under was assigned for each mouse randomly and remained the same all along the testing period. The Barnes Maze platform was made in-house using measurements from Sunyer et al. [49]. Printed patterned papers were placed in different places in the room as spatial cues. Mice were tested for 7 consecutive days and measure was the duration of time before finding the right opening. Each test session was up until they enter the escape box or up to 5 min. If mice were not able to find the correct opening during the test the period, they were gently directed toward it.

The mice were evaluated by the Barnes maze test 8-month post-irradiation (to measure chronic effect). At this time point, the open-field activity was not performed because both tests are based on the fear of isolation and being exposed in brightly lit areas. Running both test at the same time may desensitize the mice against the exposed environment, and as a result, may introduce bias.

2.2.4 Immunohistochemistry:

Brain tissues from the animal were collected at the end of the 3rd- (pretest group) and 9th-month post-treatment. Whole mouse brains were fixed in formalin for 48h, processed, embedded in paraffin, serially sectioned at the 5μm thickness and were used for IHC.

IHC was carried in Bond the fully automated immunostainer (Leica). Slides were dewaxed in Bond Dewax solution (AR9222) and hydrated in Bond Wash solution (AR9590).

Hematoxylin and Eosin (H&E) stain was done in the Autostainer XL (Leica Biosystems Inc., Vista, CA). For pretest mouse, In addition to H&E, following rabbit polyclonal antibodies were used: cleaved caspase-3 (cC3), #CP229C (Biocare Medical, Concord, CA), CD11b, #NB110-89474 (Novus Biologicals, Littleton, CO), CD31, #ab28364 (Abcam, Cambridge, MA), GFAP, #Z0334 (Dako, Carpinteria, CA), Ki-67 #NCL-Ki67p (Leica Biosystems Inc., Vista, CA); Rabbit monoclonal anti-PCNA, clone EPR3821, #ab92552 was from Abcam (Cambridge, MA) and Rat monoclonal antibodies against F4/80 (#14-4801-82, clone bM8) and Myelin Basic Protein (MBP, #ab7349, clone 12) were from eBioscience (San Diego, CA) and Abcam (Cambridge, MA) respectively.

IHC and immunofluorescence were carried in Bond the fully automated immunostainer (Leica). Slides were dewaxed in Bond Dewax solution (AR9222) and hydrated in Bond Wash solution (AR9590). Antigen retrieval for all antibodies except cC3 was performed for 30 min at 100ºC in Bond-Epitope Retrieval solution1 pH-6.0 (AR9961) and in solution2 (pH9.0) for cC3.

After pretreatment slides were incubated for 30 min with PCNA (1:1000), CD11b (1:1500), GFAP (1:2500) and ki-67 (1:300) and for 60 min with cC3 (1:50), CD31 (1:200), F4/80 (1:50) and MBP (1:200). Detection of CD31, cC3, Ki-67, GDAP, CD11b and PCNA was performed using Bond™ Polymer Refine Detection system (DS9800). Detection of F4/80 was done using Bond Intense R Detection system (DS9263), supplemented with 1:500 Goat Anti-Rat (Biotin) secondary antibody (ab7096). Stained slides were dehydrated and coverslipped.

Immunofluorescent (IF) detection of MBP was done using Bond Intense R Detection kit (DS9263) supplemented with biotinylated Rabbit Anti-Rat Immunoglobulins (DAKO, E0468) and TSA-Cy3 (SAT704A001EA, Perkin Elmer) reagent; slides were counter-stained with

Hoechst 33258 (Invitrogen) and mounted with ProLong Gold antifade reagent (P36934, Life Technologies). Positive and negative controls (no primary antibody) were included for each antibody. H&E stained slides were digitally imaged in the Aperio ScanScope XT (Leica) using 20x objective. High-resolution acquisition (20x objective) of the IF slides (MBP) in the DAPI and Cy3 channels were performed in the Aperio ScanScope FL (Leica).

2.2.5 Statistical Analysis:

Statistical analysis was performed by SAS/STAT® version 9.4 (SAS Institute Inc., Cary, North Carolina). A p-value < 0.05 was considered statistically significant. The means of baseline values were compared using ANOVA to ensure there was no significant difference at baseline among treatment groups. A multilevel model, random coefficients approach was used to make inferences concerning treatment group differences. Random coefficient models allow simultaneous inferences at the aggregate and individual level while accounting for correlation between subjects that arises in longitudinal studies. These models are also more flexible than traditional ANOVA approaches because the constraint that each subject has the same regression coefficients is removed. Random coefficient models are also more powerful than standard cross-sectional methods with appropriate multiple comparison controls. For each outcome, the level 1 regression equation was found using the partial residual sum of square (PRESS) statistic under 5-fold cross-validation to determine the order of the polynomial fit.

Fitting the polynomial structure discovered using the above method; we chose the order of the random effects that would minimize BCC in the unconditional models while yielding nonzero covariance for the highest order term. Each random coefficient was modeled as a function of treatment group, engendering the level 2 regression equations. Interactions with

treatment group and time arising from the level 2 equations were assessed using type 3 tests and dropped where they were not significant. When the treatment group was found to predict linear or higher order slope terms, regions of significance were calculated. Tests of differences in treatment groups were conducted where the treatment group was found to predict intercepts only.

Table 2-1: Pre-irradiation Evaluation of the Mice in Three Groups.

Measurement		**P-value**
Weight		0.576
Rotarod		0.365
Marble Burying		0.216
Open-field Activity	Rearing	0.332
	Center	0.506
	Locomotion	0.241

2.3 Results:

Fig 2-5 demonstrates a schematic flowchart of the current study. Mice were weighted and pre-evaluated using a series of cognitive tests and randomly assigned in three treatment groups (see pre-irradiation Fig 2-5). No significant differences were among MRT, BB, and shams in any of measurements at baseline (Table 2-1).

Mice brains in MRT and BB groups were irradiated with integrated equivalent dose (irradiation phase Fig 2-5). All mice in MRT and BB groups tolerated the irradiation procedures well, with

no specific veterinary concerns. Acute skin effects (erythema, desquamation, inflammation or epilation) were not detected in any mice after any irradiation approach.

Histological studies and pretest results (see Fig 2-8) demonstrated no measurable changes during the acute phase post-irradiation (up until one month) and as a result, the mice were evaluated every month post-irradiation using a battery of test in the current study as demonstrated in Fig 2-5, post-irradiation phase. The BB mice, whose brains were irradiated with homogeneous 10Gy of X-ray using a 2.5mm wide beam, tended to gain weight at a slower rate than MRT and non-irradiated mice. This difference became statistically significant between BB and controls since week 31 post-irradiation until the end of the experiment (week=42) (Fig 2-6).

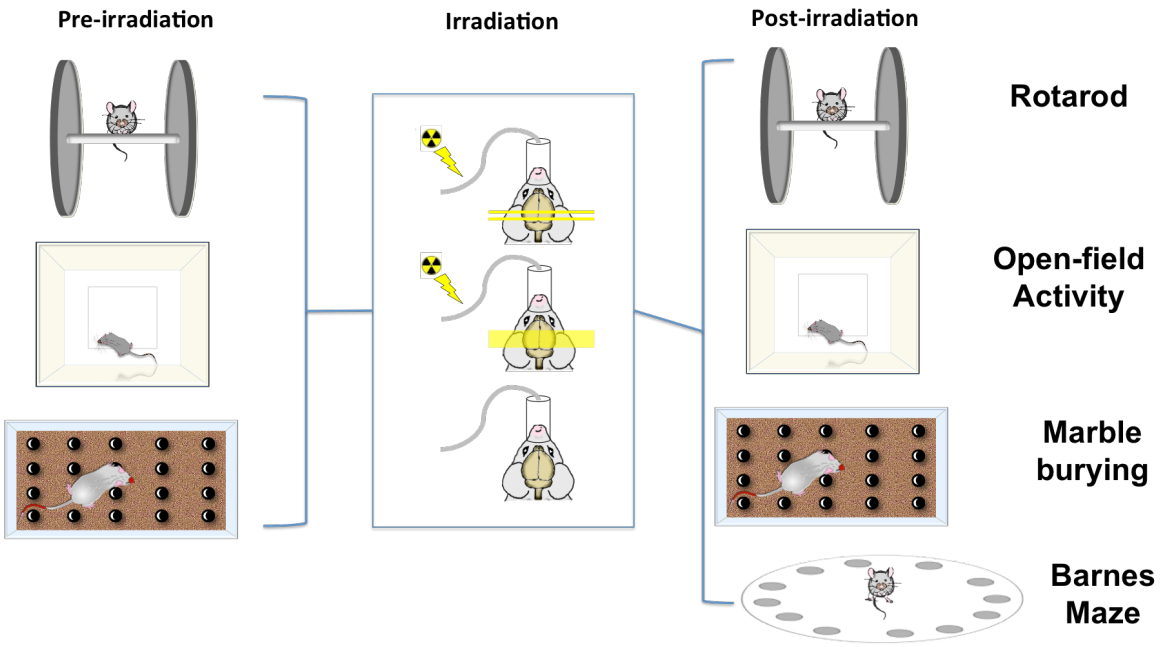

Figure 2-5: Method Abstract. The mice were pre-evaluated using rotarod, open-field activity and marble burying tests were randomly assigned to three treatment groups: broad beam (BB), microbeam radiotherapy (MRT) and controls. All mice were maintained under gaseous anesthesia for the equal duration of time. The post-irradiation evaluations were performed each month by rotarod, open-field activity and marble burying and 8-month after exposure Barnes maze test was used to evaluate the mice. All mice brains were sent for histological assessments 9-month post-irradiation.

There was no difference in the duration of time mice kept their balance on the rotating rod, duration of rearing and duration of time mice spent in the central area of the open-field arena by treatment group (Table 2-2).

The number of the buried marbles in BB was significantly less than the control group and significantly less than the MRT group at all time points ($p \leq 0.01$) and BB mice spent less time searching around the open-field arena ($p < 0.001$).

BB mice spent more time finding the correct hole in the Barnes maze test than shams in all test sessions ($p = 0.044$). There were no differences between the MRT and shams for either of these outcomes.

Interestingly, at five-month post-irradiation, a depigmented line appeared in all BB mice at the site of irradiation (Fig 2-7) which progressed until 6th month and remained the same without any regression or progression for the duration of the study (up to 9-month post-irradiation). In two out of eight mice in MRT group, a line of gray hair appeared in the exit plan at the beginning of 8-month after irradiation that stopped progression after 20 days and did not regress up to the end of study.

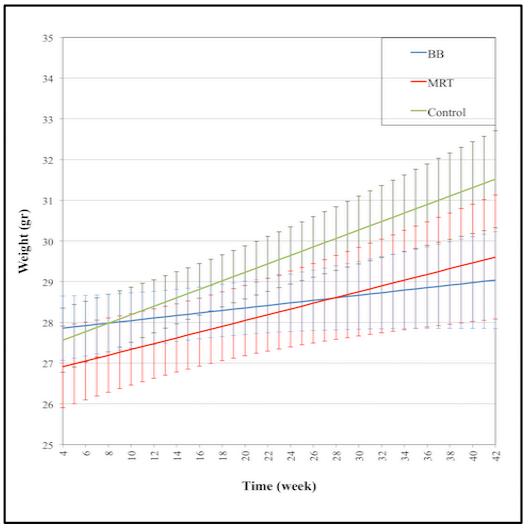

Figure 2-6: Predicted Mean of Mice Weight. The mice were weighed at their arrival to the facility and each week after irradiation. The error bars are SD.

The brain tissues of the mice were collected 4 and 9 months post-treatment in pretest and test studies, respectively (Fig 2-5 histology). No histological changes were detected in any mice brain sample using IHC (Fig 2-8).

Table 2-2: Post-irradiation Longitudinal Neurocognitive Evaluation

Behavioral Tests		**Group Difference***	**P-value**
Rotarod		MRT vs. Control vs. BB	0.520
Marble Burying		MRT-Control=0.0572	0.910
		MRT-BB=1.410	0.011^{+}
		Control-BB=1.353	0.009^{+}
Open-field Activity	Rearing	MRT vs. Control vs. BB	0.180
	Center	MRT vs. Control vs. BB	0.510
	Locomotion	MRT-Control=35.211	0.235
		MRT-BB=120.50	0.0005^{+}
		Control-BB=85.291	0.005^{+}
Barnes Maze		MRT-Control=3.549	0.861
		MRT-BB=-36.298	0.085
		Control-BB=-39.847	0.044^{+}

**The difference between predicted means are reported when a test showed statistically significant difference among groups;* $^{+}$*P-Value<0.05*

2.4 Discussion:

Radiation-induced cognitive impairment is the most frequent complication among long-term cancer survivors and occurs in up to 50–90% of adult brain tumor patients who survive more than 6 months post fractionated partial or whole brain irradiation[50–53]. In spite of adequate disease control, cognitive impairment interferes with the patients' ability to function at their

pretreatment levels. Multiple prior animal studies have reported that synchrotron MRT induces less neurotoxicity than conventional radiotherapy[54,55]. Here, I found that MRT using the first-generation CNT-based image-guided desktop microbeam irradiator would also cause less neurocognitive impairment than equivalent BB irradiation.

Local irradiation of hippocampal area with 10 Gy led to declined cognitive function in BB mice compared to sham (See Table 2-2). It has been found that 8-month after X-ray irradiation of mouse brain with 10 Gy, there was significant inhibition in neurogenesis level at hippocampus[56]. These may explain the decline in BB mice cognitive level in the current study at 8th-month post-irradiation measured using Barnes maze test.

Interestingly, no significant difference was found between MRT and shams at any time points post-irradiation. Different studies have reported that brain normal tissue can maintain its normal function and integrity at higher doses of X-ray in MRT than conventional radiotherapy methods. Four main mechanisms have been postulated to play a crucial role in keeping the normal tissue integrity after MRT. First, a "beneficial" bystander effect is hypothesized to facilitate the restoration of injured cells in central nervous system[57]. Second, due to the unique spatial distribution of X-ray in MRT, the total contact surface between highly irradiated and damaged tissue along the beam and minimally irradiated valley area is increased which may allow cells in the valley to maintain the function of the normal tissue. Third, multiple studies revealed that normal brain macro and microvasculature show higher tolerance to MRT and immature vessels like tumor neovascular are preferentially damaged by this method[58]. At last, recently, it has been shown that a spectrum of the immune response would be evoked after radiation therapy. Interestingly, studies have demonstrated that activated immune responses after MRT favor the tumor resolution while preserve the normal tissue function [59,60].

No acute skin effects were observed in any mouse after broad- or micro-beam radiotherapy. In the current study, we observed the depigmentation hair circle in all BB-treated mice at the site of irradiation (Fig 2-7). Kinoshita et al. also observed the same effects when locally irradiated C57BL/J6 mice by a single fraction of 10 Gy[61]. Microbeam radiation therapy utilizes relatively low beam energies to maintain the spatial fractionation deep in the tissue (an anode voltage energy of 160 kVp was used in the present study), which results in the lower dose penetration than the conventional radiotherapy. As a consequence, a significantly higher dose to the skin's surface needs to be applied during MRT to ensure an adequate dose delivery to the target tissue. Paradoxically, in multiple microbeam therapy studies higher than normal tolerance of normal skin tissue has been observed[9,30]. Interestingly, a line of gray hair appeared in two mice in MRT group at the exit plan 8-month after X-ray exposure. Previous studies have shown that skin effects are more severe at the joint places like axilla, groin and toes where the skin is subject to friction, or has folds in its surface[62]. Since this line coincides with the junction of mouse head and neck, we hypothesized that this effect may be due to the constant motion of these tissues with the associated inflammation.

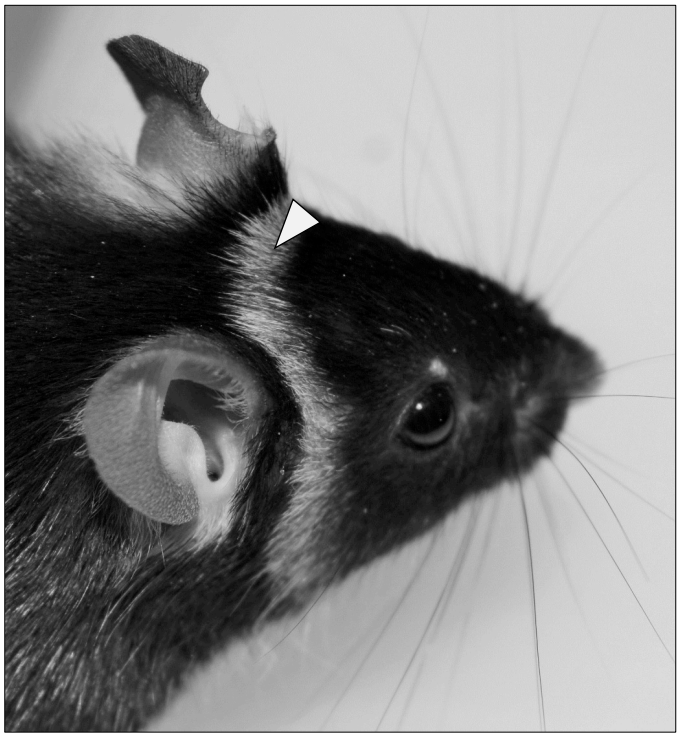

Figure 2-7: Picture of a BB-treated mouse head 6 months post-irradiation. The arrow points to the circle of gray hair at irradiation site.

No significant histological differences were detected 4- and 9-month post-irradiation based on light microscopy level (Fig 2-8). While some hypothesized that neurocognitive changes may precede histological changes, a growing number of studies have correlated the radiation-induced cognitive deterioration to changes in the subcellular and molecular level of neuronal function and plasticity, particularly hippocampal long-term potentiation[63]. These changes can happen even after a modest dose of X-ray (2-10 Gy)[64].

It is well established that the hippocampus plays a crucial role in learning and memory and its damage leads to various behavioral alterations including spatial learning impairment and disturbances in fear/anxiety responses[65,66]. Given these critical roles and the importance of hippocampal sparing radiotherapy in clinical applications[67], I focused on the hippocampus as the target of the treatment and used a radiation field size to cover the whole mice hippocampus[68]. As a consequence, the chosen behavioral tests were focused on evaluating hippocampal-associated function.

Here, I mimicked clinical irradiation protocols, so I applied a local low X-ray dose that I knew would induce cognitive impairments[69], but was well below the threshold for inducing obvious histological changes. Due to the distinct spatial fractionation of X-ray beam in MRT, finding the actual equivalence dose of MRT is complex. Previous studies have used different assumptions for the physical or biological equivalent dose[60,70]. Priyadarshika et al. suggested that the integrated dose of MRT, which is the microbeam dose averaged over the entire radiation volume, might be more relevant than the peak or valley dose when compared to broad-beam radiation[71]. In the previous study using the prototype of CNT-MRT irradiator, it has be found that 10Gy of the BB would induce same treatment efficacy as the integrated MRT dose[34]. Accordingly, here I also assumed that integral dose is close to actual equivalent dose,

so for MRT group an identical anatomical region of the brain was irradiated with the equal integrated dose.

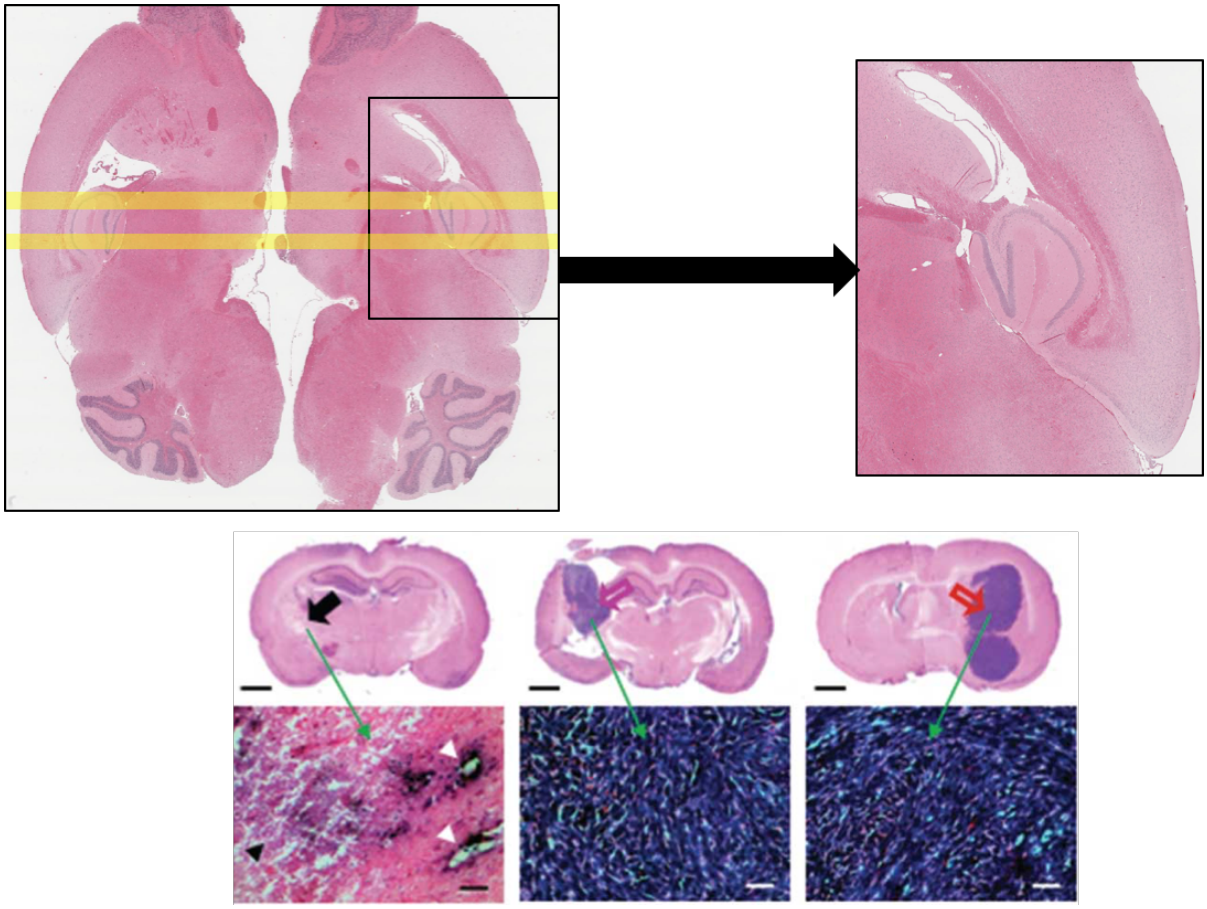

Figure 2-8: Top) H&E stain 4 months after 2 arrays of ≈40 Gy microbeam radiation therapy. No significant change was detected in the field of radiation. Bottom) The basophilic areas demonstrate radionecrosis after radiation with 40Gy[72].

The peak-to-valley dose ratio (PVDR) has been measured 16 at the entrance plane and decreased to 14 at the exit plane, so the equivalent integral dose of 10Gy BB simulated to be two peaks of ≈46Gy[34]. But several histological studies after high dose brain MRT have shown a discrete band of neuronal and glial nuclei loss only along the beam path[14,73–75]. This observation supports the idea that surviving cells in the valley region play the main role in maintaining tissue function and compensating for the loss of functional cells in the peak region.

Consequently, it has been postulated that after microbeam irradiation, brain toxicity is more dependent on valley region parameters[30]. The average dose rate at the mouse brain entrance plane has been measured to be 1.2 Gy/min. As a result, to keep the total duration of the procedure under 2 hours, I selected a peak X-ray dose of 35 Gy with a valley dose 5 Gy, to increase the toxic effect of our method.

Recent study on zebrafish fin using single peak of 5000 Gy has demonstrated that any peak ≥ 400 μm cause the permanent damage to the mature and developing (tumor) microvasculature[76]. Interestingly, thinner peaks (50 μm $\leq$ peak$<$400 μm) induced permanent destruction of immature microvasculature, while the normal vessels could heal the damages 48h post irradiation. The generated beam with the CNT-MRT device is 300 μm that is below this threshold.

In conclusion, I found that microbeam radiotherapy using the CNT-MRT desktop device and the irradiation protocol I utilized in the current study induced less neurocognitive impairment than the same integrated uniform dose on the hippocampal area in normal mice up to 8-month post-irradiation. The previous studies demonstrated that applying MRT using this device is able to control the murine model of glioblastoma effectively[35]. This suggests that another potential advantage of MRT in brain tumor treatment is improved local tumor control rates with the ability to apply radiobiological higher doses either by re-irradiating of the same lesion using the same method or combining other radiation modalities. Brain tumors are the most common solid tumor in pediatrics and MRT seems to be a promising treatment modality for this group of patients[77].

CHAPTER 3 INVESTIGATING AN EFFICIENT AND FEASIBLE DESKTOP APPROACH TO EVALUATE THE TREATMENT POTENCY OF MICROBEAM RADIOTHERAPY: A) DEVELOPING A COLLIMATOR BASED MICROBEAM RADIOTHERAPY APPROACH

3.1 Rationale:

As mentioned before (Chapter 1), ultra-high intensity parallel X-ray photons generated by synchrotron sources have the ideal characteristics for applying thousands Gy microbeams. Unfortunately, such synchrotron sources are spare. At present, only two active synchrotron facilities in the world are running preclinical MRT studies, so there is difficulty and high cost related to running synchrotron-based MRT studies. Thus, MRT has not yet been clinically applied, mainly due to a lack of sufficient preclinical data.

Recently, there have been some efforts to apply MRT using non-synchrotron irradiators[40,78]. Nevertheless, the radiation profiles of these approaches suffered from the non-uniformity of the beams and valleys, and also the variability of the peak-to-valley dose ratios (PVDR). These are the critical parameters in the normal tissue sparing and therapeutic efficacy of the MRT[60]. In addition, there are multiple clinical limitations for microbeams less than 150 μm as described before by Dilmanian et al., namely, loss of beam spatial resolution *in vivo* as a result of cardiorespiratory induced motion in the target organs[79]. Therefore, slightly wider beams (200 μm ≤ FWHM < 1 mm) have been proposed as a promising clinical future for this technique. Studies at synchrotron exhibited the normal tissue sparing effect for beams up 0.68 mm in FWHM[79–81]. Babcock et al. designed a collimator to mount near an industrial source to

to create microbeams[82]. Although their method demonstrated the feasibility of utilizing a conventional X-ray tube to implement MRT, their resultant beams were 1 mm wide, which is in contrast to the definition of MRT. Additionally, a recent study by Brönnimann et al. revealed that beams ≥ 400 μm may induce unfavorable microvascular response in normal tissue[76].

Zhou group at department of physics at UNC-CH developed the first desktop device for applying 300 μm wide beams using a multi-beam source, based on a field emission carbon-nanotube X-ray tube[42]. The first-generation device was able to apply an image-guided, physiologically gated beam with an entrance dose rate of 21.7 mGy/s and in a long duration behavioral study, I found the generated beams using this device was able to spare the normal mouse brain tissue as described in detail in previous chapter[33,41,83]. Since the first-generation device was not ready to generate the ultrahigh dose of hundreds Gy used in MRT studies in a reasonable time frame, I sought to investigate the possibility of applying MRT using a conventional irradiator and a simple and inexpensive collimator, to facilitate preclinical studies on MRT.

3.2 Approach:

3.2.1 Irradiation:

An industrial small animal irradiator (X-RAD 320, PXi, North Branford, CT) was utilized as the radiation source for microbeam radiation (MRT) and conventional radiation (CRT). The tube specifications are presented in Table 3-1 and compared to a clinical orthovoltage tube. This irradiator incorporates an oil-cooled anode, which enables running the device for multiple hours to generate the hundreds Gy doses for MRT peaks. It also has an integrated plane parallel transmission chamber (PTW 7862, PTW, Freiburg, Germany), which can be cross-calibrated

to ionization chamber (I used MDH 1015, Radcal, Monrovia, CA; the sensitive area of detector ≈ 1 cm×2 cm) at desired focus-surface distance (FSD), to measure the dose rate and the total dose on-time. For all experiments, the tube was driven at 160 kVp and 25 mA to match our prior setting[84]. The beam was filtered with an additional 2 mm Al and the target was placed at 37 cm FSD.

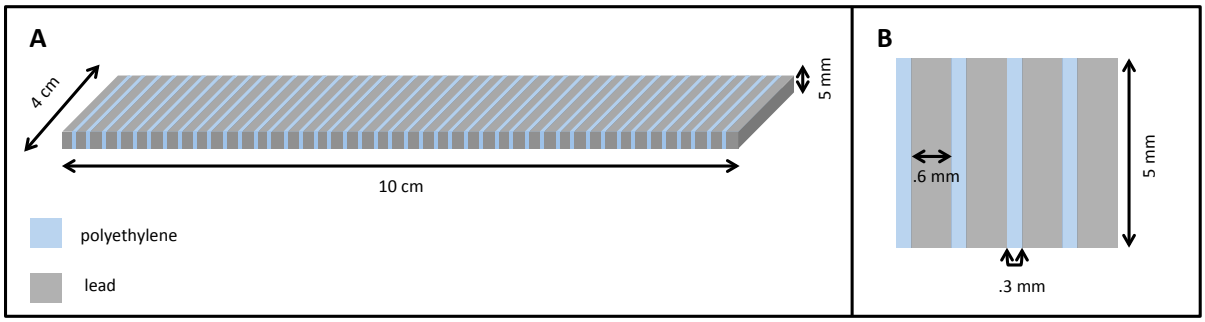

Figure 3-1: Microbeam Collimator A) The top view of the collimator; B) The detailed layers of collimator (the picture is not drawn to scale).

3.2.2 Collimation:

The microbeams were produced by a custom multi-slit collimator placed in close contact with the target (proximal collimation). The collimator consists of 5 mm thick lead ribbons, which block 99.999% of the primary photons in the highest energy spectrum range. To develop the collimator, a 0.6 mm thick, 5 mm wide lead ribbon was cut into 10 cm long pieces. A sandwich of 46 lead pieces was made by alternating 300 μm thick polyethylene sheets as spacers (Fig 3-1b). The resulting collimator was 4 cm wide and 10 cm long (Fig 3-1a).

Table 3-1: Comparison of XRAD-320 vs. Xstrahl-300

	XRAD-320 (Preclinical)	***Xstrahl-300 (Xstrahl Ltd, UK) (Clinical)***[85]
Target Material	Tungsten	Tungsten
Theta (degree)	30	30
Fixed Filter	Br=2 mm	Br=0.8±0.1 mm
Focal Spot (Largest diameter; mm)	8	≈ 7.5
Cooling System	Oil	Water to Air; Water-cooled
Tube power max (kW)	4	3
Dose Rate (Gy/min)	2.9	2.16 (FSD=20 cm; 150 kVp; Filters=2.25 mm Al and 0.15 mm Cu; mean energy=62 KeV)
Dose Measurement	PTW 7862 transmission chamber	N/A
1st HVL_{Al}(mm)	7.99±0.41	

3.2.3 Dosimetry:

SpekCalc version Pro was used to simulate the X-ray spectra[86–88]. GAFCHROMIC™ MD-V3 (peak) and EBT3 (valley) films (Ashland Advanced Materials, Bridgewater, NJ, US) were utilized for dosimetry and evaluating dose profiles[38,89]. The films were cross-calibrated to the integrated plane parallel transmission chamber without any collimator in place and scanned 24h later with 1200 dpi resolution (spatial resolution ≈ 20 μm). Scanned films were processed by in-house written Matlab script (R-2015a, The MathWorks, Inc, Natick, MA) using three-channel dosimetry principles described by the supplier[90]. Exposure doses were chosen such that peak and valley doses fell into the films' optimal sensitive range (1-10Gy for EBT3 and 1-100Gy for MD-V3)[38,89].

A custom dose phantom was also created to evaluate the dose depth effects of the system. Ten layers of 4 cm×4 cm PMMA, with a thickness of 2 mm each, were sandwiched with 11 layers of GAFCHROMIC™ films of the same area to construct a phantom, as shown in Fig 3-2. Data from this phantom were used to calculate the percentage dose drop (PDD) with and without the collimator and peak-to-valley-dose ratio (PVDR) and full-width half-maximum (FWHM) of peaks generated using the collimator. Since kilovolt energy photons were used in these experiments, the reference point (MU) was defined at the phantom surface. The field size (4 cm×4 cm) was matched to the clinical orthovoltage irradiator applicator at FSD=30cm[85]. The aluminum first half-value-layer (HVL_{Al}) was evaluated following AAPM's TG-61 for kilovoltage X-ray beam dosimetry protocol setup[91]. All the experiments were repeated at least three times.

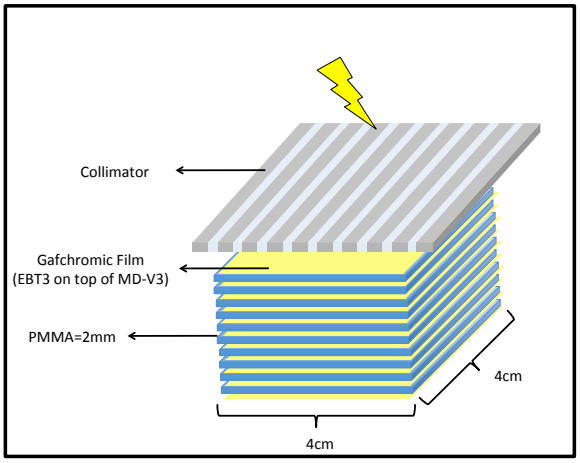

Figure 3-2: Schematic picture of PMMA phantom used for dosimetry evaluations. Eleven layers of Gafchromic EBT-3 and MD-V3 films were sandwiched with 10 pieces of PMMA sheets to measure MRT and CRT behavior in depth.

3.2.4 Immunohistochemistry:

To investigate the spatial resolution of the beam *in vivo*, the mid and posterior part of a C57BL/6J mouse brain was irradiated under anesthesia using the collimator with 100 Gy beams. The mouse was acquired from Jackson Laboratory (Bar Harbor, ME), housed in the UNC-CH Division of Laboratory Animal Medicine pathogen free designated environment and cared for in accordance with the United States Department of Health and Human. Brain tissue from the animal was collected 6h post irradiation and was fixed in formalin for 48h, processed, embedded in paraffin and serially sectioned at 5 μm thickness. Sectioned slides were used for γ-H2AX (Double-DNA-Strand-Break marker) immunofluorescence (IF) staining immediately. Rabbit monoclonal anti-phosphoser 139-H2AX antibody was from Cell Signaling Technology (Cat# 9718, Danvers, MA). IF was carried in the Bond Autostainer (Leica Microsystems Inc., Norwell, MA). All solutions were from Leica Microsystems (Norwell, MA). Slides were deparaffinized in Bonddewax solution (AR9222) and hydrated in Bond wash solution (AR9590), antigen retrieval of γ-H2AX was performed for 20min at 100ºC in Bond-epitope retrieval solution 1 pH-6.0 (AR9961), then protein blocking reagent (PV6122, Leica) was added for 10min. After pretreatment, the slides were incubated for 2h with γ-H2AX (1:2000). Detection was performed using the BondT Polymer Refine Detection system

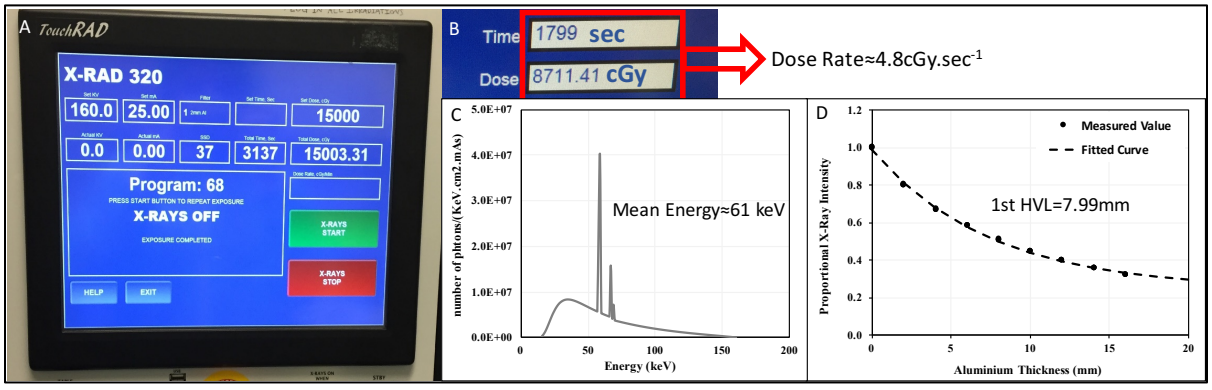

Figure 3-3: A, B) The irradiator setting used for our studies. C) The simulated X-ray spectrum. D) Intensity through different thickness of aluminum

(DS9800) and Tyramide-Cy5 reagent (Perkin Elmer, SAT705A001EA). Slides were counterstained with Hoechst 33258 (H3569, Invitrogen, Carlsbad, CA) and mounted with ProLong Gold antifade reagent (P36934, Life Technologies). Positive and negative controls (no primary antibody) were included. High-resolution acquisitions of IF slides in the DAPI and Cy5 channels were performed in the Aperio ScanScope FL (Leica) using 20x objective. Nuclei were visualized in DAPI channel (blue) and γ-H2AX in Cy5 (red).

3.3 Results:

At an FSD of 37 cm, XRAD 320 produced a homogenous 14.5 cm×14.5 cm radiation field. The mean dose rate in the air at this distance was ≈ 2.9 Gy/min (4.8 cGy/sec) after the filters described in the Table 3-1 (Fig 3-3a,b). The simulated X-ray spectrum of the device can be found in Fig 3-3c. The mean energy of X-ray spectrum was 61 KeV and the 1st HVL_{Al} was 7.99±0.41 (Fig 3-3d). The mounted transmission chamber measured the dose within 1.25±.08 percentage difference compared to the cylindrical ion chamber.

The dosimetric characteristics of the collimator are shown in Table 3-2.

Table 3-2: Collimator Dosimetric Characteristics

Beam FWHM (µm)	**246±32**
Center-to-Center (µm)	**926±23**
Peak to Valley Dose Ratio	**24.35±2.10**
Relative Output Factor	**0.84±0.04**

The collimator (Fig 3-1) was able to convert the cone beam of this irradiator to 44 microbeams. The generated beam profile is shown in Fig 3-4a. In the y-direction (parallel to the beams), the peak did not decrease as the distance to the central axis increased (Fig 3-4b). As shown in Fig 3-4c, the profile was uniform in the x-direction, and homogenous valleys were generated.

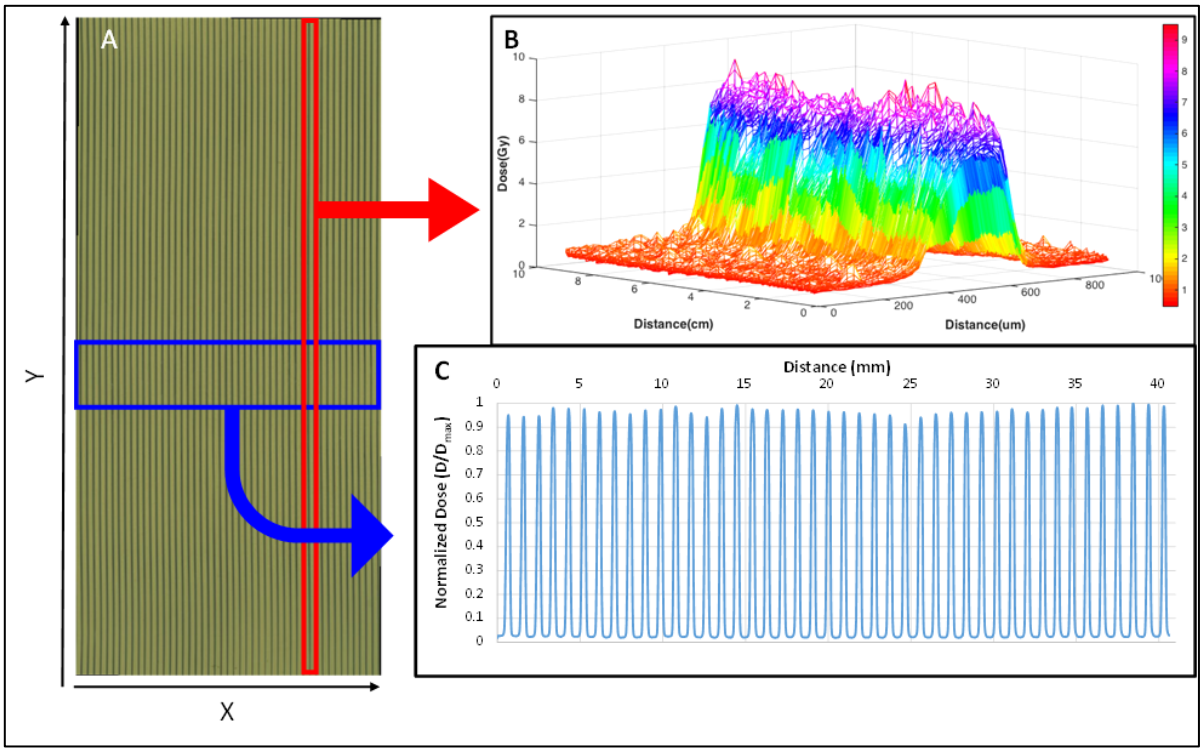

Figure 3-4: The beam profile at the PMMA phantom entrance A) Gafchromic film showing the beam pattern. B) A single beam pattern at y-direction: the peak dose did not fall when the distance to the central axis increased. C) The normalized beam profile in x-direction: homogeneous peaks and valleys.

To study the behavior of microbeams deep in the tissue, the PDD of peak, valley and integral dose and PVDR at different depths using the PMMA phantom was measured and compared with CRT. The results are shown in Fig 3-5. It should be noted that the thickness of radiochromic films (EBT3=278 µm; MD-V3=255 µm) were added to the PMMA sheet thickness (2 mm) to measure the depth of each point in the phantom. The entire doses in Fig 3-5a were normalized to the mean entrance dose in CRT and the mean entrance integral dose

in MRT. Interestingly, the CRT and MRT integral doses demonstrated a similar pattern in depth. The peak dose dropped to its half value at 19.61±0.04 mm depth, while the valley dose increased in the first 12.7 mm and then started to decrease. As a result of peak and valley dose behavior in tissue, PVDR decreased exponentially.

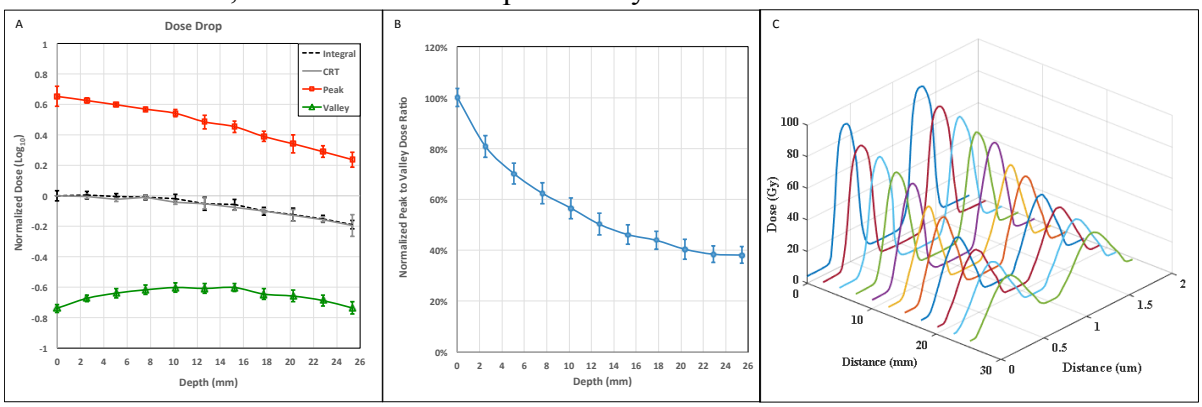

Figure 3-5: The dosimetric characteristics of microbeams at different depth of PMMA phantom. A) Percentage dose drop of peak, valley and integral dose vs. CRT; please note that all the dose values were normalized to the entrance dose in CRT and integral dose at the entrance plan in MRT. B) Dose drop of the PVDR at different depths, normalized to the entrance PVDR. C) Beams pattern at different depth of PMMA phantom.

One major concern in using non-synchrotron irradiators (divergent photons) to apply MRT is the loss of spatial resolution deep in the tissue, as well as potential formation of a homogeneous high dose radiation field that may cause tissue damage at the exit plane. Microbeams profile at various depth of PMMA is shown in Fig 3-5c. The beams maintained their resolution at least up to the depth of our phantom (≈ 2.53 cm), sufficient for small animal studies, where the thickest portion of the body (head) in the prone position is around 2 cm deep. To further investigate this depth dependence of the beam, a 4 cm×10 cm EBT3 film was placed along the beam path (longest dimension was parallel to the beams) between two 2 mm thick PMMA sheets and irradiated with 25 Gy (Fig 3-6a and b). Interestingly, the peaks and valleys were distinguishable at 10 cm depth (Fig 3-6c). To evaluate the spatial resolution of beams *in vivo*, a mouse brain was irradiated with 100 Gy microbeams. The mouse was sacrificed 6h post-irradiation and its brain tissue was stained with γ-H2AX, a DNA double-

strand break marker. The micro-beams maintained their spatial resolution in vivo where physiological movements (heartbeat and respiration) were two major confounding factors (Fig 3-6d).

3.4 Discussion:

Synchrotron generated microbeam radiation preclinical studies have shown promising results in sparing the normal tissue while inducing higher therapeutic effects than conventional radiation therapy[60,80,92,93]. These findings have prompted investigators to explore ways to generate MRT using non-synchrotron irradiators, with the goal of facilitating the translation of this promising modality to the clinic. However, most of these studies have designed complicated collimators or irradiators that confined the MRT studies to a few labs and facilities[40,78,82,84]. Here, I have demonstrated a straightforward and affordable method for applying heterogeneous MRT over a large field of irradiation using an industrial animal irradiator. Moreover, my simple method generates a reasonable dose rate allowing this microbeam application to be reproduced in a wider variety of facilities. When compared to previous studies, the dosimetric characteristics of my method are in substantial agreement. The PDD pattern of peaks, valley, and PVDR is identical to previously measured and reported dosimetric evaluations of MRT[80,94,95]. The PVDR in my study is also comparable to a previously reported non-synchrotron-based study[82]. In fact, it should be noted the valley dose is generated due to Compton scatter, and consequently, it is roughly proportional to the primary peak dose from which it originates and decreases as the number of beams decreases (smaller radiation field size). As a result, the fact that I generated comparable PVDR while covering larger radiation field (4 cm ×10 cm field vs. 1.75 cm circular field in Babcock et al. study) and

using higher peak dose (100 Gy for peak and valley doses measurements vs. 20-25 Gy in Babcock et al. study) underlines the utility of my method. Furthermore, I utilized two different radiochromic films with different ranges of sensitivity to precisely measure peak and valley doses and scanned them with high resolution (1200dpi), which allowed higher accuracy compared with previous studies[82]. The calibration curves of EBT3 and MD-V3 in three-color channels are demonstrated in Fig 3-7. I also found that starting at ≈23 mm deep in the tissue,

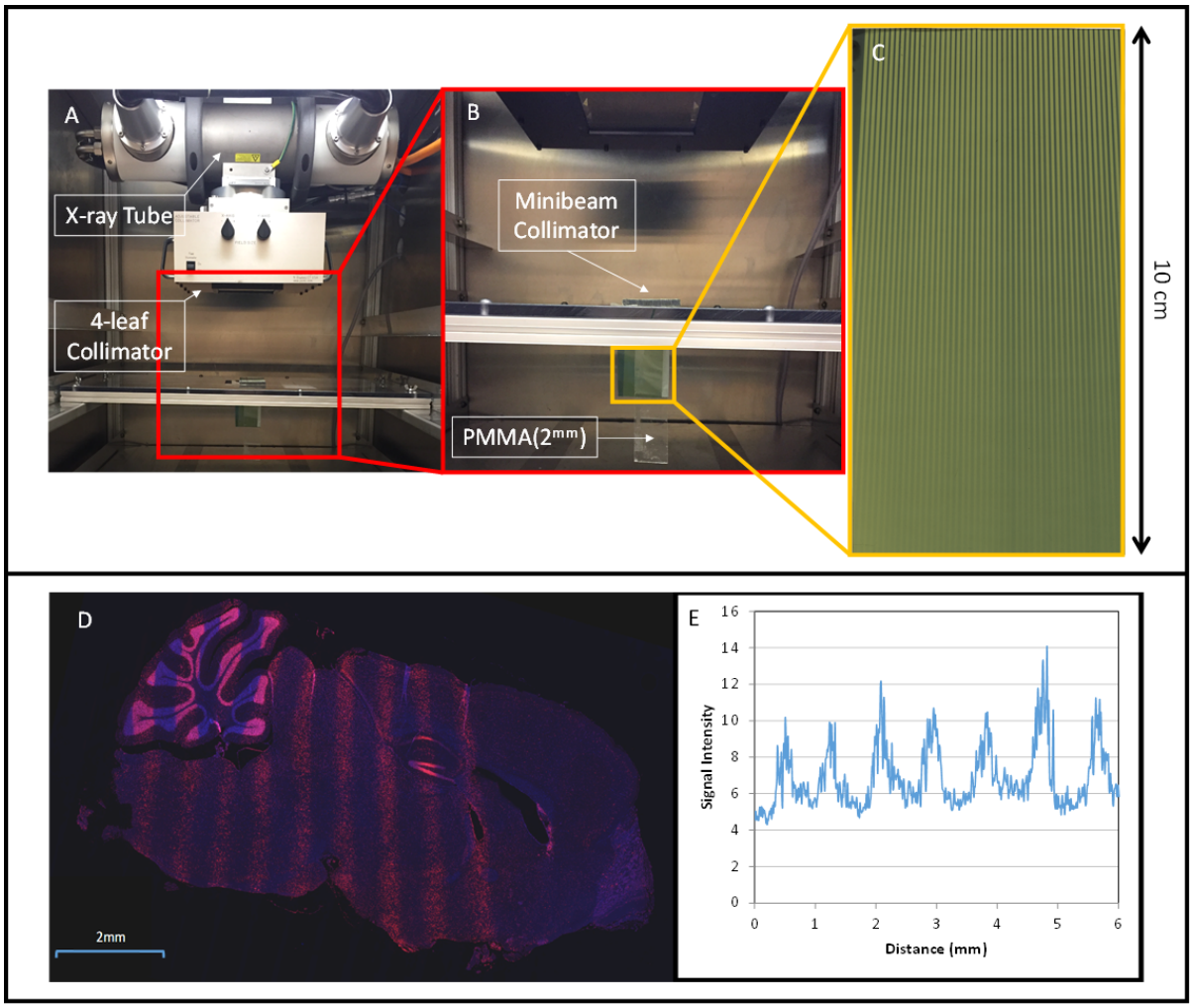

Figure 3-6: The spatial resolution of the MRT in phantom and mouse brain. A layer of EBT3 (4×10 cm) was sandwiched between two layers of PMMA (2 mm each) and placed under the minibeam collimator (longest dimension along the beam), at 37 cm FSD (A,B). C) The mini-beam behavior in the film: the peaks were distinguishable at 10 cm depth. D) γ-H2AX staining of the mouse brain, 6h post irradiation with 100 Gy MRT: the beam kept their resolution deep in the tissue (D,E).

the PVDR remains almost constant within the error bars (Fig 3-5b). This pattern has been reported before[80], and illustrates the normal tissue sparing effect of this method at the exit plane. The peaks in our method dropped to 50% at lower depth compared to synchrotron generated MRT, which was expected due to the lower mean of energy used in our experiment relative to the synchrotron (61 KeV here vs. 80 KeV or higher in synchrotron studies)[80].

The use of an industrial irradiator as the source of radiation for MRT introduces two major limitations as shown in the following diagram (Fig 3-8).

First, as mentioned in the introduction, in MRT, kilovolt X-ray beams are utilized in order to keep the spatial fractionation deep in the tissue. At this energy level, more than 99% of electrons energy would be converted to heat in the anode. In the current study, an oiled-cooled-anode irradiator with a large focal spot (8 mm) was employed that provides better heat conduction in the anode and, in addition, lessens the heel effect. So, a large homogeneous radiation field can be used to apply MRT on a large area to minimize the duration of radiation (Fig 3-9a) and consequently, lessen the chance of smearing of the beams due to physiological

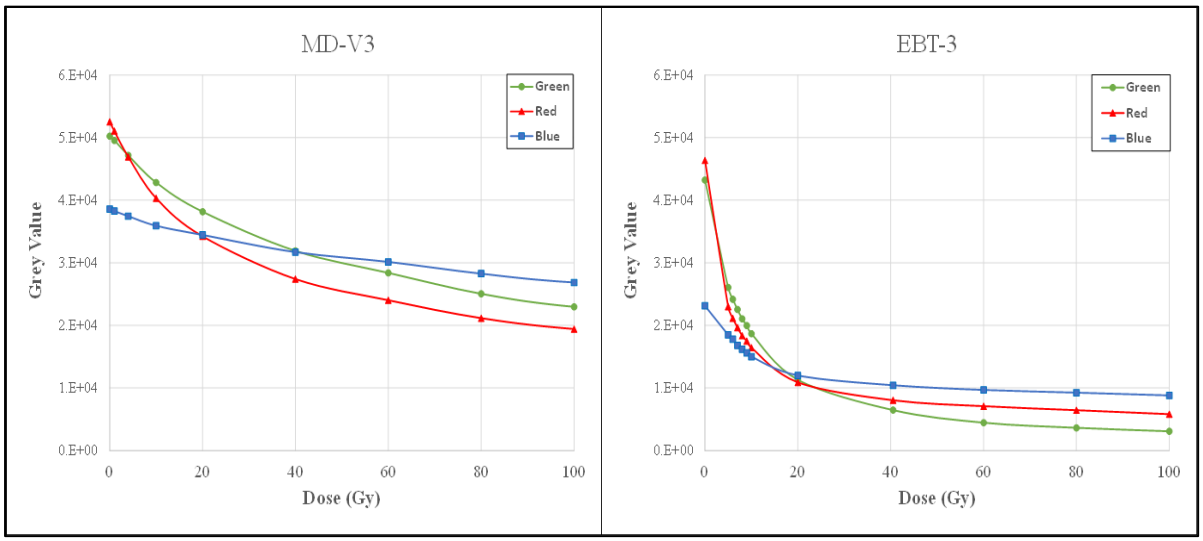

Figure 3-7: The three-channel calibration curve for Gafchromic™ MD-V3 and EBT-3. EBT-3 is more sensitive in dose range ≤ 20 Gy, while MD-V3 can be used for higher doses up to 100 Gy.

movements during long radiation time. As aforementioned, I also employed wider beams (250 µm) instead of narrow beams (<100 µm) to minimize this effect. As it is clear in Fig 3-6d,e, I was able to generate 100 Gy beams that maintained their resolution deep in the live mouse brain.

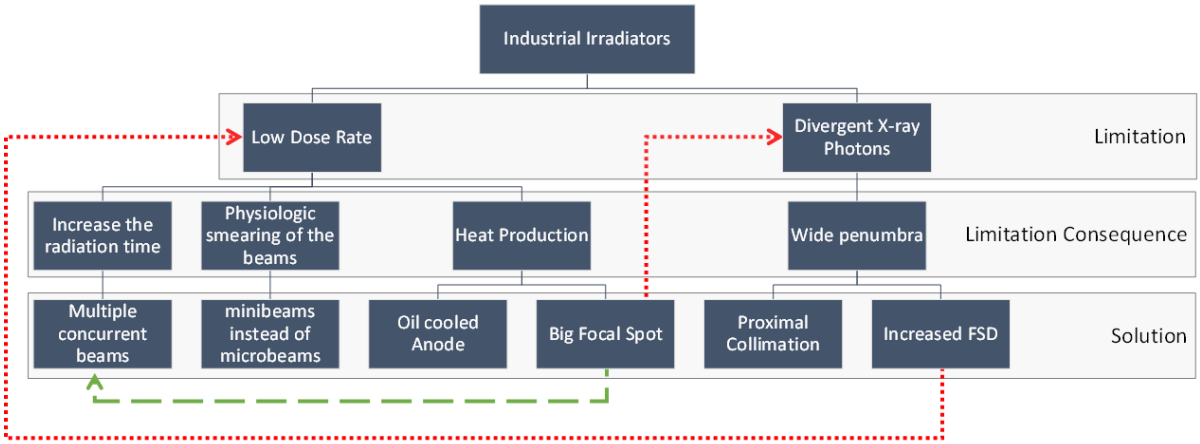

Figure 3-8: The major limitation in using industrial irradiators for applying MRT and our approaches to minimize their effects. Our solutions to one limitation may also help with other one (dashed line) or worsen the effect of another limitation (dotted line).

Another limitation is the fact that the industrial generated X-ray photons are divergent and, in combination with big focal size, generates a wider penumbra that increases the valley dose deep in the tissue (Fig 3-9b). Several histological studies support the idea that surviving cells in the valley regions, and consequently the valley doses, play the crucial role in maintaining tissue function[73,75,96,97]. As a result, a narrower penumbra is desired. We utilized the following consideration to minimize the penumbra.

1. In contrast to previous studies[32,82], I used a proximal collimation (collimator was close to the target instead of radiation source) (see Fig 3-9b).

2. As it is shown in Fig 3-9c, there is an inverse relation between penumbra and FSD. On

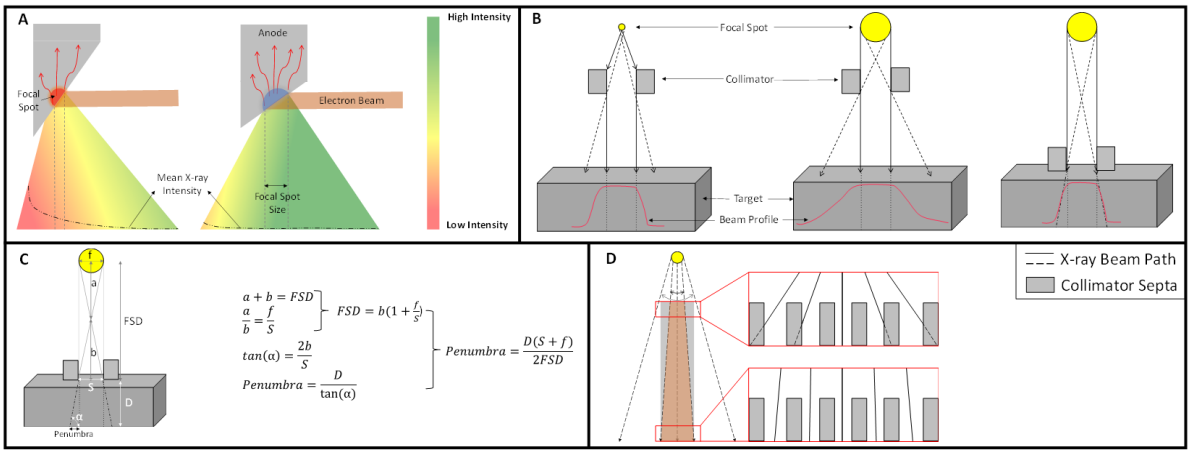

Figure 3-9: A) the comparison of the generated beam intensity between a small (left) vs. large (right) focal spot irradiator; B) The comparison in generated beam profile deep in the tissue in small (left) or large (middle and right) focal spot irradiator are used and the collimator is placed near the source (left and middle) vs. near the target (right); C) The equation demonstrates in large focal spot irradiators, penumbra has inverse relation with the focal spot to surface distance; D) The schematic shows that by increasing the FSD, parallel septa in collimator can be used, and wider radiation field can be covered. The rectangle covers equal radiation field, far or close to the source, trapezoid area contains beams with the same degrees.

the other hand, dose rate changes proportional to $(\frac{1}{FSD^2})$. Based on previous studies[98,99], the estimated required dose to induce therapeutic responses with minimal effect on normal tissue range between 150Gy and 300Gy, so to maintain the total treatment duration to less than two hours; according to the approved protocol by IACUC to minimize animal anesthetic effects; the farthest FSD was chosen (FSD=37cm, Dose rate=2.9Gy/min, Collimator relative output factor=0.84). In addition, by increasing the FSD, using parallel-septa collimator was feasible, which eased the design and alignment of the collimator (Fig 3-9d). In conclusion, I have demonstrated a relatively simple and easily reproduced method for applying homogeneous MRT using a small animal irradiator unit. I describe the approach, and the dosimetric characteristics of this method. At its current stage, my method can be used for applying MRT in preclinical studies.

CHAPTER 4 INVESTIGATING AN EFFICIENT AND FEASIBLE DESKTOP APPROACH TO EVALUATE THE TREATMENT POTENCY OF MICROBEAM RADIOTHERAPY: B) EVALUATING THE BIOLOGICAL EQUIVALENCE DOSE

4.1 Rationale:

In chapter 3, I described a collimator that converts the beam of a conventional irradiator to 44 beams (beam FWHM = 246±32μm; center-to-center = 926±23μm; peak-to-valley dose ratio = 24.35±2.10; collimator relative output factor = 0.84±0.04, all at the entrance plan) and the dosimetric characteristics of this method were reported in detail. Here, the biological effects of MRT using this method were investigated.

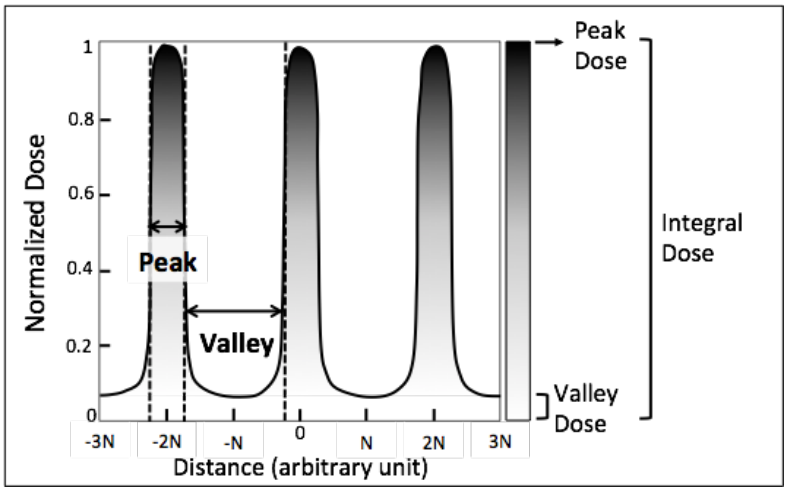

Figure 4-1: The schematic beam profile, demonstrating the different dose component of MRT

One major hurdle in implementing clinical MRT is identifying the optimal irradiation dose. Due to spatial fractionated nature of MRT, the physical dosimetry is more complex than for conventional broad beam radiotherapy (BB) and just evaluate the deposition of energy. In contrast, the radiobiological equivalent dose (RBED) is the dose of MRT radiation, which elicits the same biological effect either *in vitro* or *in vivo* as BB. In addition, the RBED takes

into account the different dose components of MRT: peak, valley and integrated dose (Fig 4-1).

Investigators have utilized various methods to evaluate the MRT equivalent dose. Ibahim et al.[100] tried to find the *in vitro* equivalent dose using clonogenic and real-time cell impedance sensing (RT-CIS)/xCELLigence assays while recently Bouchet et al.[60] demonstrated that the effect of MRT on animal survival is equal to the half valley dose in homogeneous X-ray distribution. While still there is disagreement over the real equal dose, here, the aim was to calculate the RBED of my method *in vitro* using clonogenic assay and *in vivo* by evaluating the acute mouse skin response to the different radiation dose of BB or MRT.

4.2 Approach:

4.2.1 Cell Culture:

B16-F10 cell line was purchased from the Lineberger Comprehensive Cancer Center Tissue Culture Facility, at UNC-CH. A mouse model of glioblastoma, TRP cell line, was a gift by Dr. C. Ryan Miller at UNC-CH[101]. Cells were cultured at 37°C and 5% CO_2 in Dulbecco's Modified Eagle's Medium supplemented with, 100Uml^{-1} penicillin and 100µg.ml^{-1} streptomycin all from Corning Inc. (Corning, NY) and 10% FBS (Serum Source International, NC).

4.2.2 Clonogenic Assay:

In vitro dose responses of B16-F10 and TRP cell lines were evaluated using clonogenic assays with delayed plating after treatment protocol as shown in Fig 4-2[102]. In short, an appropriate number of cells were seeded in 12.5 mm^2 cell culture flasks, grown to ≈90% confluency, and irradiated with different doses of MRT. The flasks were filled with the

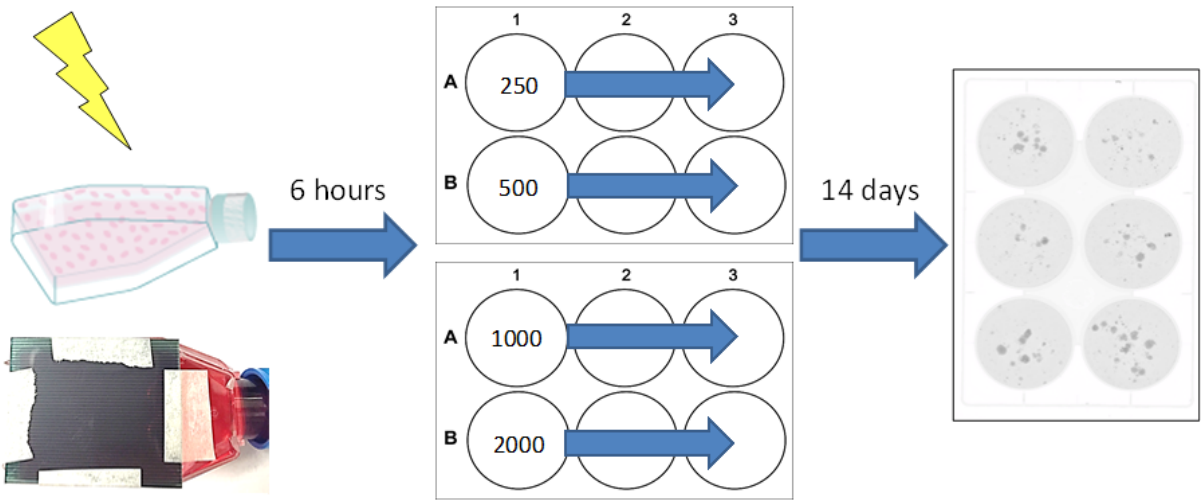

Figure 4-2: Schematic Picture of the Clonogenic Assay protocol to investigate the in vitro effect of MRT on two murine cancer cell lines (B16-F10 and TRP). Left bottom, is a picture of irradiated cell culture flask with attached radiochromic film on the top.

complete media and placed upside down so that the collimator could be placed in close contact with the growth surface. To mimic the subcutaneous tumor dose, 2 mm thick PMMA sheet was placed between the flask and the collimator. The PVDR at the growth surface (4mm depth) calculated to be 15. The control flasks were placed outside of incubator inverted for the equal duration of time, to account for the effect of cell death due to detachment (anoikis) or unfavorable environment (low temperature, humidity, and pH). Six hours following irradiation, a single cell suspension was obtained and an appropriate number of the cells was counted and seeded in each well of a 6-well plate. Colonies were fixed with 70% ethanol, stained with crystal violet two weeks later. After scanning, the colonies were counted using ImageJ (NIH, Bethesda, MD). The minimal pixel size of the particles was defined by measuring the size of a colony consisting of 25 cells for each cell line. The surviving fractions were calculated by the following equations[103]:

$$Platting\ Efficiency\ (PE) = \frac{Number\ of\ Counted\ Colony}{Number\ of\ Platted\ Cells} \times 100;\ \textit{Equation 4-1}$$

$$Surviving\ Fraction\ (SF) = \frac{Colonies\ Counted}{Cell\ Seeded \times PE} \times 100;\ \textit{Equation 4-2}$$

The α and ß were calculated by fitting the survival curve to the following equations using Matlab Curve Fitting toolbox (R2015-a, Mathworks, Natick, MA):

$$SF = \varepsilon^{-(\alpha D+\beta D^2)} \text{ in BB; } \textit{Equation 4-3}$$

$$SF = \varepsilon^{-(\alpha\frac{D}{10}+\beta\frac{D^2}{100})} \text{ in MRT; } \textit{Equation 4-4}$$

where D is X-ray dose in BB and mean peak dose in MRT.

4.2.3 Irradiation and Dosimetry:

An industrial irradiator (X-RAD 320, PXi, North Branford, CT) was utilized as our radiation source. The detailed specification of the irradiator and our setting has been reported before (Chapter 3). For *in vivo* studies, the mouse underwent irradiation under anesthesia that was induced by 3-4% isoflurane and maintained by 1-2% isoflurane in medical-grade oxygen at 0.8-1 L/min flow rate. Except for the irradiation field (radiation field size=1.5cm×1.5cm), the rest of the animal body was shielded with 1 cm thick lead. The anesthetized mouse was laid prone on an in-house designed mouse-holder and the head was fixed using ear bars and nose cone. The mouse body and right hind leg were fixed on the designated holder by medical tape (Transpore™ Surgical Tape, 3M Company, Maplewood, MN) (Fig 4-3). Gafchromic® MD-V2 film was placed on the entrance and exit plan to confirm the dose delivery and for dosimetry measurements (Fig 4-3c). The films were scanned and analyzed using the protocol we reported before (Chapter 3).

4.2.4 *In vivo* Mouse Studies:

Five to six-weeks-old female C57BL/6J mice were obtained from Jackson Laboratory (Bar Harbor, ME) and maintained under the pathogen-free condition in the UNC-CH Division of

Laboratory Animal Medicine temperature and light-controlled designated environment with 12-h light/dark cycle (lights on at 7 AM) and provided food and water. All the experiments were performed according to approved by UNC-CH IACUC.

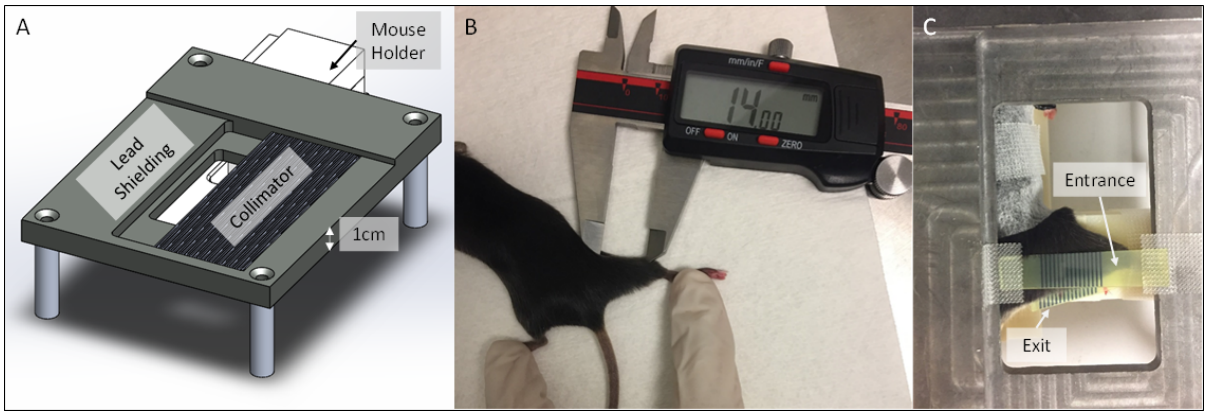

Figure 4-3: The in vivo studies setting. A) For all experiments, the anesthetized mouse was fixed on an in-house mouse holder and all the body except irradiation field was covered with a 1cm lead. Note that the collimator is not shown all the way to the left to enable seeing the underneath shielding and mouse holder; B) The radiation field was 1.5cm×1.5cm to cover the entire mouse thigh; C) Two pieces of Gafchromic® MD-V2 films were placed at the entrance and exit plans for dosimetry purpose.

4.2.5 Acute Skin Injury:

The hind limbs of mice were shaved and right legs were irradiated with different dose of BB or MRT (5 mice in each group) and observed 3 times a week for the appearance of acute skin effect up to one-month post-irradiation. The contralateral legs served as the control. Upon appearance, the skin effect was scored based on the scoring system, illustrated in Table 4-1[104,105].

Table 4-1: Radiation Therapy Oncology Group Scoring System for Acute Radiation Skin Injury

Score	**0**	**1**	**2**	**3**	**4**
Observation	No change over baseline	Erythema; dry desquamation; epilation	Bright erythema; moist desquamation; edema	Confluent moist desquamation; pitting edema	Ulceration, hemorrhage; necrosis

4.3 Results:

4.3.1 Calculating *in vitro* dose equivalence between BB and MRT (clonogenic assays):

Using clonogenic assay, the responses of two murine cell lines, B16-F10 and TRP, to different doses of MRT and BB were evaluated. All the results for BB and MRT were obtained from at least three samples. The surviving fractions were calculated using Eq.4-2. and are shown in Fig 4-4. The data were fitted to linear-quadratic survival equation (Eq.4-3&4-4) and *in vitro* RBED were determined, considering the same fraction of cells survives the equivalent dose (Table 4-2). α, β and R^2 values are presented in Table 4-3.

4.3.2 Calculating *in vivo* dose equivalence between BB and MRT (acute skin reaction):

To determine the *in vivo* RBED, the right thighs of mice were irradiated with graded doses of BB and MRT and the acute skin reaction to the radiation was scored (see Table 3-3). The mean ± SEM of the scores in each group is demonstrated in Fig 4-5. The highest radiation doses that did cause any skin damage in either of approaches (MRT or BB) were considered *in vivo* RBEDs. Based on my observations MRT=150 Gy on peak induced the same skin effect as BB=15Gy. According to *in vitro* survival curve, 9.1×10^{-4} percent and 2.3×10^{-9} percent of cells survive after 15 Gy of BB and 150 Gy of MRT_{peak}, respectively. This finding promises the higher therapeutic window in MRT.

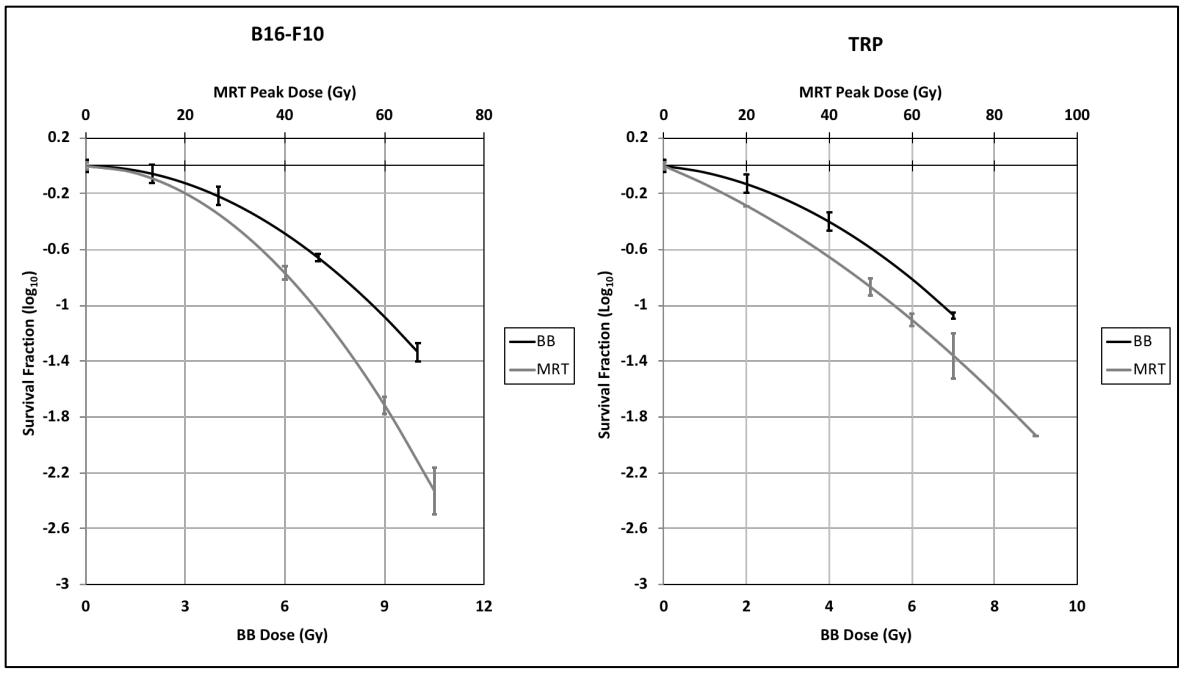

Figure 4-4: Cell Survival Curves. Surviving fraction vs. BB dose and MRT peak dose of two different murine cell lines (B16-F10 on the left and TRP on the right), evaluated using the clonogenic assay.

Table 4-2: In vitro Radiobiological Equivalent Dose.

	B16-F10	**TRP**
BB (Gy)	**MRT Peak (Gy)***	**MRT Peak (Gy)***
2	10	10
5	26	37
7	37	59
10	53	94
20	107	219
50	268	607

4.4 Discussion:

As a proof of principle, and to investigate the efficacy of my method *in vitro*, the response of two-cell lines using clonogenic assay was evaluated and the cell survival curve was generated (Fig 4-4). This assay measures the ability of a single cell to form a colony and is based on the idea that for a tumor to be eradicated, it is only necessary to render its consisting cells unable to proliferate indefinitely[103]. When compared to the survival curve of these two cell lines after BB, we found that 5 Gy of BB will induce comparable *in vitro* effect to almost 37 Gy and 26 Gy of MRT in TRP and B16-f10, respectively.

Higher α and β was found in both TRP and B16-F10 cell lines (Table 3-5). This observation demonstrates that cells can tolerate the low dose of MRT better than BB, but at the higher dose, MRT can eradicate tumor cells more efficiently.

Due to the distinct spatial fractionation of X-ray beam in MRT (Fig 4-1), finding the actual equivalence dose of MRT is convoluted and studies have used different assumption for the physical or biological equivalent dose.

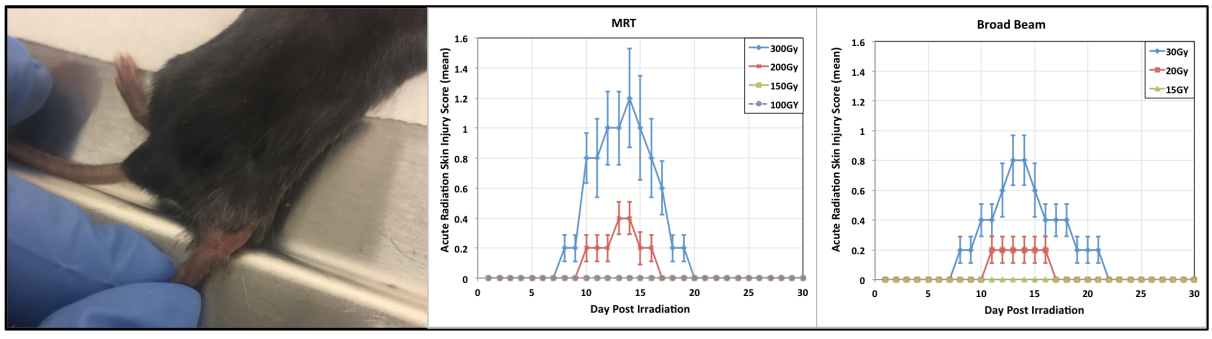

Figure 4-5: Normal Tissue Radiation Injury. The image on the left demonstrates a mouse with score 3 post-irradiation acute skin Injury. Mean score of acute skin injury up to 30 days post-irradiation with different MRT peak and BB peak doses (n=5 per group). Error bars are SEM.

An *in vitro* model does not take into account the interference of other factors, such as neovascularization or immune modulation, with the response of tumor cells to X-ray after MRT or standard RT irradiations. As a result, the *in vivo* RBED would be the optimal method. Here, the effect of two irradiation modality on normal skin tissue was evaluated to calculate the *in vivo* RBED, since in future I planned to investigate the therapeutic effect of MRT on flank tumors.

Although in the initial MRT experiments ultra-high dose of X-ray up to thousands of Gys have been utilized[106], recent studies demonstrated the toxicity effect appears at much lower doses[107]. Serduc et al. found the toxicity is directly correlated to peak width. Using our approach, 150Gy is the maximum MRT peak dose that did not induce skin effects. The toxic dose using our method was lower than synchrotron MRT[108]. In synchrotron based MRT studies, normal tissue toxicity is more dependent on valley region parameters because: (1) ultra-high dose of X-ray destroy all cell along the beam path, and (2) the beam size is approximately 25μm–50μm, spaced at 200 μm–400 μm on center and consequently, most of the tissue in the radiation field receives the valley dose. In the current study, the beams to valley width ratio is larger than with synchrotron microbeams (24 at the skin level and 15 at the cell growth surface), so higher normal tissue toxicity than equivalent valley dose was expected.

The generated beams using my method are almost 250μm, that are below the threshold (beamwidth ≥ 400 μm) that induces permanent destruction of normal tissue microvasculature[76]. However, it should be noted that synchrotron sources may induce a different biological response due to the extremely high dose rates, which should be evaluated by scientists at these facilities.

In conclusion, the new collimator-approach for applying MRT can be effectively be utilized for preclinical and biomedical studies. This method is able to induce radiobiological cell death *in vitro* which promises its treatment efficacy. The high tolerance of normal mouse skin to doses up to 150 Gy is a sign of potentially higher therapeutic window in this technique. In next chapter, the effect of this modality on orthotopic melanoma model would be evaluated.

Table 4-3: Calculated α and β values and goodness of fitted curve.

Cell Line	**Irradiation Method**	**α^***	**β^***	**R^2**
B16-F10	BB	.002±.07	.031±.02	.96
	MRT	.01±.11	.11±.05	.98
TRP	BB	.031±.05	.02±.008	.99
	MRT	.12±.04	.01±.005	.99

CHAPTER 5 INVESTIGATING AN EFFICIENT AND FEASIBLE DESKTOP APPROACH TO EVALUATE THE TREATMENT POTENCY OF MICROBEAM RADIOTHERAPY: C) EVALUATING THE MICROBEAM TREATMENT EFFICACY

5.1 Rationale:

In last two chapters, it was demonstrated that I made a new approach for applying MRT using conventional kilovoltage small animal irradiator. The most important specification of this method is its easiness of reproducibility. Since I published the initial characteristics and feasibility of this modality, other groups also adopted it[109].

In current chapter, the ultimate goal is to investigate the therapeutic effect of this novel approach since the ultimate goal of the MRT is to treat cancer. It has been shown in chapter 4 that utilizing this technique, I was able to induce the radiobiological cell death, *in vitro*. I also evaluated the radiobiological equivalent dose (RBED) of MRT and BB both *in vitro* and *in vivo*. Here, I will use the *in vivo* RBED (150 Gy_{MRT}=15 Gy_{BB}) to compare the effect of MRT and BB on orthotopic melanoma tumor model.

It worth mentioning that in the current study the peaks were almost 250 μm wide, spaced every 900 μm. As a result, most of the field of the radiation received the valley dose, which was less than 15 Gy (PVDR=24). Consequently, a treatment efficacy equal or less than BB was expected.

5.2 Approach:

5.2.1 Mouse Model:

For detailed information regarding the mouse model please see section 4.2.4.

5.2.2 Therapeutic Effect:

The method for cell growth can be found in section 4.2.1. The cells were harvested and prepared based on Overwijk et al. protocol[110]. The appropriate number of the cells (8×10^4 cell) in 100 µL Hank's Balanced Salt Solution (Corning Inc. Corning, NY) was injected s.c to the right thighs of the mice (Day 0). One week later, mice were randomly assigned in three groups as indicated. After Irradiation, mice were weighted and the perpendicular tumor diameters were measured using digital calipers thrice a week. Tumor volume was calculated using the formula $L\times W^2\times0.52$, where L is the longest dimension and W is the perpendicular dimension. The mice were humanely sacrificed when the tumor volume reached $1.5cm^3$ to decrease the morbidity. The study concluded 60 days post-injection.

5.2.3 Irradiation:

The mice in BB and MRT groups received radiation on the inoculation site on Day 8. The setting is described in section 4.2.3 and demonstrated in Fig 4-3. The X-ray doses were selected as the *in vivo* RBED (BB=15 Gy and MRT=150 Gy on peak; See Chapter 4 for more detail).

5.2.4 Statistical Analysis:

For all analysis, a p-value < 0.05 was considered statistically significant. The sample size power was evaluated using PROC POWER, SAS version 9.4 (SAS Institute Inc., Cary, NC).

Statistical analysis was performed by SPSS version 22 (IBM, Armonk, NY). Differences in survival were determined for each group by the Kaplan–Meier method and the p-values were calculated by the log-rank test. The mice with metastatic tumor growth were excluded. The one-way analysis of variance (ANOVA) and nonparametric Kruskal–Wallis were used to determine whether there were any significant differences between the mean tumor volume at different time points and median time to progression of groups, respectively.

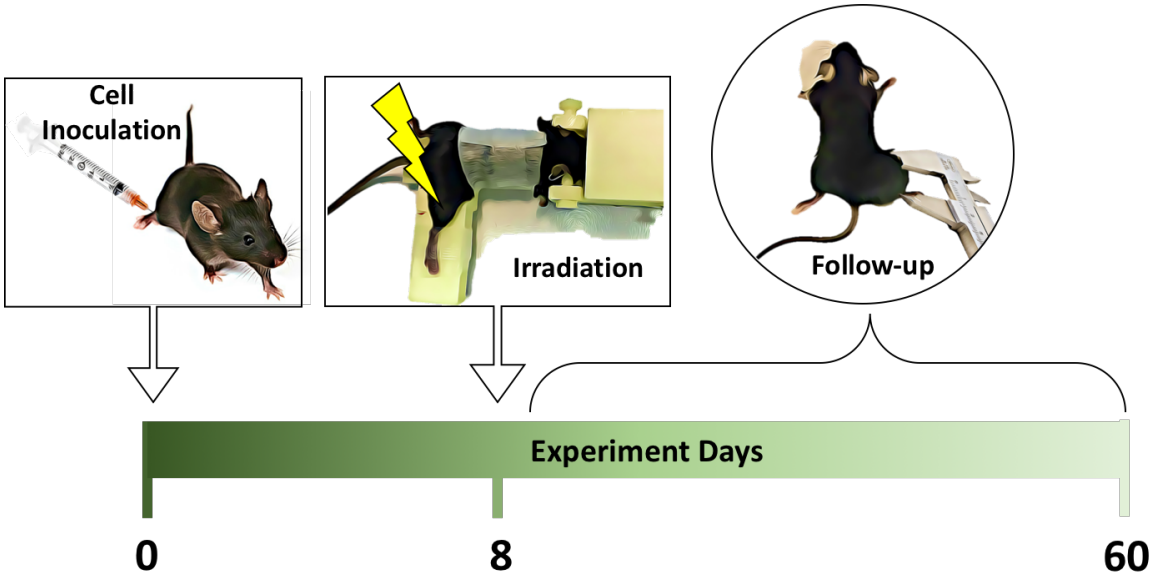

Figure 5-1: The abstract methodology for evaluating the therapeutic efficacy of MRT

5.3 Results:

The *in vivo* therapeutic effect of our method was investigated using a murine model of melanoma by applying RBED of each modality (MRT=150 Gy; BB=15 Gy). It was found that applying MRT using the current setting and doses was more effective in controlling the tumor growth rate than BB ($p<.001$) and ablated the tumor in one out of 11 mice in MRT group (9% chance of ablation) (Fig. 5-2). It worth mentioning that BB is not an effective treatment for B16-F10 even when higher dose (20 Gy) is applied[111].

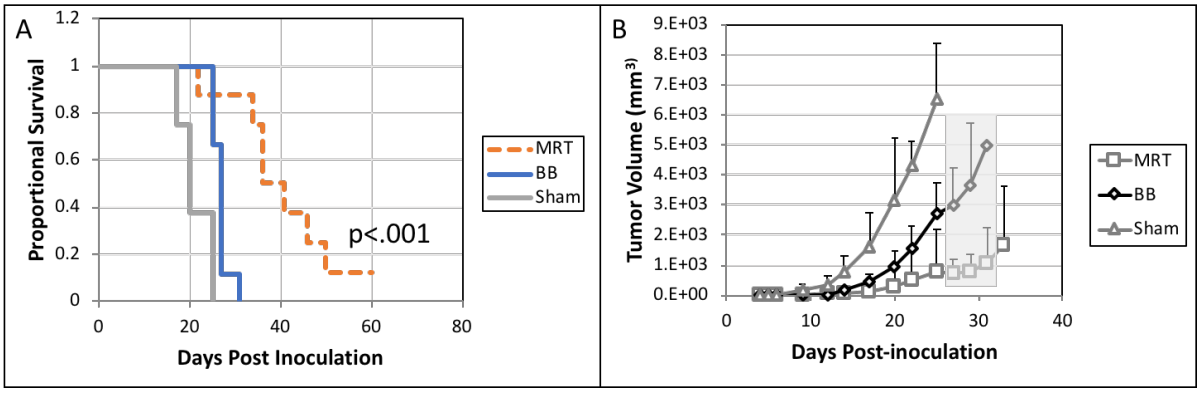

Figure 5-2: Mice treated for flank melanoma. Survival (A) and mean tumor volume ± SEM (B) without treatment or after either BB or MRT. P-value for survival is by log-rank. Shaded area in B demonstrates the time-points where the tumor volume between BB and MRT was statistically significant.

5.4 Discussion:

A significant difference was observed between the therapeutic effect of MRT and BB on a murine model of melanoma.

Several hypotheses have been postulated to explain the wider therapeutic index of MRT:

1. The spatial fractionation pattern of MRT provides higher contact surface between radiated and non-irradiated tissue. This higher contact area would increase the chance of healing. In addition, micrometer dimension of the destroyed zone would magnify the ability of the healthy tissue to compensating for the cell in the beam path.
2. MRT may activate a different bystander response than BB that favors the tissue healing in normal tissue and facilitates the tumor ablation[57].
3. During the initial MRT studies at synchrotron facilities, ultra-high doses of irradiation (in the magnitude of thousands) were delivered to the different animal organs, especially the brain, to investigate the tolerance of normal tissue. During this period researchers observed that in the beam path, the endothelial nuclei was preserved while neurons, oligodendrocytes, and astrocytes were ablated[6]. Furthermore, studies performed over the

past decades have confirmed the therapeutic efficiency of MRT for different types of orthotopic tumor models and found the selective tissue sparing effect of MRT. Overall, these observations formed the foundation for the idea that normal and tissue vessels respond differently to MRT[58].

4. A different immune response may be activated after MRT than BB[112]. This hypothesis will be discussed in detail in Chapter 6.

In conclusion, we found that my approach for applying MRT is more robust than conventional radiation in treating the mouse model of melanoma.

CHAPTER 6 PRELIMINARY STUDIES INTO THE MECHANISM OF THE MICROBEAM RADIOTHERAPY EFFECT ON IMMUNE RESPONSE

6.1 Rationale:

Every day numerous healthy cells acquire changes and become potential cancer cells in the body, but for these cells to be able to form a cancer, they have to have a series of characteristics, known as "Cancer Hallmarks", as demonstrated in Fig 6-1. These hallmarks involve six biological capabilities acquired during the multistep development of tumors, among them is the ability of the tumor cell to avoid immune destruction[113]. In this section, first an introduction to immune system will be given, then the effect of radiotherapy on the immune system will be discussed in detail. Later, the hypothetical advantages of the MRT over conventional radiation will be overviewed. These hypothetical beneficial effects provoked me to test the role of immune response in controlling tumor growth after MRT.

6.1.1 Immune system:

6.1.1.1 Overview:

The immune system is our defense against a wide variety of pathogens. It can be classified into two subsystems: the innate immune system and the adaptive immune system (Fig 6-2).

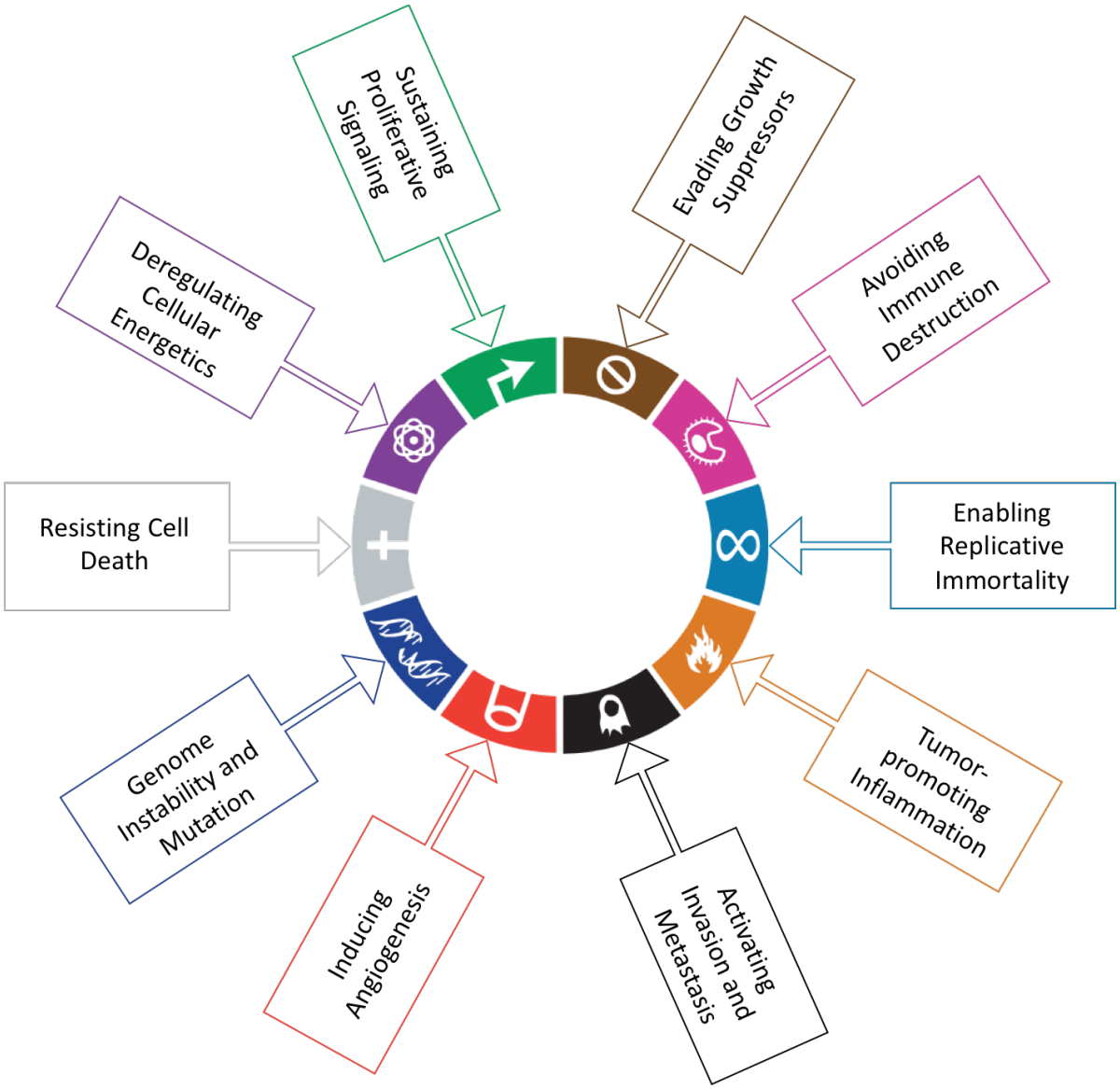

Figure 6-1: Hallmarks of cancer

The innate immune system is the dominant subsystem. It is the first line defense. Exposure to the pathogen will elicit an immediate and maximum reaction in this system. However, its response is nonspecific, which means the innate immune system reaction to different pathogens is identical. Furthermore, this system does not hold any long-lasting memory. Innate immunity comprises four types of defensive barriers:

1. Anatomical or physical
2. Physiological (Temperature, pH, and chemicals like lysozymes, complement, and some interferons
3. Phagocytic (monocytes, neutrophils, macrophages). The cells of the immune system will be described in detail in section 6.1.1.2.
4. Inflammatory events

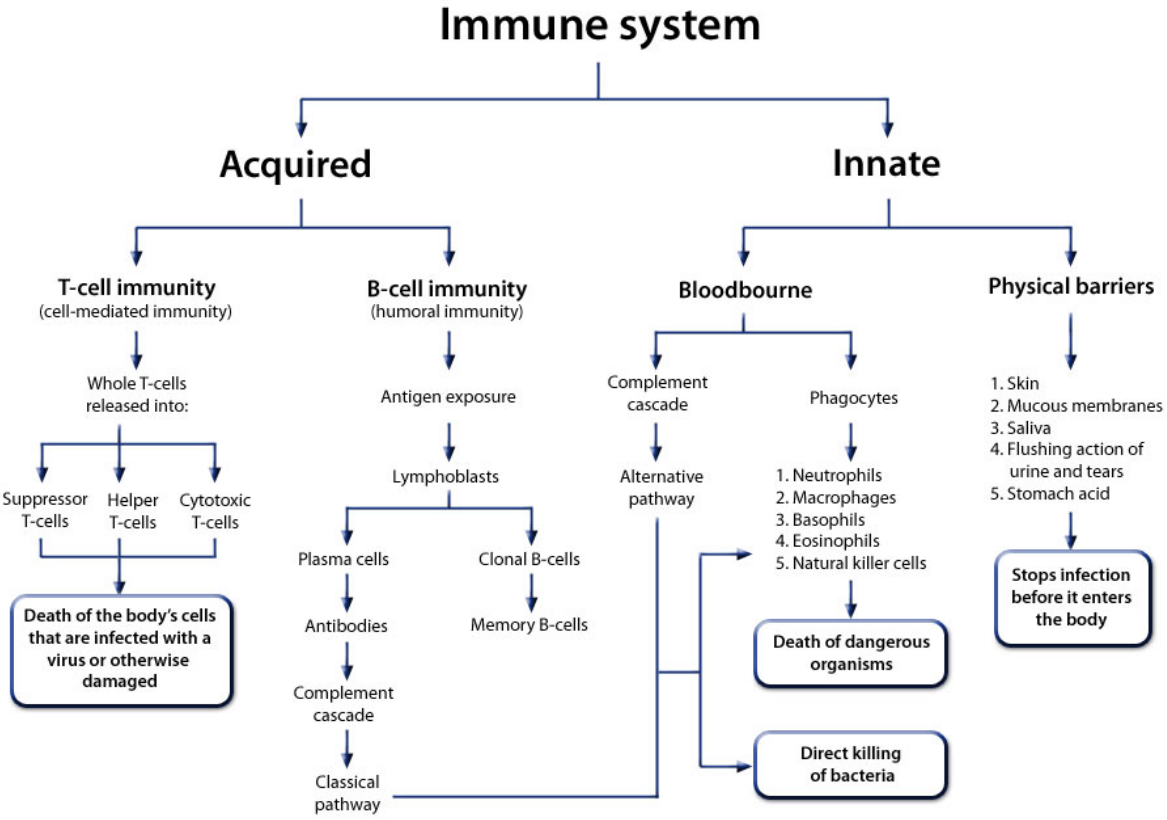

Figure 6-2: Flowchart of immune system

The acquired immune system, also known as the adaptive immune system, is another subsystem that creates the immunological memory of a pathogen. This process of acquired immunity is called vaccination. The vaccination effect can provide long-lasting protection. Interestingly, the adaptive immune response enhances to subsequent encounters with the same

pathogen. In contrast to the innate immune system, the adaptive immune system acts specifically to each pathogen.

A point to consider is that the innate and adaptive arms of immune response do not operate independently. For instance, although dendritic cells are part of the innate immune system, they enhance the activation of T-cell lymphocytes and consequently, acquired immune response.

6.1.1.2 Cells of the immune system:

The cells of the immune system can be categorized in two groups based on their origin in bone marrow: myeloid or lymphoid originated cells (See Fig. 6-3). Cells of the myeloid heritage are considered members of the innate branch of the immune system, while almost all of the lymphoid lineage is part of the acquired immune system. Accordingly, the acquired immune system can be divided into two branches: humoral immunity (B lymphocytes) and cell-mediated immunity (T lymphocytes). Humoral immunity is directed toward the defense against extracellular microbes or antigens using antibodies synthesized and secreted by B lymphocytes or their fully differentiated end cells, the plasma cells. In contrary, the cell-mediated arm of the acquired immune system is designed to identify and eradicate antigen stimuli that arise from inside the cells of the body, which activates when cells become infected by intracellular pathogens, namely viruses, or when the malignant transformation of the cell causes the expression of atypical molecules on the cell membrane.

Here, since the goal is to study the immune system in relation to cancer, the focus is on the cell-mediated immune system and other cells of the immune system are discussed according to their relationship with the T-lymphocytes.

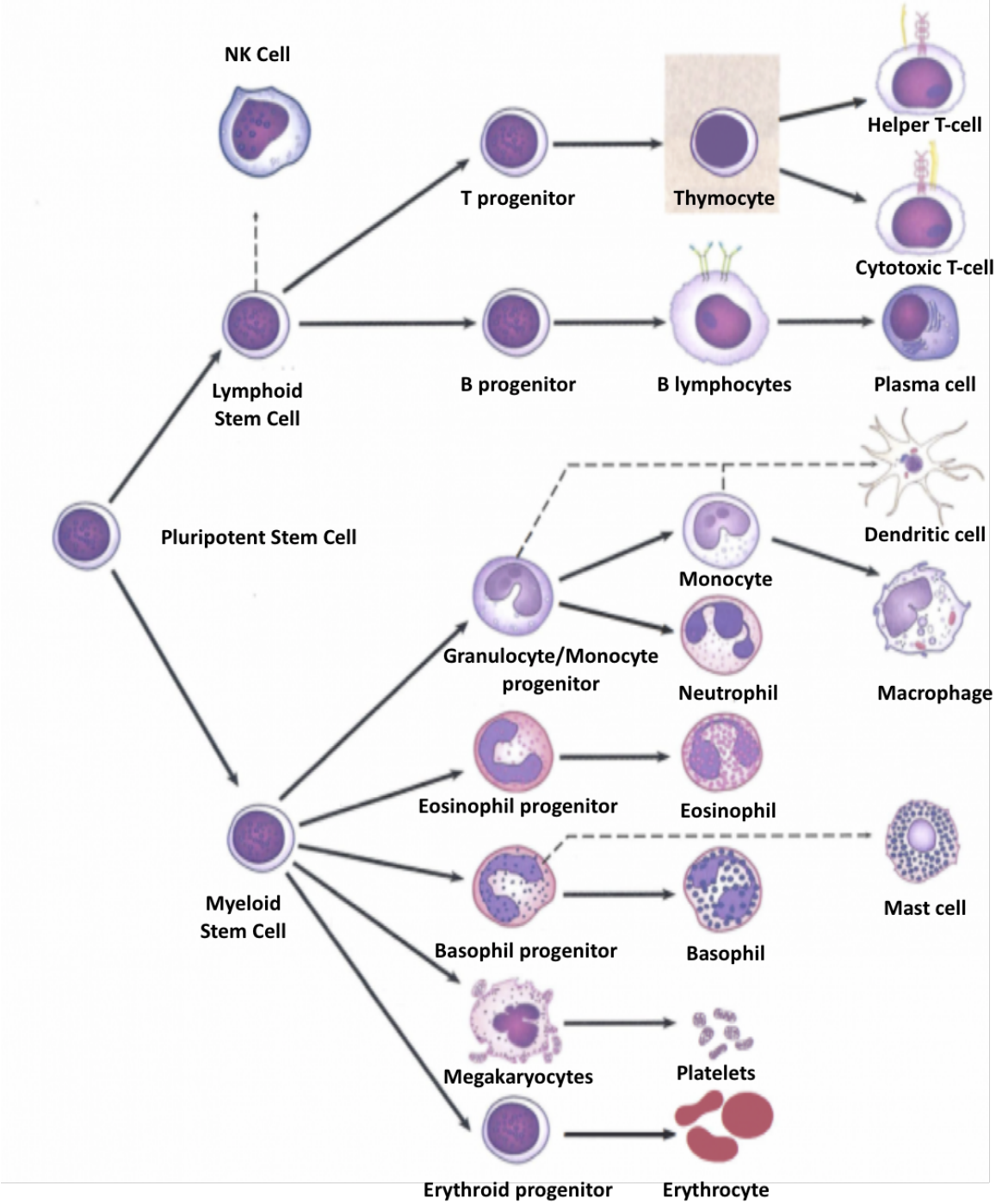

Figure 6-3: The ontogeny of immune cells

6.1.1.3 The generation of cell-mediated immune response:

After the generation in bone marrow, immature T-cells transport to the thymus, where they undergo a two-step selection. The detail of this process is beyond the scope of the current study, but in short, all the cells that have an affinity to the host antigens are eradicated. The surviving cells, called naïve T-cells, reside in the secondary lymphoid tissues, namely lymph nodes. Each naïve T-cell has a unique type of molecule on its membrane, called the T-cell receptor (TCR). The TCR binds to antigenic peptide presented by a membrane-bound molecule known as major histocompatibility complex (MHC), that called human leukocyte antigen (HLA) in humans. There are two types of MHC in humans: class-I and class-II.

Table 6-1: Classes of human leukocyte antigens (HLA)

Class-I HLA			Class-II HLA		
HLA-A	HLA-B	HLA-C	HLA-DP	HLA-DQ	HLA-DR

Class-I molecules are expressed on all nucleated cells in the body, as well as platelets. Each cell expresses two A, two B and two C, one inherited from each parent. A small groove in this molecule is designated to accommodate a small peptide to be presented to the TCR.

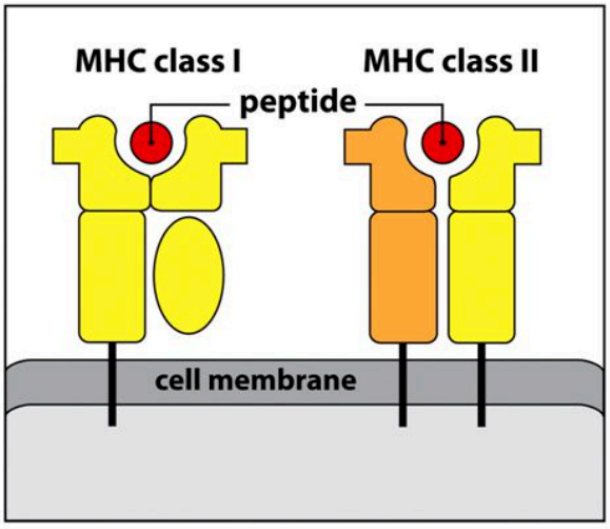

Figure 6-4: Classes of MHC

Class-II molecules are explicitly expressed on the membrane of antigen presenting cells (APCs). APCs involve different immune cells mainly dendritic cells, macrophages, and B-lymphocytes, but dendritic

cells, with their long processes, are the most efficient of these cells[114,115]. There is a groove at the extracellular end of the molecule to hold the peptides to be presented to TCR.

Based on their affinity to MHC classes, T-lymphocytes are further categorized into two groups. First, helper T-cells (THs) that recognize class-II MHC and are CD4+ and second, cytotoxic T-cells (CTLs) that have a high affinity to class-I MHC and are CD8+.

Proteins synthesized in the cell cytosol are routinely degraded in proteasomes, and the peptides from these proteins are transported into the endoplasmic reticulum. The class-I MHC molecules are synthesized in the endoplasmic reticulum of the cells and the peptides are loaded there by the endogenous pathway. These MHC-peptide complexes are then transported to the cell membrane to be presented to CD8+ T-lymphocytes. On the other hand, professional APCs load partially degraded peptides they have ingested, into the groove of MHC-II molecules through endosomal pathway. Within few hours of the initial encounter to the antigens, the APCs that have phagocyted and processed the antigens begin to leave the area and enter the lymph nodes where they present their loaded MHC II to THs. The detailed description of endogenous and endosomal pathways is beyond the scope of my dissertation, but it worth mentioning that the cancer cells are able to suppress the expression of MHC-I on their surface, and consequently render themselves invisible to CTLs.

T-lymphocytes need multiple steps signals for activation. The binding of the TCR of the T-cells to the MHC-peptide complex is the first signal of T-cell activation. Several costimulatory molecules are involved in the second signal:

- CD8 and CD4 bind with MHC-I and II, respectively.
- Integrins on T-cells (LFA-1) bind to IgCAMs on cells (ICAM-1) to increase the cell-cell adhesion.

- IgCAMs on T-cells (CD2) bind to integrins on cells (LFA-3) for the same purpose.
- CD28 on T-cells binds to B7 on the cells. CTLA-4 (CD152) competes with CD28 for binding to B7 and acts as a down-regulator.

The last step of activation signals are cytokines, excreted by T-cells or APC.

The naïve THs then give rise to different classes as demonstrated in Fig 6-5. My main focus here will be on TH1s and regulatory T-cells (Tregs), that enhance and suppress the anti-tumor immunity, respectively.

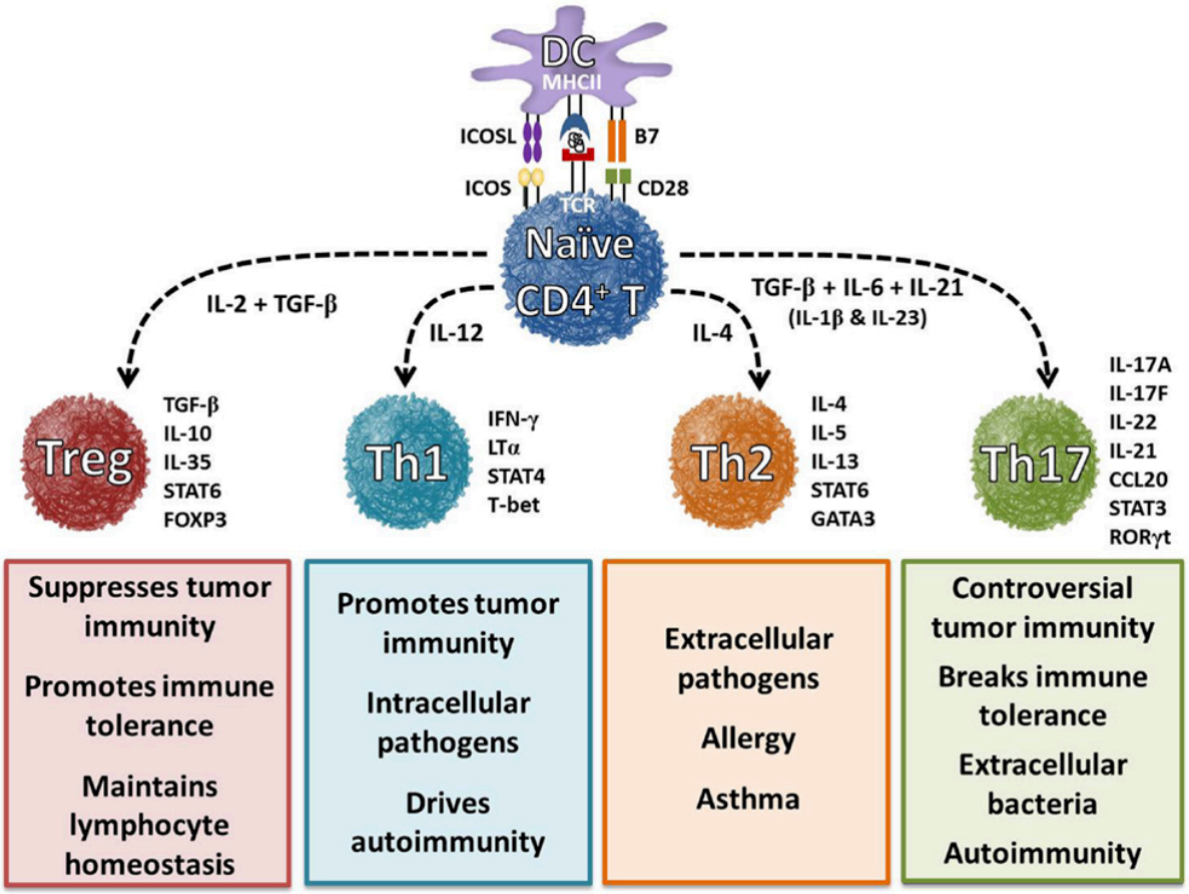

Figure 6-5 Subsets of helper T-cells

CTLs are capable of differentiating and cloning by themselves in the presence of the class-I MHC bonded antigen stimulation, but they are more effective if they are assisted by TH1. After activation, CTLs attach to the target cells and induce apoptosis.

Another mechanism enhanced by the action of TH1 cells is natural killer cells (NK cells). NK cells are the only member of lymphocyte heritage that belongs to the innate immune arm. Like CTLs, they induce apoptosis in the target cells, but unlike THs and CTLAs, they act non-specifically and they won't produce any memory.

After the initial immune response, the activated T-cells, except a minority of THs, start to die and the remnant cells form the memory. Unlike naïve T-lymphocytes, the memory cells do not reside in the secondary lymphatic tissues, but they tend to go back to the type of tissues they first encountered antigen.

6.1.2 Immune escape mechanisms of tumor:

As reviewed in the previous section, the immune system contributes to tumor control. But through multiple processes, cancer cells can evade the immune destructions, as listed in Table 6-2. Dunn et al. proposed "immunosurveillance and immunoediting" model to describe the dynamic interaction between immune system and cancer cells[116]. According to this model, in early phases of tumor growth, the immunogenic tumor cells are eradicated, while less immunogenic tumor cells survive (See Type A mechanism in Table 6-2). Later in course of the disease, the evolving tumor microenvironment restrains the access of other immune cells to cancer cells through forming irregular microvasculature. In addition, the tumor microenvironment also suppresses the infiltrated CTLs by inducing hypoxia and lowering the pH, for instance. In final stages, tumors avoid the immune elimination by various mechanisms

Table 6-2: Immune-evade mechanisms of cancer cells[117]

A. Tumor cell-related mechanisms	Rapid proliferation rate	
	Decreased MHC-I expression	
	Selection of immuno-resistant variants	
	Antigen shedding	
	Production of immune suppressive cytokines	
	Resistance to tumor killing mechanisms	
B. Microenvironment-related mechanisms	Development of hypoxic regions	
	Aberrant tumor vasculature	
	Extracellular environment with acidic pH	
C. Immune-cell related mechanisms	I. Tumor infiltrating cytotoxic T cells	Impaired lytic activity
		Alterations in TCR signaling
		Secretion of immune suppressive cytokines
	II. Tumor infiltrating Treg cells:	Increased cytotoxic T cell suppressing capacity
		Increased expression of PD-1
		Increased TGF-β production
	III. Tumor infiltrating DCs:	Altered expression of costimulatory molecules
		Deficient CD8+ cross-priming
		Enhanced expression of co-inhibitory molecules
		Inefficient recruitment and maturation in the tumor
		Increased TGF-β production
		High plasmacytoid and low myeloid DC levels in tumors
	IV. Tumor infiltrating macrophages:	Shift to the M2 phenotype within the tumors
		Enhanced expression of co-inhibitory molecules
		Low levels of NO production
		High levels of arginase production

namely the elaboration of cytokines such as TGF-β. These cytokines mainly suppress the cell-mediated immune response and enrich the tumor microenvironment with immunosuppressive populations of cells, particularly Treg, plasmacytoid dendritic cells[118] and tumor-associated macrophages[119]. These cells further secret the immune suppressor cytokines and, as a result of

this positive feedback loop, tumors can grow uncontrollablly "invisible" to the immune response.

6.1.3 Radiation therapy and the immune system:

6.1.3.1 Effect of conventional radiation therapy on the immune system:

Immune cells, CTLs in particular, are radiosensitive[120]. Consequently, high dose radiotherapy has been, for long, considered to be immunosuppressive. However, in contrast to chemotherapy, the immunosuppressive effect of radiotherapy is confined to the irradiation field. Now, various aspects of immune stimulating potential of radiation, both on innate and adaptive immunity, are evident. The detailed effects can be found in Fig 6-6, but here I only discuss a few.

Various studies on murine and human cell lines have confirmed that radiation induces the cancer cells to express MHC class-I on their surface[121–124]. As mentioned before (See section 6.1.1.3), these membrane-attached proteins present the inner cells antigens to T-cells. Cancer cells usually under-express them in attempt to escape immune destruction (Table 6-2). This effect of radiation is dose-dependent, which means the higher the radiation dose, the greater proportion of tumor cells undergo this transformation[121–124].

It has been shown in different types of cancer cells, that only high dose of radiation induces the upregulation of ICAM-1. This marker attaches to LFA-1 on the surface of T-cells and stimulate the naïve T-cell activation and subsequently, cell-mediated immunity[123,124].

The irradiated melanoma cells secret IFN-γ, which in turn increases the MHC-I expression[125]. Radiation also induces immunogenic cell death, which reveals the intercellular antigens to

immune cells[126]. This process enables the APCs to effectively activate the naïve T-cells against tumor neoantigens.

In addition, radiotherapy through sensitizing immune cells, not only promotes local tumor control but also these highly mobile cells can travel to distant sites of body and destroy the metastatic lesions. Indeed, this is presumed to be the fundamental of a phenomenon called "abscopal" effect of radiotherapy[127].

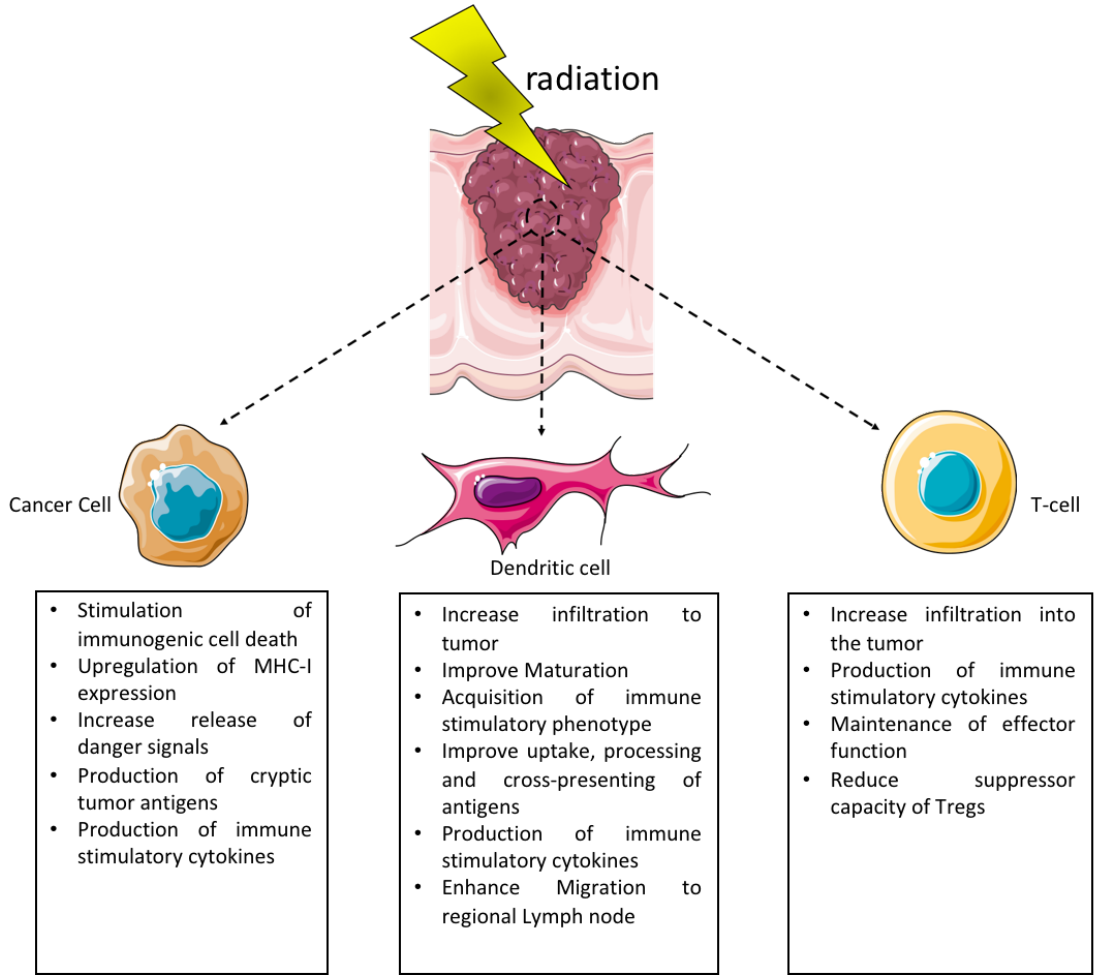

Figure 6-6: Immune stimulatory effects of irradiation[117]

On the other hand, it should be mentioned that irradiation also has immunosuppressive effects. These effects can shift the balance in favor of tumor proliferation by inhibiting the

efficacy of immune response[128]. Irradiated dendritic cells are less effective in stimulating T-cells, with lesser cytotoxic activity against antigen-specific targets and decreased secretion of cytokines required to prime a helper T-cell response[129]. Some researchers also suggested that radiation could also influence the tumor-associated macrophage phenotype and promote stromal remodeling and tumor growth[130]. Consequently, an irradiation strategy is needed to overcome this paradoxical effect and enhance the immune stimulatory arm of radiation.

6.1.3.2 Why MRT is superior to conventional radiation therapy in activating the immune system; Hypotheses:

Aside from the immunogenic effects of conventional radiotherapy, MRT may has several more beneficial effects on immune system as follows:

1) As mentioned earlier, T-lymphocytes are the effective arm of immune system against cancer cells, but they are radiosensitive[120]. During conventional radiation, the homogenous dose distribution damages the tumor infiltrating lymphocytes. In contrast, MRT, by its unique spatially fractionated pattern, provides more contact area between irradiated and non-irradiated area, which in turn, offers greater opportunity for T-cells in valley area to interact with the damaged tumor cells in the peak.
2) During necrosis the cell membrane integrity is lost, which reveals the intercellular antigens to immune cells, in contrast to the more orderly cell death of apoptosis[131]. Higher radiation doses result in higher percentage of cell-death through necrosis[126]. In MRT, as mentioned before, the tumor tissue is irradiated with significantly higher than conventional doses in the peaks, which, in theory, increases the necrosis over apoptosis ratio.

3) Intermediate dose exposure, such as what happens in the valley area due to scatter effect, have also shown to stimulate immune function by stimulating natural killer (NK) cells and proliferation of T-cells which both play critical role in anticancer immune response[132]. In addition, low dose radiation decreases the phagocytosis of macrophages, also making more antigens available[133].
4) Radiotherapy enhances the surface degradation of MHC class-I molecules that represents intracellular antigens[121–124]. Sprung et al. in a genome wide study using microarray demonstrated that expression of class-I MHC antigens increases 4-48 hours after microbeam radiation[112].
5) Dendritic cells are a member of APCs that process and present antigens to T-cell lymphocytes. These cells need more than 48 hours to migrate to the tumor, absorb the antigens, maturate and migrate to lymph node to simulate CD8+ cytotoxic lymphocytes[134]. As a consequence, temporal fractionation interferes this process and it clarifies the need for a more optimal modality that can induce the therapeutic effect with reduced or no temporal fractionation.
6) Yang et al. found that MRT, through manipulating the cytokines expression in a different way compared to conventional radiotherapy, promotes the favorable immune response in tumor microenvironment[135].
7) Single high dose radiation (>10Gy) causes massive endothelial damage which impairs the T-cell recruitment in the tumor. There are various studies which have confirmed MRT normalizes the tumor microvasculature and consequently, enhances the T-cell trafficking[136].

To investigate the hypothetical effect of MRT on the immune system, I examined the tumor response to MRT and conventional irradiation in immunocompetent and immunocompromised mice.

6.2 Approach:

6.2.1 Cell Culture:

The method for cell growth can be found in section 4.2.1. See section 5.2.2 for the cell preparation and number of the cell injected per mice.

6.2.2 Mice:

Five to six-weeks-old female C57BL/6 and B6.129S7-Rag1^{tm1Mom}/J mice were obtained from Jackson Laboratory (Bar Harbor, ME) and maintained under pathogen-free condition. B6.129S7-Rag1^{tm1Mom}/J (Rag-) mice do not develop mature T-cells and B-cells, so they lack acquired immune system. All the experiments were performed according to approved protocols by UNC-CH IACUC.

6.2.3 Tumor Treatments and Reagent:

For follow-up procedures and tumor measurements see section 5.2.2. If the mice survived the first tumor challenge (no tumor growth 60 days post inoculation), they were rechallenged by injecting the same number of the cells to their left (contralateral) thigh.

Anti-mouse CD8a (BE0004-1, BioXCell, West Lebanon, NH) was injected IP on day -2, day 0, then twice per week for the duration of experiment (.2 mg per mouse)[7].

6.2.4 Irradiation and Dosimetry:

An industrial irradiator (X-RAD 320, PXi, North Branford, CT) was utilized as our radiation source. To apply MRT, I used a collimator that converts the beam of this conventional irradiator to 44 beams (beam FWHM = 246±32μm; center-to-center = 926±23μm; peak-to-valley dose ratio at entrance = 24.35±2.10; collimator relative output factor = 0.84±0.04). The detailed specification of the irradiator and full dosimetric characteristics of our method for applying can be found in Chapter 3[137].

On day 8, the mice in BB and MRT groups underwent irradiation as described in section 4.2.4. Briefly, the anesthesia was induced by 3-4% isoflurane and maintained by 1-2% isoflurane in medical-grade oxygen at 0.8-1 L min^{-1} flow rate. Except for the irradiation field, the whole the animal body was shielded by 1 cm thick lead. The anesthetized mouse was positioned on a dedicated mouse-holder and its head, body and right hind limb were fixed. The radiotherapy was delivered to the 1.5cm×1.5cm radiation field, centered at the site of cell inoculation. Radiation was delivered at 4.8 $cGy.sec^{-1}$ with 160 kVp X-ray. The focal-to-surface distance was 37cm. The mice in MRT received 150 Gy vs. 15Gy in BB. The logic behind our dose selections can be found in Chapter 4. Gafchromic® MD-V2 film (Ashland, Bridgewater, NJ) was placed at the entrance and exit plan to confirm the dose delivery and for dosimetry measurements. The film was scanned and analyzed using the protocol described in Chapter 3.

6.2.5 Immunostaining of Tumor Sections:

Two days and one week after MRT, BB and mock treatment the mice were humanely sacrificed and the tumors were harvests for histology analyzes. The tumors were stained for

THs, CTLs and Tregs. Extracted tissues were fixed in formalin for 48h, processed, embedded in paraffin and serially sectioned at 5µm thickness.

Immunohistochemical analysis for Mouse CD4 (14-9766, eBioscience) was performed on paraffin slide specimens. Antigen retrieval was performed using Ventana's CC1 (pH 8.5), for 72 min at 100°C, followed by the primary antibody diluent (1:25) for 4 hr at room temperature using Discovery Ab Diluent, 760-108. The slides were then given a post-primary peroxidase incubation for 8 min, followed by the secondary antibody (Ventana Omap OmniMap anti-Rat HRP, 760-4457, Ready to Use) for 32 min at room temperature. The slides were incubated in Discovery Purple, 760-229 for 1 hr and 32 min.

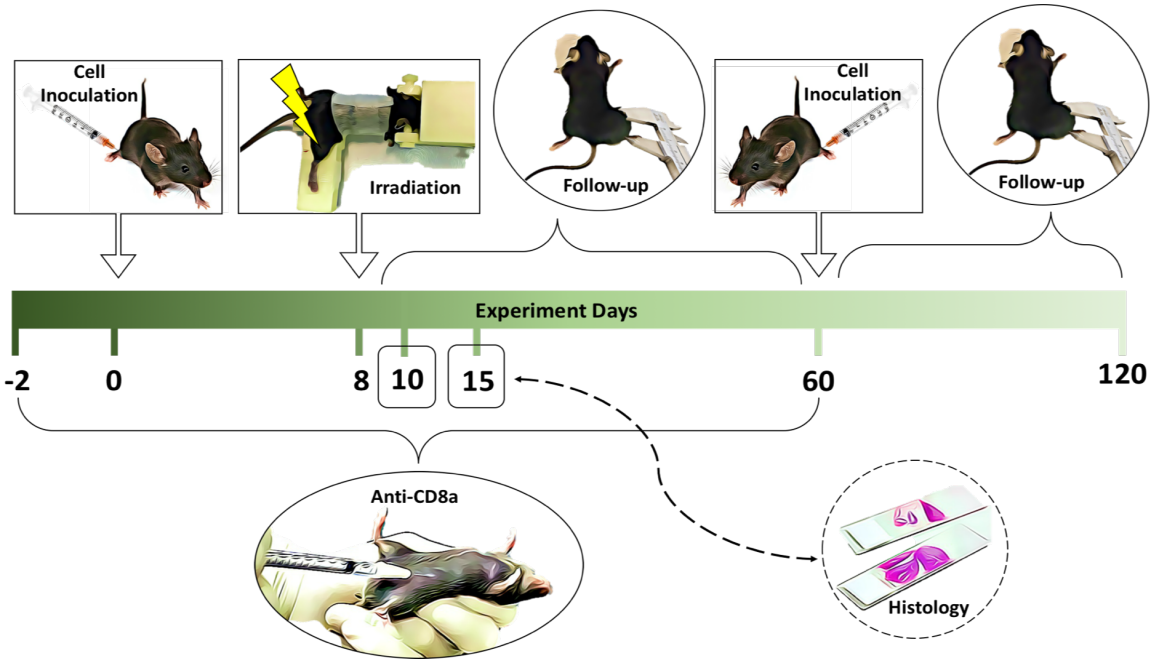

Figure 6-7: Tumor model and experiment schedule. Immunocompetent or Rag1K0 mice were injected s.c. with syngeneic B16-F10 cells (8×10^4) into the right thigh on day 0. On day 8, irradiation, either as MRT or BB, was given in a single dose locally, exclusively to the tumor inoculation site with the rest of the body shielded. Mouse anti-CD8a was given i.p on day -2, 0 and then twice a week as indicated. Tumor dimensions were measured until the tumor volume reached 1.5 cm^3 or day 60. The mice survived the primary challenge, were re-challenged by injecting the same number of the B16-F10 cells s.c. to the left thigh on day 60 and followed-up for the next 60 days. For histology studies, tumors were harvest 2 and 7 days after irradiation.

Immunohistochemical analysis for anti-Mouse CD8a (14-0808, eBioscience) was performed on paraffin slide specimens. Antigen retrieval was performed using Ventana's CC1 (pH 8.5), for 64 min at 100°C and given a peroxidase step for 8 min, followed by the primary antibody diluent (1:100) for 2 hr at room temperature using Discovery PSS Diluent, 760-212, and then the secondary antibody (Ventana Omap OmniMap anti Rat HRP, 760-4457, Ready to Use) for 32 min at room temperature. The slides were incubated in Discovery Purple, 760-229 for 32 min.

Immunohistochemical analysis for FoxP3 (14-5773, eBioscience) was performed on paraffin slide specimens. Antigen retrieval was performed using Ventana's CC1 (pH 8.5), for 64 min at 100° C, given a protein block for 1 hr, followed by a peroxidase incubation for 8 min. The primary antibody diluent (1:25) was added and incubated for 2 hr at room temperature using Discovery Ab Diluent, 760-108. The slides were then treated with the secondary antibody (Ventana Omap OmniMap anti-Rat HRP, 760-4457, Ready to Use) for 32 min at room temperature. The slides were incubated in Discovery Purple, 760-229 for 1 hr and 4 min.

Stained slides were digitally imaged at ×20 magnification using the Aperio ScanScope XT (Aperio Technologies, Vista, CA). Digital images were stored in the Aperio Spectrum eSlide Database. Cells were analyzed for CD8 and FoxP3 using the Aperio Cytoplasmic V2 algorithm with adjustments for stain optical densities to ensure removal of melanin from the analysis. Default thresholds for 0, 1+, 2+, and 3+ staining intensities were used. To increase the specificity and reduce the background noises, only the cells that were stained ≥ 2+ were considered positive.

6.2.6 Statistical Analysis:

For all analysis, a p-value < .05 was considered statistically significant. The sample size power was evaluated using PROC POWER, SAS version 9.4 (SAS Institute Inc., Cary, NC). Statistical analysis was performed by SPSS version 22 (IBM, Armonk, NY). Differences in survival were determined for each group using the Kaplan-Meier method and the p-value was calculated by the log-rank test. The one-way analysis of variance (ANOVA) determined whether there were any significant differences between the mean tumor volume at different time points.

6.3 Result:

6.3.1 Intact acquired immune system is required for treatment response to MRT:

The normal C57BL/6 and Rag1K0 mice were injected on right leg with the same number of cells on day 0 and received BB, MRT or mock irradiation on day 8. The mice were weighted and the tumor dimension was measured three-times a week. When the tumor volume reached 1.5 cm^3, the mice were humanely sacrificed to reduce the mortality. The overall survival of the mice was compared among the various group as demonstrated in Fig 6-8. Although in normal mice MRT significantly hinders the tumor growth vs. conventional radiation ($p<.001$), in Rag1K0 mice MRT was not an effective modality for controlling the tumor growth as compared to BB ($p=.78$).

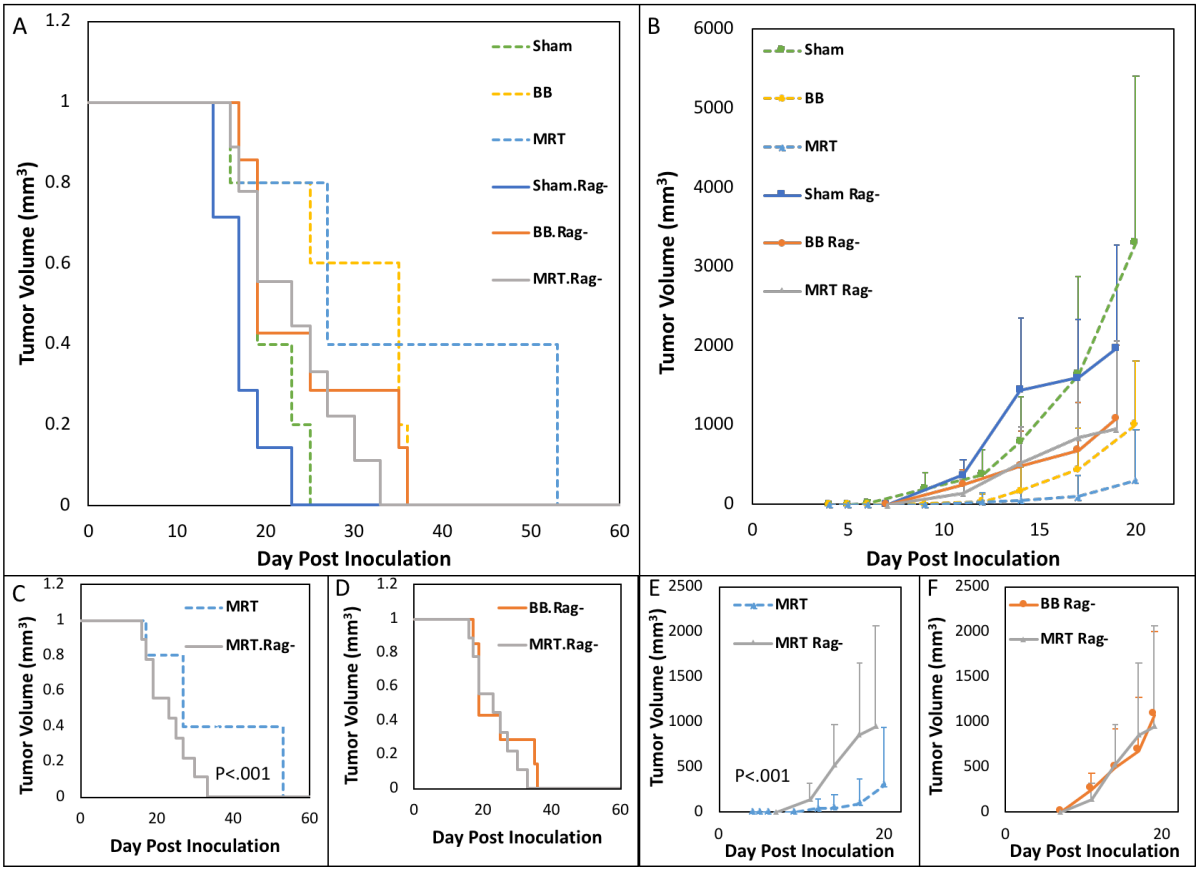

Figure 6-8: The Kaplan-Meier curves (A,C,D) demonstrate the proportion of the mice survived in various treatment groups at different time points after cell inoculation (Day 0); C) The treatment effect of the MRT was suppressed in the Rag- mice that lack acquired immune system (p<.001); D) MRT did not induce a significant difference in the overall survival of the Rag- mice compared to the BB; B, E and F demonstrate the tumor volume at different time points after cell injection; E) The suppressive effect of MRT on tumor growth was diminished in the Rag- mice (p<.001); F) MRT did not significantly hinder the tumor growth in Rag- mice vs. conventional irradiation.

6.3.2 MRT induces more robust cytotoxic lymphocyte recruitment:

The tumors were harvested 48 hours after irradiation and stained for F4/80 to detect macrophages and a week after irradiation in immunocompetent mice and stained for CD4, CD8a and FoxP3 to detect the B-cells, THs, CTLs and Tregs (See Fig 6-9). Interestingly, at these time points, the number of B-cells and CTLs were significantly higher in MRT-treated tumor compared to BB and Sham. In addition, the number of Tregs in MRT were significantly

lower than BB group. When compared to sham and BB, MRT did not increase the number of CD4, one week after irradiation (data not shown).

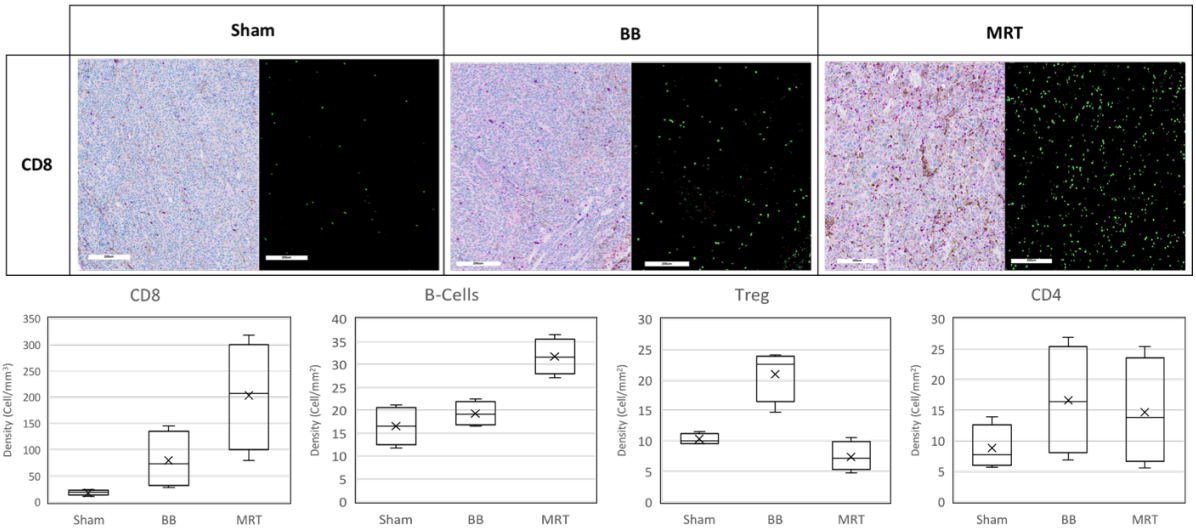

Figure 6-9: Top) The histological section of mouse melanoma one week after, mock irradiation (Sham), conventional irradiation (BB) or microbeam radiation therapy (MRT), stained for mouse CD8a. It demonstrates the higher number of CTLs infiltration in MRT group. The bars are 0.2mm. The graphs demonstrate the median number of CTLs B-cells, Tregs and THs in three different study groups. MRT significantly increased the number of CTLs and B-cells infiltrations into the tumor one week after irradiation. The number of Tregs was significantly suppressed after MRT. The number of THs was statistically the same in treatment groups.

6.3.3 Cytotoxic T-cells play a crucial role in tumor response after MRT:

The normal C57BL/6 mice were injected on right leg with 8×10^4 of cells on day 0 and received BB, MRT or mock irradiation on day 8. The anti-mouse CD8a were injected i.p. on day -2, day 0 and then twice a week. Interestingly, neither BB nor MRT was effective in treating the tumor or suppressing the tumor growth in these mice, compared to sham (Fig 6-10).

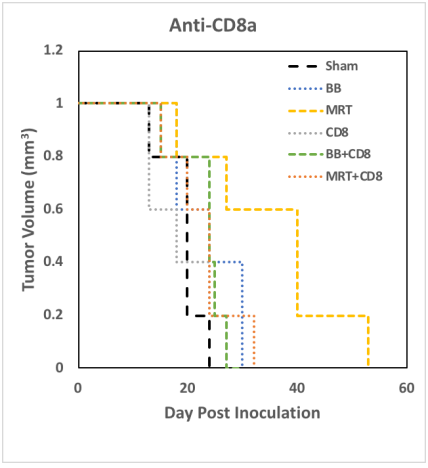

Figure 6-10: Kaplan-Meier curve demonstrates the survival of sham and CD8 depleted mice after different treatment.

6.3.4 MRT alone does not elicit persistent anti-tumor response:

One mouse in MRT group survived the first tumor injection challenge. The left leg of the mouse was injected with B16-F10. It was hypothesized that MRT induces the systemic anti-tumor response. The tumor started to grow in this mouse and the hypothesis was rejected (Fig 6-11).

6.4 Discussion:

The effect of irradiation on the tumor immune response has recently been the subject of great interest. Most of the immune-stimulating effects of irradiation have been proven to be dose-dependent, i.e. the higher the radiation dose the higher the anti-tumor immune response will be[117]. Since the high dose is beyond the normal tissue tolerance, a number of groups have suggested that the use of hypofractionation low dose irradiation is the optimal modality [138]. However, it seems that fractionation of radiotherapy interferes with the APC function[134].

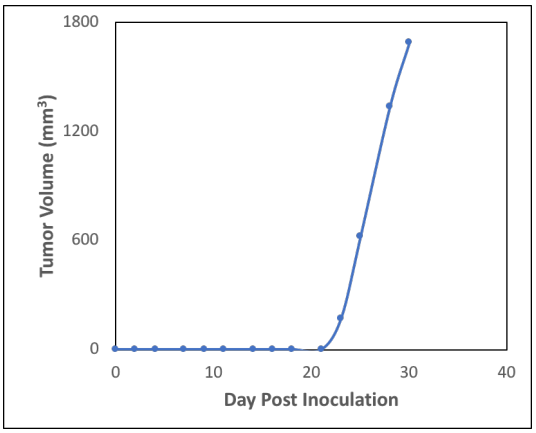

Figure 6-11: Left leg tumor volume in the re-challenged mouse. MRT did not induce long term memory in this mouse.

The treatment doses utilized in MRT greatly exceed the conventional radiation limits. Despite these high doses, the detrimental effects of MRT on normal tissue are minimal[30]. Furthermore, during MRT most of the tumor volume lies in the valet area. Therefore, a confirmed regional bystander effect could explain how tumor eradication occurs in the regions of tumors that receive irradiation doses equal or lower than standard irradiation dose[139].

The loss of the microbeam treatment effect in the Rag1K0 mice suggests the importance of the acquired immune system to the MRT effect, supporting its immune-mediated effect. Furthermore, the loss of the microbeam advantage in survival with the elimination of CD-8 cells further reinforces the importance of the adaptive immunity in the microbeam advantage. However, MRT alone was not able to induce a systemic anti-tumor response. This may be in part due to the limited activation of CD4 lymphocytes after MRT and insufficient formation of memory cells. It also should be mentioned that the anti-tumor memory was only evaluated in one mouse that survived after MRT. Thus, future research should focus on defining optimal radiotherapy protocols on one hand and optimal, tumor-specific immune therapeutic approaches on the other hand that can achieve the highest level of synergy.

CHAPTER 7 LIMITATIONS, FUTURE DIRECTION AND CONTRIBUTION

7.1 Limitations and future researches:

In the neurocognitive study, the total number of mice was limited (n=24 in the test), but by running pretest (n=9 in pretest), and use of different tests on separate days, I increased the sensitivity of the study to detect subtle differences. On 8th-month post-irradiation, the mice were evaluated using Barnes Maze test, which has been found to be the most sensitive test for detection of irradiation-induced hippocampal-dependent cognitive changes in rodent[69]. Another limitation was the use of normal mice. Patients with brain tumors often experience cognitive dysfunction associated with the disease that is present at diagnosis[140,141]. As a result, tumor regression will substantially improve the neuropsychological function level[142]. In the current study, the effect of two different methods of radiotherapy on normal healthy mouse brain was compared. Having said that, a recent study has shown that brain tumor patients are more prone to post-irradiation cognitive deterioration than normal patients[143]. Consequently, the optimal study would be the one that compares the neurocognitive performance of BB- and MRT-treated brain tumor mice. However, considering the aggressive nature of mice brain tumor models, such a study is not feasible for a long-time follow-up.

Another limitation was using radiochromic film for dosimetry. Although these films have been used extensively in MRT studies[39,40,42], currently the level of uncertainty of film

dosimetry has been reported between 1% and 10% depending on the situation[144–147]. Here I followed the single scan, three-channel protocol, recommended by the supplier to minimize errors[90]. However, this protocol does not eliminate some reported source of errors, like film curvature at scanning[147].

I cross-calibrated the mounted transmission chamber to an ion chamber and used the transmission plate for dose measurements. This also introduced some potential errors (1.25±.08 percentage difference between the two methods). To minimize this error, the calibration was done at a high dose (150 Gy) and checked twice.

Finally, some errors were introduced from utilizing the plastic phantom (PMMA or acrylic) instead of water. Although the IAEA TRS398 code of practice approved their application for low energy X-ray dosimetry, the plastic phantom introduces error in measurements mainly due to density variation (up to 4%) in different batches, and non-homogenous thickness distribution even in one sheet[148]. The density of the sheet used was 1.174 g cm^{-3} and I measured the entire slab and used the piece that was 2 ±0.01 mm thick.

The translation of my method for applying MRT to clinics may encounter several technical limitations. The low dose rate and limited heat conduction capacity of clinical irradiators are the major limitations of the current method, and, consequently, developing a high-intensity kilovoltage irradiator would be advantageous. Second, with proximal collimating, aligning the collimator with the source may require a greater deal of accuracy. Designing a device to mount the collimator may ease this problem. An applicator may also be needed to restrict the radiation field to the lesion. Although normal skin demonstrated a higher resistance to MRT in the acute phase, confining the radiation field to the lesion is always desired in order to minimize the normal tissue toxicity. Besides, utilizing an image-guided modality would further limit the

radiating the normal tissue. Finally, beam smearing due to the long duration of therapy also remains a significant consideration, as even cerebral spinal fluid fluctuations can induce millimeter scale movements[149]. Aside from high-intensity irradiator, applying irradiation by a physiologically gated irradiator may help to overcome this problem[33].

Aside technical complication, further radiobiological and preclinical studies are necessary to guide this modality to its appropriate clinical translation. Although in small animal studies it is not a major obstacle, when the target is a deep-sited tumor, like brain tumors, in larger animals or humans, higher doses may be required due to the steep dose drop in orthovoltage beams. As a result, high dose of irradiation deposits to the tissues proximal to the tumor, mainly skin, and may cause severe injuries in these tissues. The technical solution to this problem is to apply MRT from various directions and implement what is referred as "cross-beams" (Fig7-1)[99]. Preclinical studies using synchrotron sources demonstrated this method is superior to unidirectional MRT in treating animal models of cancers and has been used for radiosurgeries[150]. However, since at the cross-fire zone the classical MRT-pattern of peak and valley is impaired, high toxicity of the normal tissue has been observed, so the overlapping

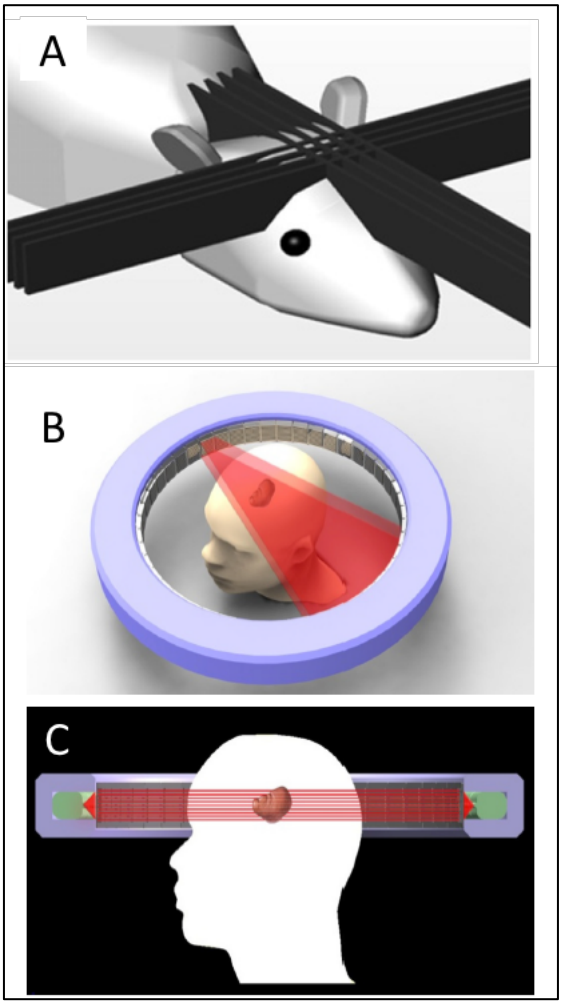

Figure 7-1: A) The cross-beam pattern as used at synchrotron labs. B,C) Hypothetical crossbeam application with the ring irradiator for irradiating deep sited brain tumor.

zone should be precisely limited to the actual tumor area[151,152]. Applying MRT on larger animal models would provide valuable information regarding the normal tissue effect of this modality. At the current stage, using the cabinet irradiator, it is possible to treat small pets namely cats, rabbits, piglets and small dogs.

Here, all of the *in vivo* studies were on a murine model of melanoma (B16-F10). This cell line has been well studied[110]. It is proven to be radioresistant and have low immunogenicity[111,153]. Furthermore, melanoma is a superficial tumor, which simplified the radiation targeting and tumor follow-up. Altogether, these properties made this cell line an appropriate choice for my purposes. In future, other cell lines and another cancer models should be used. Considering the normal tissue sparing effect of MRT, tumors embedded in the radiosensitive tissues, like the brain, would be of great interest.

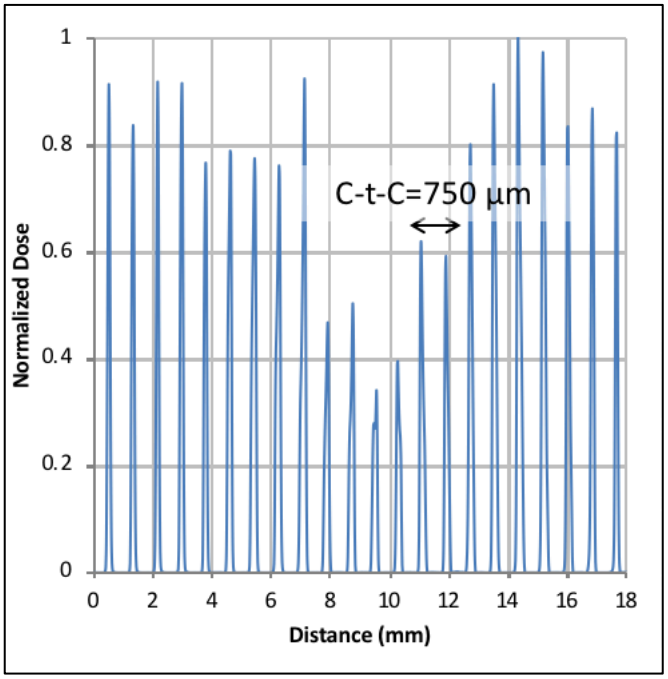

Figure 7-2: The beam pattern of a prototype collimator with 150 µm beam FWHM and center to center distance of 750 µm. The collimator was made to be used under the industrial irradiator.

Another helpful biological investigation would be evaluating the tumor immune infiltration at different time points using the gold standard flow cytometry. The cells of interest would be APCs especially dendritic cells. Unfortunately, to the best of my knowledge, currently, there is no effective stain for mouse dendritic cells, for histological studies. Here, I evaluated the tumors 48h and a week after irradiation for CTLs, Tregs, THs, and macrophages.

I found that the number of CTLs and Treg were significantly different between BB and MRT, but no difference was detected between the number of CD4 infiltrated in tumor 48h after irradiation between these two modalities. In addition, ablating the CD8 cells diminished the effect of MRT. Besides, no memory against tumor cells was detected in the survived mouse. These observations support the idea that MRT activates CTLs but is not an efficient CD4 activator. As a result, more studies on the pathways that activate CTLs alone, like the increase in the MHC-I expression on cancer cells, would be of great interest. Furthermore, to boost-up the immune effect of MRT, combination MRT and immunotherapy, would be the next logic step.

Finally, the physical dimensions I employed for the collimator construction was based on the previous studies in our group. Studies at synchrotrons have demonstrated that different beam dimension may elicit a different response in tumor and normal tissue. Consequently, it would be interesting to evaluate different beam width and center-to-center distance to find the optimal collimator configuration. Using the same method in section 3.2.2, I have demonstrated the feasibility of making a collimator with 150 μm beam, 750 μm center-to-center distance.

7.2 Contribution to science:

My preclinical research on the application of microbeam radiotherapy (MRT) has added fundamental concepts to the body of knowledge. The neurocognitive study was the first in the field that utilized comprehensive behavioral evaluations to investigate the effect of MRT on normal brain tissue for long duration of time. Here I presented the first collimator-based approach to apply MRT on small animal. The application of other collimator is limited to physical and cellular studies and just recently a group has generated a collimator to be used in

animal studies[109]. To the best of my knowledge, my developed collimator generates the most uniform and the largest microbeam irradiation field using the industrial orthovoltage irradiator. I was the first in the field that measured the *in-vitro* and *in-vivo* radiobiological equivalent dose using this approach. The first treatment efficacy of collimator generated MRT *in-vivo* was evaluated and presented here. We were the first group that evaluated the role of acquired immune system in treatment efficacy of MRT. The main body of my work has been published in two manuscripts and I have presented it in different international meetings:

1. S. Bazyar, et al. "Minibeam Radiotherapy with Small Animal Irradiators; In-vitro and In-vivo Feasibility Studies". Physics in Medicine and Biology. 2017, 62(23):8924-42.

2. S. Bazyar, et al. "Neurocognitive Sparing Desktop Microbeam Irradiation". Radiation Oncology, 2017;12(1)127.

3. S. Bazyar, et al. "Efficacy of Combined Microbeam Radiotherapy and Immunotherapy on Melanoma". 2nd Annual International Conference on Immunotherapy Radiotherapy Combinations, September 2017, New York, NY.

4. S. Bazyar, et al. "Minibeam Radiotherapy with Conventional Irradiators". Immunoradiotherapy Workshop, June 2017, NIH Campus, Bethesda, MD.

5. S. Bazyar, et al. "Proximal Collimation to Apply Non-synchrotron Microbeam Radiotherapy". American Physician Scientists Association, April 2017, Chicago, IL.

6. S. Bazyar, et al. "Neurocognitive Sparing Desktop Microbeam Irradiation". Radiation Research Society Annual Meeting, October 2016, Waikoloa, HI.

In addition, during my PhD eduation, I was honored to receive the following awards:

1. 1st Best Clinical Poster Award, Lineberger Comprehensive Cancer Center; 2017.

2. Dissertation Completion Fellowship Award; Full-Scholarship (Stipend+Tuition+Fees) for the last year of Ph.D., University of North Carolina at Chapel Hill; 2017.

3. Travel Award, $1000 to be used for travel to an international academic conference or professional society meeting to present my research, University of North Carolina at Chapel Hill; 2016.

4. 3rd Best Translational Poster Award; Lineberger Comprehensive Cancer Center; 2016.

My ongoing research is on the effect of combined MRT and immune checkpoint blockers, that I will present some of the preliminary data in the next chapter.

APPENDIX 1. CONCURRENT MICROBEAM RADIATION THERAPY AND IMMUNE CHECKPOINT BLOCKER: INITIAL FEASIBILITY STUDIES

A1.1. Rationale:

In the latest years, the development of immune checkpoint inhibitors represents the main step forward in the treatment of cancers. Even though they demonstrated superiority towards standard available treatments in different disease settings, the response rates are still low (Fig. 8-1[154]). For instance, after combined PD-1 and anti-CTLA-4 treatment, the two main FDA approved checkpoint blockers, the progression-free survival of the patient with non-small cell lung cancer was almost 30% after one year[155]. Furthermore, the response rate of highly molecularly selected patients with same cancer (expressing PD-L1 in at least 50% of tumor cells) to PD-1 inhibitor did not exceed 45%[156]. Additionally, combined immune checkpoint blockers (anti-CTLA-4 and PD-1 inhibitor) can cause severe toxicities in patients (Table 8-1). As a result, a more robust combination therapy with less severe side effects is needed.

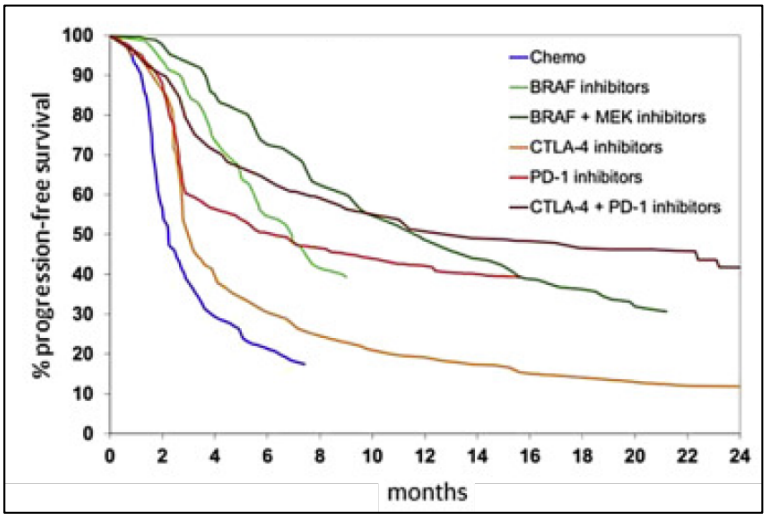

Figure A1-1: Mean survival curves created by weighted averaging of Kaplan–Meier survival curves of melanoma patients treated in different clinical trials[151].

Table A1-1: Efficacy and safety results from a phase III trial of anti-PD1 alone or combined with anti-CTLA-4 versus anti-CTLA-4 alone in treatment-naive patients with advanced melanoma[157]

	Anti-PD1	**Anti-CTLA-4**	**Combination**
Progression Free Rate (month)	6.9	2.9	11.5
High Grade Toxicity (%)	16.3	27.3	53
Drop Out Rate (%)	7.7	14.8	36.4

As mentioned previously, radiotherapy can have both proimmunogenic and immunosuppressive effects. However, a common point in these paradoxical effects seems to be that radiation most probably can only amplify or augment a pro-immunogenic microenvironment and cannot singlehandedly change a net immune suppressing environment into an immune stimulating one[158]. As a result, it has been proposed that concurrent immunotherapy and radiation therapy may have synergic effect: RT provides better cancer antigen-presenting, while checkpoint blockers alter the tumor microenvironment to more immunogenic. Multiple studies have proven this synergistic effect and demonstrated that this combination therapy has also increased the chance of radiation abscopal effect [111,138,159–163].

In chapter 6, it was shown that MRT can elicit a more robust anti-tumor immune response, but it did not develop any memory against cancer cells. Accordingly, I postulated that concurrent MRT and immune checkpoint blocker would have superior effect vs. the combination of conventional radiation therapy (BB) with the same agent.

A1.2. Approach:

A1.2.1. Cell Culture:

The method for cell growth and maintenance can be found in section 4.2.1. The method of cell preparation and number of the cell injected per mice see section 5.2.2. Only the cells within 4 passages (4 to 8) were injected to the mice.

A1.2.2. Mice:

Five to six-weeks-old female C57BL/6 mice were obtained from Jackson Laboratory (Bar Harbor, ME) and maintained under pathogen-free condition. All the experiments were performed according to approved protocols by UNC-CH IACUC.

A1.2.3. Tumor Treatments and Reagent:

For follow-up and tumor measurements see section 5.2.2. If the mice survived the first tumor challenge (no tumor growth 60 days post inoculation), they were rechallenge by injecting the same number of the cells to their left thigh.

Anti-mouse CTLA-4 (BP0131, BioXCell, West Lebanon, NH) was selected because it has proven to have no effect on B16-F10 tumor model *in vivo*[111]. The drug was given i.p. on day 5, 8 and 11 (.2mg per mouse)[111].

Anti-mouse CD8a (BE0004-1, BioXCell, West Lebanon, NH) was injected IP on day -2, day 0, then twice per week for the duration of experiment (.2 mg per mouse)[111].

A1.2.4. Irradiation and Dosimetry:

The detailed description of irradiator, dose, settings and dosimetry method cab be found in section 6.2.4.

A1.2.5. Statistical Analysis:

For all analysis, a p-value < .05 was considered statistically significant. The sample size power was evaluated using PROC POWER, SAS version 9.4 (SAS Institute Inc., Cary, NC). Statistical analysis was performed by SPSS version 22 (IBM, Armonk, NY). Differences in survival were determined for each group using the Kaplan-Meier method and the p-value was calculated by the log-rank test.

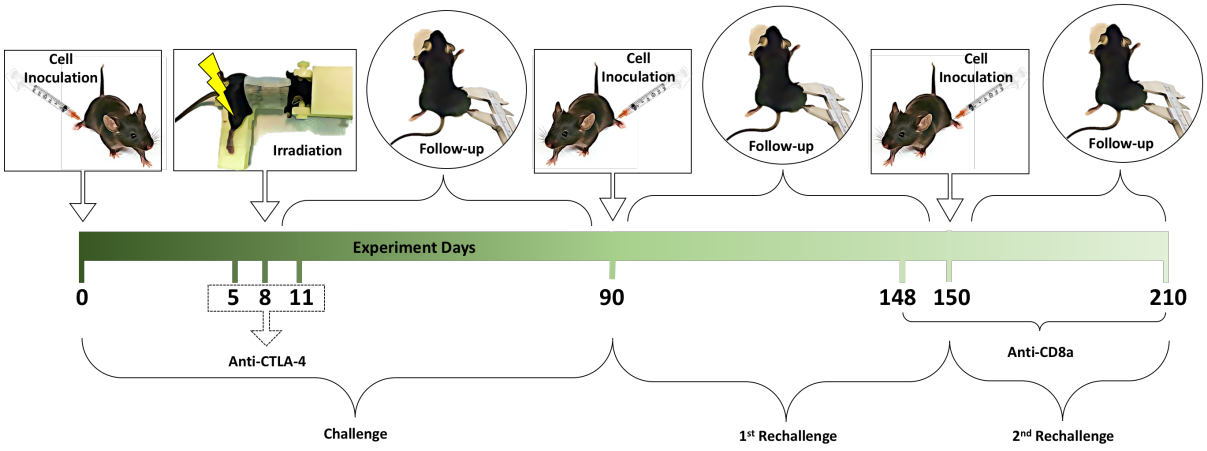

Figure A1-2: Tumor model and experiment schedule.

A1.3. Result:

A1.3.1.Microbeam radiotherapy is more effective than standard irradiation when combined with immune checkpoint blockers:

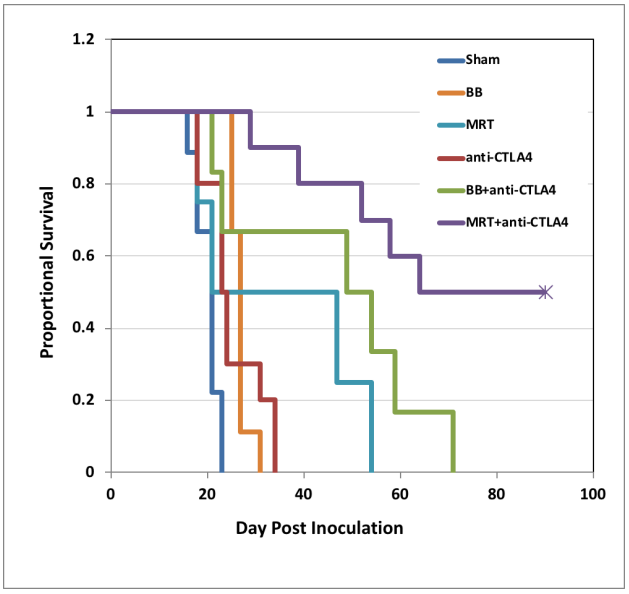

Figure A1-3: The Kaplan-Meier curve demonstrates the survival in different treatment group. Five out of ten mice that received combined MRT+anti-CTLA-4 survived up to 90 days post tumor inoculation (log rank p<.001).

The mice were inoculated with $8x10^4$, B16-F10 cell on day 0, on their right leg. The mice were randomly assigned to six different treatment groups. The anti-CTLA4 was injected i.p on day 5, 8 and 11. The mice in BB and MRT groups received treatment on day 8. Interestingly, the combined MRT and anti-CTLA-4 induced a robust synergic effect (Fig 8-3). Consequently, 5 out of 10 mice did survived up to day 90 (log rank p<.001).

A1.3.2. Combined microbeam radiotherapy and immune checkpoint blockers induces anti-tumor memory:

The tumor did not grow in five out of ten mice that received combined MRT and anti-CTLA-4, up to 90 days post inoculation. These mice were rechallenged by injecting the same cell line s.c to the left flank. The tumor didn't grow in any of these five mice up to 90 days after second tumor inoculation.

A1.3.3.The anti-tumor memory is CD8 dependent:

To investigate if this memory response is CD8 dependent, the mice that survived the first rechallenge, were injected with the same cell line, on the left leg. These mice were categorized into two groups: one group (N=3) received anti-mouse-CD8a on days -2, 0 and the twice per week (day 0 was assigned the second rechallenge cell inoculation day). The result is shown in Fig 8-4. The tumor did not grow in the mice that were not injected with the anti-CD8a reagent, while suppressing the CTLs caused the tumor to grow. As a result, the memory effect was CD8 related.

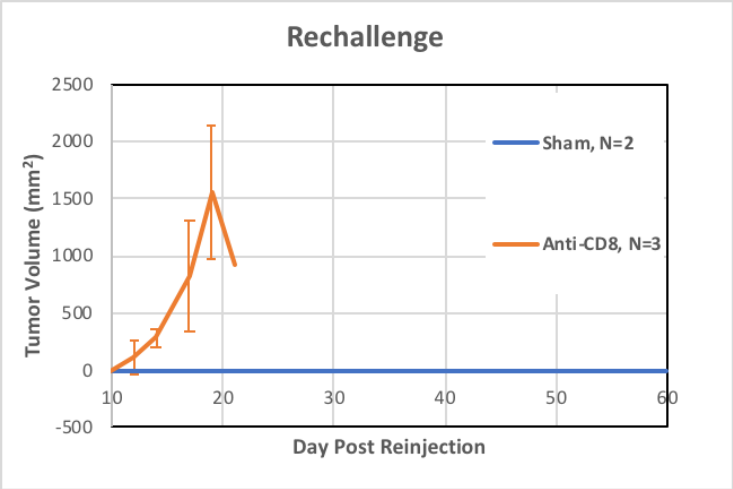

Figure A1-4: Mean tumor volume±SEM in second rechallenge test. The tumor did not grow in the immunocompetent mice.

A1.4. Discussion:

In Chapter 6, I found that acquired immune system, CTLs in particular play crucial role in the effect of MRT. The studies in this Chapter demonstrated that the combination of MRT and anti-CTLA-4 may elicit a more robust anti-tumor response and induce a long-term anti-tumor memory. Since these studies are in the preliminary stages, the main goal was to present the concept and methods. The more comprehensive results and conclusions need further studies to confirm the reproducibility of data and the underlying mechanisms.

REFERENCE

1. Cancer Facts & Figures 2018. https://www.cancer.org/content/dam/cancer-org/research/cancer-facts-and-statistics/annual-cancer-facts-and-figures/2018/cancer-facts-and-figures-2018.pdf. Accessed February 20, 2018.

2. Radiation Therapy for Cancer - National Cancer Institute. https://www.cancer.gov/about-cancer/treatment/types/radiation-therapy/radiation-fact-sheet. Accessed February 20, 2018.

3. Armoogum K, Thorp N. Dosimetric Comparison and Potential for Improved Clinical Outcomes of Paediatric CNS Patients Treated with Protons or IMRT. *Cancers (Basel)*. 2015;7(4):706-722. doi:10.3390/cancers7020706

4. Zeman W, Curtis HJ, Gebhard EL, Haymaker W. Tolerance of mouse-brain tissue to high-energy deuterons. *Science*. 1959;130(3391):1760-1761. http://www.ncbi.nlm.nih.gov/pubmed/13847257.

5. Slatkin DN, Spanne P, Dilmanian FA, Sandborg M. Microbeam radiation therapy. *Med Phys*. 1992;19(6):1395-1400. doi:10.1118/1.596771

6. Laissue JA, Geiser G, Spanne PO, et al. Neuropathology of ablation of rat gliosarcomas and contiguous brain tissues using a microplanar beam of synchrotron-wiggler-generated X rays. *Int J Cancer*. 1998;78(5):654–660. doi:10.1002/(SICI)1097-0215(19981123)78:5<654::AID-IJC21>3.0.CO;2-L

7. Dilmanian FA, Morris GM, Zhong N, et al. Murine EMT-6 Carcinoma: High Therapeutic Efficacy of Microbeam Radiation Therapy. *Radiat Res*. 2003;159(5):632-641. doi:10.1667/0033-7587(2003)159[0632:MECHTE]2.0.CO;2

8. Miura M, Blattmann H, Bräuer-Krisch E, et al. Radiosurgical palliation of aggressive murine SCCVII squamous cell carcinomas using synchrotron-generated X-ray microbeams. *Br J Radiol*. 2006;79(937):71-75. doi:10.1259/bjr/50464795

9. Zhong N, Morris GM, Bacarian T, Rosen EM, Dilmanian FA. Response of rat skin to high-dose unidirectional x-ray microbeams: a histological study. *Radiat Res*. 2003;160(2):133-142. http://www.ncbi.nlm.nih.gov/pubmed/12859223. Accessed February 20, 2018.

10. Dilmanian FA, Morris GM, Le Duc G, et al. Response of avian embryonic brain to spatially segmented x-ray microbeams. *Cell Mol Biol (Noisy-le-grand)*. 2001;47(3):485-493. http://www.ncbi.nlm.nih.gov/pubmed/11441956. Accessed February 20, 2018.

11. Sabatasso S, Laissue JA, Hlushchuk R, et al. Microbeam radiation-induced tissue damage depends on the stage of vascular maturation. *Int J Radiat Oncol Biol Phys*.

2011;80(5):1522-1532. doi:10.1016/j.ijrobp.2011.03.018

12. Laissue JA, Lyubimova N, Wagner H-P, et al. Microbeam radiation therapy. In: Barber HB, Roehrig H, eds. ; 1999:38. doi:10.1117/12.368185

13. Slatkin DN, Spanne P, Dilmanian FA, Gebbers JO, Laissue JA. Subacute neuropathological effects of microplanar beams of x-rays from a synchrotron wiggler. *Proc Natl Acad Sci*. 1995;92(19):8783-8787. http://www.pnas.org/content/92/19/8783. Accessed January 3, 2014.

14. Serduc R, Vérant P, Vial J-C, et al. In vivo two-photon microscopy study of short-term effects of microbeam irradiation on normal mouse brain microvasculature. *Int J Radiat Oncol*. 2006;64(5):1519-1527. doi:16/j.ijrobp.2005.11.047

15. Serduc R, Looij Y van de, Francony G, et al. Characterization and quantification of cerebral edema induced by synchrotron x-ray microbeam radiation therapy. *Phys Med Biol*. 2008;53(5):1153. doi:10.1088/0031-9155/53/5/001

16. Laissue JA, Blattmann H, Wagner HP, Grotzer MA, Slatkin DN. Prospects for microbeam radiation therapy of brain tumours in children to reduce neurological sequelae. *Dev Med Child Neurol*. 2007;49(8):577-581. doi:10.1111/j.1469-8749.2007.00577.x

17. Laissue JA, Blattmann H, Wagner HP, Grotzer MA, Slatkin DN. Prospects for microbeam radiation therapy of brain tumours in children to reduce neurological sequelae. *Dev Med Child Neurol*. 2007;49(8):577-581. doi:10.1111/j.1469-8749.2007.00577.x

18. Laissue JA, Blattmann H, Di Michiel M, et al. Weanling piglet cerebellum: a surrogate for tolerance to MRT (microbeam radiation therapy) in pediatric neuro-oncology. In: Barber HB, Roehrig H, Doty FP, Schirato RC, Morton EJ, eds. Vol 4508. International Society for Optics and Photonics; 2001:65-73. doi:10.1117/12.450774

19. Thomlinson W, Chapman D, Gmür N, Lazarz N. The superconducting wiggler beamport at the National Synchrotron Light Source. *Nucl Instruments Methods Phys Res Sect A Accel Spectrometers, Detect Assoc Equip*. 1988;266(1-3):226-233. doi:10.1016/0168-9002(88)90389-0

20. Decker G. The superconducting wiggler at the NSLS: Systems description and initial experience. *Nucl Instruments Methods Phys Res Sect A Accel Spectrometers, Detect Assoc Equip*. 1990;291(1-2):357-362. doi:10.1016/0168-9002(90)90087-M

21. Felici M De, Felici R, Rio MS del, Ferrero C, Bacarian T, Dilmanian FA. Dose distribution from x-ray microbeam arrays applied to radiation therapy: An EGS4 Monte Carlo study. *Med Phys*. 2005;32(8):2455-2463. doi:10.1118/1.1951043

22. Hausermann D. Accelerator based technology for cancer treatment with intense micro-beams of synchrotron radiation Daniel Häusermann Imaging and Medical Beamline. -

ppt download. http://slideplayer.com/slide/10302049/. Accessed March 7, 2018.

23. Langley RR, Fidler IJ. The Biology of Brain Metastasis. *Clin Chem*. 2013;59(1):180-189. doi:10.1373/clinchem.2012.193342

24. Walbert T, Gilbert MR. The role of chemotherapy in the treatment of patients with brain metastases from solid tumors. *Int J Clin Oncol*. 2009;14(4):299-306. doi:10.1007/s10147-009-0916-1

25. Yang Z, Bai S, Gu B, Peng S, Liao W, Liu J. Radiation-Induced Brain Injury After Radiotherapy for Brain Tumor. In: *Molecular Considerations and Evolving Surgical Management Issues in the Treatment of Patients with a Brain Tumor*. InTech; 2015. doi:10.5772/59045

26. de Guzman AE, Gazdzinski LM, Alsop RJ, et al. Treatment Age, Dose and Sex Determine Neuroanatomical Outcome in Irradiated Juvenile Mice. *Radiat Res*. 2015;183(5):541-549. doi:10.1667/RR13854.1

27. Serduc R, Looij Y van de, Francony G, et al. Characterization and quantification of cerebral edema induced by synchrotron x-ray microbeam radiation therapy. *Phys Med Biol*. 2008;53(5):1153. doi:10.1088/0031-9155/53/5/001

28. Bouchet A, Lemasson B, Le Duc G, et al. Preferential Effect of Synchrotron Microbeam Radiation Therapy on Intracerebral 9L Gliosarcoma Vascular Networks. *Int J Radiat Oncol*. 2010;78(5):1503-1512. doi:10.1016/j.ijrobp.2010.06.021

29. Bouchet A, Lemasson B, Christen T, et al. Synchrotron microbeam radiation therapy induces hypoxia in intracerebral gliosarcoma but not in the normal brain. *Radiother Oncol*. 2013;108(1):143-148. doi:10.1016/j.radonc.2013.05.013

30. Smyth LML, Senthi S, Crosbie JC, Rogers PAW. The normal tissue effects of microbeam radiotherapy: What do we know, and what do we need to know to plan a human clinical trial? *Int J Radiat Biol*. 2016;92(6):302-311. doi:10.3109/09553002.2016.1154217

31. Brown WR, Blair RM, Moody DM, et al. Capillary loss precedes the cognitive impairment induced by fractionated whole-brain irradiation: A potential rat model of vascular dementia. *J Neurol Sci*. 2007;257(1-2):67-71. doi:10.1016/J.JNS.2007.01.014

32. Hadsell M, Zhang J, Laganis P, et al. A first generation compact microbeam radiation therapy system based on carbon nanotube X-ray technology. *Appl Phys Lett*. 2013;103(18):183505. doi:10.1063/1.4826587

33. Chtcheprov P, Burk L, Yuan H, et al. Physiologically gated microbeam radiation using a field emission x-ray source array. *Med Phys*. 2014;41(8Part1):81705. doi:10.1118/1.4886015

34. Yuan H, Zhang L, Frank JE, et al. Treating Brain Tumor with Microbeam Radiation

Generated by a Compact Carbon-Nanotube-Based Irradiator: Initial Radiation Efficacy Study. *Radiat Res*. 2015;184(3):322-333. doi:10.1667/RR13919.1

35. Zhang L, Yuan H, Inscoe C, et al. Nanotube x-ray for cancer therapy: a compact microbeam radiation therapy system for brain tumor treatment. *Expert Rev Anticancer Ther*. 2014;14(12):1411-1418. doi:10.1586/14737140.2014.978293

36. Stratmann G, Sall JW, May LD V, Loepke AW, Lee MT. Beyond anesthetic properties: the effects of isoflurane on brain cell death, neurogenesis, and long-term neurocognitive function. *Anesth Analg*. 2010;110(2):431-437. doi:10.1213/ANE.0b013e3181af8015

37. Loepke AW, Istaphanous GK, McAuliffe JJ, et al. The Effects of Neonatal Isoflurane Exposure in Mice on Brain Cell Viability, Adult Behavior, Learning, and Memory. *Anesth Analg*. 2009;108(1):90-104. doi:10.1213/ane.0b013e31818cdb29

38. GAFCHROMIC ™ DOSIMETRY MEDIA, TYPE EBT-3. http://www.gafchromic.com/documents/EBT3_Specifications.pdf. Accessed February 21, 2018.

39. Crosbie JC, Svalbe I, Midgley SM, Yagi N, Rogers PAW, Lewis RA. A method of dosimetry for synchrotron microbeam radiation therapy using radiochromic films of different sensitivity. *Phys Med Biol*. 2008;53(23):6861-6877. doi:10.1088/0031-9155/53/23/014

40. Hong Z, Zenkoh J, Le B, et al. Generation of low-flux X-ray micro-planar beams and their biological effect on a murine subcutaneous tumor model. *J Radiat Res*. 2015;56(5):768-776. doi:10.1093/jrr/rrv037

41. Zhang L, Yuan H, Burk LM, et al. Image-guided microbeam irradiation to brain tumour bearing mice using a carbon nanotube x-ray source array. *Phys Med Biol*. 2014;59(5):1283-1303. doi:10.1088/0031-9155/59/5/1283

42. Hadsell MJ. THE DEVELOPMENT AND CHARACTERIZATION OF A FIRST GENERATION CARBON NANOTUBE X-RAY BASED MICROBEAM RADIATION THERAPY SYSTEM. 2013. https://cdr.lib.unc.edu/indexablecontent/uuid:0a98fb59-a755-4f96-b436-278576467d6c. Accessed February 21, 2018.

43. Casanova Borca V, Pasquino M, Russo G, et al. Dosimetric characterization and use of GAFCHROMIC EBT3 film for IMRT dose verification. *J Appl Clin Med Phys*. 2013;14(2):4111. http://www.ncbi.nlm.nih.gov/pubmed/23470940. Accessed February 21, 2018.

44. Pérez-Escudero A, Vicente-Page J, Hinz RC, Arganda S, de Polavieja GG. idTracker: tracking individuals in a group by automatic identification of unmarked animals. *Nat Methods*. 2014;11(7):743-748. doi:10.1038/nmeth.2994

45. Bailey KR, Pavlova MN, Rohde AD, Hohmann JG, Crawley JN. Galanin receptor

subtype 2 (GalR2) null mutant mice display an anxiogenic-like phenotype specific to the elevated plus-maze. *Pharmacol Biochem Behav*. 2007;86(1):8-20. doi:10.1016/j.pbb.2006.11.024

46. Bailey KR, Crawley JN. *Anxiety-Related Behaviors in Mice*. CRC Press/Taylor & Francis; 2009. http://www.ncbi.nlm.nih.gov/pubmed/21204329. Accessed February 21, 2018.

47. Alves R, Carvalho JGB de, Venditti MAC. High- and Low-Rearing Rats Differ in the Brain Excitability Controlled by the Allosteric Benzodiazepine Site in the GABA_A Receptor. *J Behav Brain Sci*. 2012;2(3):315-325. doi:10.4236/jbbs.2012.23036

48. Deacon RMJ, Rawlins JNP. Hippocampal lesions, species-typical behaviours and anxiety in mice. *Behav Brain Res*. 2005;156(2):241-249. doi:10.1016/j.bbr.2004.05.027

49. Sunyer B, Patil S, Höger H, Luber G. Barnes maze, a useful task to assess spatial reference memory in the mice. *Protoc Exch*. October 2007. doi:10.1038/nprot.2007.390

50. Meyers CA, Brown PD. Role and Relevance of Neurocognitive Assessment in Clinical Trials of Patients With CNS Tumors. *J Clin Oncol*. 2006;24(8):1305-1309. doi:10.1200/JCO.2005.04.6086

51. Giovagnoli AR, Boiardi A. Cognitive impairment and quality of life in long-term survivors of malignant brain tumors. *Ital J Neurol Sci*. 1994;15(9):481-488. http://www.ncbi.nlm.nih.gov/pubmed/7721551. Accessed February 21, 2018.

52. Crossen JR, Garwood D, Glatstein E, Neuwelt EA. Neurobehavioral sequelae of cranial irradiation in adults: a review of radiation-induced encephalopathy. *J Clin Oncol*. 1994;12(3):627-642. doi:10.1200/JCO.1994.12.3.627

53. Johannesen TB, Lien HH, Hole KH, Lote K. Radiological and clinical assessment of long-term brain tumour survivors after radiotherapy. *Radiother Oncol*. 2003;69(2):169-176. http://www.ncbi.nlm.nih.gov/pubmed/14643954. Accessed February 21, 2018.

54. Manda K, Ueno M, Anzai K. Cranial irradiation-induced inhibition of neurogenesis in hippocampal dentate gyrus of adult mice: attenuation by melatonin pretreatment. *J Pineal Res*. 2009;46(1):71-78. doi:10.1111/j.1600-079X.2008.00632.x

55. Gondi V, Tomé WA, Mehta MP. Why avoid the hippocampus? A comprehensive review. *Radiother Oncol*. 2010;97(3):370-376. doi:10.1016/j.radonc.2010.09.013

56. Wu K-L, Tu B, Li Y-Q, Wong CS. Role of Intercellular Adhesion Molecule-1 in Radiation-Induced Brain Injury. *Int J Radiat Oncol*. 2010;76(1):220-228. doi:10.1016/j.ijrobp.2009.08.017

57. Dilmanian FA, Qu Y, Feinendegen LE, et al. Tissue-sparing effect of x-ray microplanar beams particularly in the CNS: Is a bystander effect involved? *Exp Hematol*. 2007;35(4,

Supplement):69-77. doi:10.1016/j.exphem.2007.01.014

58. Bouchet A, Serduc R, Laissue JA, Djonov V. Effects of microbeam radiation therapy on normal and tumoral blood vessels. *Phys Medica*. 2015;31(6):634-641. doi:10.1016/j.ejmp.2015.04.014

59. Sprung CN, Yang Y, Forrester HB, et al. Genome-Wide Transcription Responses to Synchrotron Microbeam Radiotherapy. *Radiat Res*. 2012;178(4):249-259. doi:10.1667/RR2885.1

60. Bouchet A, Bräuer-Krisch E, Prezado Y, et al. Better Efficacy of Synchrotron Spatially Microfractionated Radiation Therapy Than Uniform Radiation Therapy on Glioma. *Int J Radiat Oncol*. 2016;95(5):1485-1494. doi:10.1016/j.ijrobp.2016.03.040

61. Kinoshita K, Ishimine H, Shiraishi K, et al. Cell and Tissue Damage after Skin Exposure to Ionizing Radiation: Short- and Long-Term Effects after a Single and Fractional Doses. *Cells Tissues Organs*. 2014;200(3-4):240-252. doi:10.1159/000435809

62. Collen EB, Mayer MN. Acute effects of radiation treatment: skin reactions. *Can Vet J = La Rev Vet Can*. 2006;47(9):931-932, 934-935. http://www.ncbi.nlm.nih.gov/pubmed/17017663. Accessed February 21, 2018.

63. Snyder JS, Kee N, Wojtowicz JM. Effects of Adult Neurogenesis on Synaptic Plasticity in the Rat Dentate Gyrus. *J Neurophysiol*. 2001;85(6):2423-2431. doi:10.1152/jn.2001.85.6.2423

64. Wu PH, Coultrap S, Pinnix C, et al. Radiation Induces Acute Alterations in Neuronal Function. Tofilon PJ, ed. *PLoS One*. 2012;7(5):e37677. doi:10.1371/journal.pone.0037677

65. Cole CJ, Josselyn SA. Transcription Regulation of Memory: CREB, CaMKIV, Fos/Jun, CBP, and SRF. In: *Learning and Memory: A Comprehensive Reference*. Elsevier; 2008:547-566. doi:10.1016/B978-012370509-9.00030-9

66. GODDYN H, LEO S, MEERT T, DHOOGE R. Differences in behavioural test battery performance between mice with hippocampal and cerebellar lesions. *Behav Brain Res*. 2006;173(1):138-147. doi:10.1016/j.bbr.2006.06.016

67. Kazda T, Jancalek R, Pospisil P, et al. Why and how to spare the hippocampus during brain radiotherapy: the developing role of hippocampal avoidance in cranial radiotherapy. *Radiat Oncol*. 2014;9(1):139. doi:10.1186/1748-717X-9-139

68. Franklin KBJ, Paxinos G. *Paxinos and Franklin's The Mouse Brain in Stereotaxic Coordinates*.

69. Raber J, Radoslaw R, LeFevour A, et al. Radiation-Induced Cognitive Impairments Are Associated with Changes in Indicators of Hippocampal Neurogenesis. *Radiat Res*. 2004;162(1):39-47. http://www.jstor.org/stable/3581068.

70. Ibahim MJ, Crosbie JC, Yang Y, et al. An evaluation of dose equivalence between synchrotron microbeam radiation therapy and conventional broadbeam radiation using clonogenic and cell impedance assays. *PLoS One*. 2014;9(6). doi:10.1371/journal.pone.0100547

71. Priyadarshika RCU, Crosbie JC, Kumar B, Rogers PAW. Biodosimetric quantification of short-term synchrotron microbeam versus broad-beam radiation damage to mouse skin using a dermatopathological scoring system. *Br J Radiol*. 2011;84(1005):833-842. doi:10.1259/bjr/58503354

72. Zhou J, Tryggestad E, Wen Z, et al. Differentiation between glioma and radiation necrosis using molecular magnetic resonance imaging of endogenous proteins and peptides. *Nat Med*. 2011;17(1):130-134. doi:10.1038/nm.2268

73. Schültke E, Trippel M, Bräuer-Krisch E, et al. Pencilbeam Irradiation Technique for Whole Brain Radiotherapy: Technical and Biological Challenges in a Small Animal Model. Cordes N, ed. *PLoS One*. 2013;8(1):e54960. doi:10.1371/journal.pone.0054960

74. Laissue J, Blattmann H, Wagner HP, Grotzer MA, Slatkin DN. Prospects for microbeam radiation therapy of brain tumours in children to reduce neurological sequelae. *Dev Med Child Neurol*. 2007;49(8):577-581. doi:10.1111/j.1469-8749.2007.00577.x

75. Benedict PD, Schlesinger DJ, Goetsch SJ, Kavanagh BD. *Stereotactic Radiosurgery and Stereotactic Body Radiation Therapy.* CRC Press; 2014.

76. Brönnimann D, Bouchet A, Schneider C, et al. Synchrotron microbeam irradiation induces neutrophil infiltration, thrombocyte attachment and selective vascular damage in vivo. *Sci Rep*. 2016;6(September):1-10. doi:10.1038/srep33601

77. Brain Tumors in Children | American Brain Tumor Association. http://www.abta.org/adolescent-pediatric/brain-tumors-in-children.html. Accessed February 21, 2018.

78. Bartzsch S, Cummings C, Eismann S, Oelfke U. A preclinical microbeam facility with a conventional x-ray tube. *Med Phys*. 2016;43(12):6301-6308. doi:10.1118/1.4966032

79. Dilmanian FA, Zhong Z, Bacarian T, et al. Interlaced x-ray microplanar beams: a radiosurgery approach with clinical potential. *Proc Natl Acad Sci U S A*. 2006;103(25):9709-9714. doi:10.1073/pnas.0603567103

80. Deman P, Vautrin M, Edouard M, et al. Monochromatic Minibeams Radiotherapy: From Healthy Tissue-Sparing Effect Studies Toward First Experimental Glioma Bearing Rats Therapy. *Int J Radiat Oncol*. 2012;82(4):e693-e700. doi:10.1016/j.ijrobp.2011.09.013

81. Prezado Y, Deman P, Varlet P, et al. Tolerance to Dose Escalation in Minibeam Radiation Therapy Applied to Normal Rat Brain: Long-Term Clinical, Radiological and Histopathological Analysis. *Radiat Res*. 2015;184(3):314-321. doi:10.1667/RR14018.1

82. Babcock K, Sidhu N, Kundapur V, Ali K. Collimator design for experimental minibeam radiation therapy. *Med Phys*. 2011;38(4):2192-2197. doi:10.1118/1.3560425

83. Bazyar S, Inscoe CR, Benefield T, et al. Neurocognitive sparing of desktop microbeam irradiation. *Radiat Oncol*. 2017;12(1):127. doi:10.1186/s13014-017-0864-2

84. Hadsell M, Zhang J, Laganis P, et al. A first generation compact microbeam radiation therapy system based on carbon nanotube X-ray technology. *Appl Phys Lett*. 2013;103(18):183505. doi:10.1063/1.4826587

85. Clinical conditions. http://www.radiustech.it/upld/catalogo/doc/Xstrahl_Medical_200_300_LR.pdf. Accessed February 22, 2018.

86. Poludniowski GG, Evans PM. Calculation of x-ray spectra emerging from an x-ray tube. Part I. Electron penetration characteristics in x-ray targets. *Med Phys*. 2007;34(6Part1):2164-2174. doi:10.1118/1.2734725

87. Poludniowski GG. Calculation of x-ray spectra emerging from an x-ray tube. Part II. X-ray production and filtration in x-ray targets. *Med Phys*. 2007;34(6Part1):2175-2186. doi:10.1118/1.2734726

88. Poludniowski G, Landry G, DeBlois F, Evans PM, Verhaegen F. SpekCalc: a program to calculate photon spectra from tungsten anode x-ray tubes. *Phys Med Biol*. 2009;54(19):N433-N438. doi:10.1088/0031-9155/54/19/N01

89. GAFCHROMIC™ DOSIMETRY MEDIA TYPE MD-V3. http://www.gafchromic.com/documents/gafchromic-mdv3.pdf. Accessed February 22, 2018.

90. Efficient Protocols for Accurate Radiochromic Film Calibration and Dosimetry. http://www.gafchromic.com/documents/Efficient Protocols for Calibration and Dosimetry.pdf. Accessed February 22, 2018.

91. Ma C-M, Coffey CW, Dewerd LA, et al. AAPM protocol for 40–300 kV x-ray beam dosimetry in radiotherapy and radiobiology. doi:10.1118/1.1374247

92. Dilmanian FA, Zhong Z, Bacarian T, et al. Interlaced x-ray microplanar beams: A radiosurgery approach with clinical potential. *Proc Natl Acad Sci*. 2006;103(25):9709-9714. doi:10.1073/pnas.0603567103

93. Prezado Y, Thengumpallil S, Renier M, Bravin A. X-ray energy optimization in minibeam radiation therapy. *Med Phys*. 2009;36(11):4897-4902. doi:10.1118/1.3232000

94. Siegbahn EA, Stepanek J, Bräuer-Krisch E, Bravin A. Determination of dosimetrical quantities used in microbeam radiation therapy (MRT) with Monte Carlo simulations. *Med Phys*. 2006;33(9):3248-3259. doi:10.1118/1.2229422

95. Gokeri G, Kocar C, Tombakoglu M. Monte Carlo simulation of microbeam radiation therapy with an interlaced irradiation geometry and an Au contrast agent in a realistic head phantom. *Phys Med Biol*. 2010;55(24):7469. doi:10.1088/0031-9155/55/24/006

96. Laissue J, Blattmann H, Wagner HP, Grotzer MA, Slatkin DN. Prospects for microbeam radiation therapy of brain tumours in children to reduce neurological sequelae. *Dev Med Child Neurol*. 2007;49(8):577-581. doi:10.1111/j.1469-8749.2007.00577.x

97. Serduc R, Vérant P, Vial J-C, et al. In vivo two-photon microscopy study of short-term effects of microbeam irradiation on normal mouse brain microvasculature. *Int J Radiat Oncol*. 2006;64(5):1519-1527. doi:10.1016/j.ijrobp.2005.11.047

98. Yuan H, Zhang L, Frank JE, et al. Treating Brain Tumor with Microbeam Radiation Generated by a Compact Carbon-Nanotube-Based Irradiator: Initial Radiation Efficacy Study. *Radiat Res*. 2015;184(3):322-333. doi:10.1667/RR13919.1

99. Zhang L, Yuan H, Inscoe C, et al. Nanotube x-ray for cancer therapy: a compact microbeam radiation therapy system for brain tumor treatment. *Expert Rev Anticancer Ther*. 2014;14(12):1411-1418. doi:10.1586/14737140.2014.978293

100. Ibahim MJ, Crosbie JC, Yang Y, et al. An Evaluation of Dose Equivalence between Synchrotron Microbeam Radiation Therapy and Conventional Broadbeam Radiation Using Clonogenic and Cell Impedance Assays. Jagetia GC, ed. *PLoS One*. 2014;9(6):e100547. doi:10.1371/journal.pone.0100547

101. Vitucci M, Karpinich NO, Bash RE, et al. Cooperativity between MAPK and PI3K signaling activation is required for glioblastoma pathogenesis. *Neuro Oncol*. 2013;15(10):1317-1329. doi:10.1093/neuonc/not084

102. Franken NAP, Rodermond HM, Stap J, Haveman J, van Bree C. Clonogenic assay of cells in vitro. *Nat Protoc*. 2006;1(5):2315-2319. doi:10.1038/nprot.2006.339

103. Hall, E J; Giassia AJ. *Radiobiology for the Radiologist*. Vol 66. Elsevier; 2006. doi:10.1016/j.ijrobp.2006.06.027

104. Pommier P, Gomez F, Sunyach MP, D'Hombres A, Carrie C, Montbarbon X. Phase III randomized trial of Calendula officinalis compared with trolamine for the prevention of acute dermatitis during irradiation for breast cancer. *J Clin Oncol*. 2004;22(8):1447-1453. doi:10.1200/JCO.2004.07.063

105. Ryan JL. Ionizing Radiation: The Good, the Bad, and the Ugly. *J Invest Dermatol*. 2012;132(3):985-993. doi:10.1038/JID.2011.411

106. Serduc R, Vérant P, Vial J-C, et al. In vivo two-photon microscopy study of short-term effects of microbeam irradiation on normal mouse brain microvasculature. *Int J Radiat Oncol*. 2006;64(5):1519-1527. doi:10.1016/j.ijrobp.2005.11.047

107. Mukumoto N, Nakayama M, Akasaka H, et al. Sparing of tissue by using micro-slit-

beam radiation therapy reduces neurotoxicity compared with broad-beam radiation therapy. *J Radiat Res*. 2017;58(1):17-23. doi:10.1093/jrr/rrw065

108. Serduc R, Bouchet A, Bräuer-Krisch E, et al. Synchrotron microbeam radiation therapy for rat brain tumor palliation-influence of the microbeam width at constant valley dose. *Phys Med Biol*. 2009;54(21):6711-6724. doi:10.1088/0031-9155/54/21/017

109. Prezado Y, Dos Santos M, Gonzalez W, et al. Transfer of Minibeam Radiation Therapy into a cost-effective equipment for radiobiological studies: a proof of concept. *Sci Rep*. 2017;7(1):17295. doi:10.1038/s41598-017-17543-3

110. Overwijk WW, Restifo NP. B16 as a Mouse Model for Human Melanoma. *Curr Protoc Immunol*. 2001;CHAPTER:Unit-20.1. doi:10.1002/0471142735.im2001s39

111. Twyman-Saint Victor C, Rech AJ, Maity A, et al. Radiation and dual checkpoint blockade activate non-redundant immune mechanisms in cancer. *Nature*. 2015;520(7547):373-377. doi:10.1038/nature14292

112. Sprung CN, Yang Y, Forrester HB, et al. Genome-Wide Transcription Responses to Synchrotron Microbeam Radiotherapy. *Radiat Res*. 2012;178(4):249-259. doi:10.1667/RR2885.1

113. Hanahan D, Weinberg RA. Hallmarks of cancer: the next generation. *Cell*. 2011;144(5):646-674. doi:10.1016/j.cell.2011.02.013

114. de Jong JMH, Schuurhuis DH, Ioan-Facsinay A, et al. Dendritic cells, but not macrophages or B cells, activate major histocompatibility complex class II-restricted CD4+ T cells upon immune-complex uptake in vivo. *Immunology*. 2006;119(4):499-506. doi:10.1111/j.1365-2567.2006.02464.x

115. Hume DA. Macrophages as APC and the dendritic cell myth. *J Immunol*. 2008;181(9):5829-5835. doi:10.4049/JIMMUNOL.181.9.5829

116. Dunn GP, Old LJ, Schreiber RD. The Immunobiology of Cancer Immunosurveillance and Immunoediting. *Immunity*. 2004;21(2):137-148. doi:10.1016/j.immuni.2004.07.017

117. Lumniczky K, Sáfrány G. The impact of radiation therapy on the antitumor immunity: Local effects and systemic consequences. *Cancer Lett*. 2015;356(1):114-125. doi:10.1016/j.canlet.2013.08.024

118. Rabinovich GA, Gabrilovich D, Sotomayor EM. Immunosuppressive Strategies that are Mediated by Tumor Cells. *Annu Rev Immunol*. 2007;25(1):267-296. doi:10.1146/annurev.immunol.25.022106.141609

119. Kusmartsev S, Gabrilovich DI. Role Of Immature Myeloid Cells in Mechanisms of Immune Evasion In Cancer. *Cancer Immunol Immunother*. 2006;55(3):237-245. doi:10.1007/s00262-005-0048-z

120. Trowell OA. The sensitivity of lymphocytes to ionising radiation. *J Pathol Bacteriol*. 1952;64(4):687-704. doi:10.1002/path.1700640403

121. Reits EA, Hodge JW, Herberts CA, et al. Radiation modulates the peptide repertoire, enhances MHC class I expression, and induces successful antitumor immunotherapy. *J Exp Med*. 2006;203(5):1259-1271. doi:10.1084/jem.20052494

122. Hauser SH, Calorini L, Wazer DE, Gattoni-Celli S. Radiation-enhanced expression of major histocompatibility complex class I antigen H-2Db in B16 melanoma cells. *Cancer Res*. 1993;53(8):1952-1955. http://www.ncbi.nlm.nih.gov/pubmed/8467514. Accessed March 3, 2018.

123. Santin AD, Rose GS, Hiserodt JC, et al. Effects of cytokines combined with high-dose gamma irradiation on the expression of major histocompatibility complex molecules and intercellular adhesion molecule-1 in human ovarian cancers. *Int J Cancer*. 1996;65(5):688-694. doi:10.1002/(SICI)1097-0215(19960301)65:5<688::AID-IJC21>3.0.CO;2-2

124. Santin AD, Hermonat PL, Hiserodt JC, et al. Effects of irradiation on the expression of major histocompatibility complex class I antigen and adhesion costimulation molecules ICAM-1 in human cervical cancer. *Int J Radiat Oncol Biol Phys*. 1997;39(3):737-742. http://www.ncbi.nlm.nih.gov/pubmed/9336157. Accessed March 3, 2018.

125. Lugade AA, Sorensen EW, Gerber SA, Moran JP, Frelinger JG, Lord EM. Radiation-induced IFN-gamma production within the tumor microenvironment influences antitumor immunity. *J Immunol*. 2008;180(5):3132-3139. http://www.ncbi.nlm.nih.gov/pubmed/18292536. Accessed March 4, 2018.

126. Mantel F, Frey B, Haslinger S, et al. Combination of Ionising Irradiation and Hyperthermia Activates Programmed Apoptotic and Necrotic Cell Death Pathways in Human Colorectal Carcinoma Cells. *Strahlentherapie und Onkol*. 2010;186(11):587-599. doi:10.1007/s00066-010-2154-x

127. Mole RH. Whole Body Irradiation—Radiobiology or Medicine? *Br J Radiol*. 1953;26(305):234-241. doi:10.1259/0007-1285-26-305-234

128. Kargiotis O, Geka A, Rao JS, Kyritsis AP. Effects of irradiation on tumor cell survival, invasion and angiogenesis. *J Neurooncol*. 2010;100(3):323-338. doi:10.1007/s11060-010-0199-4

129. Merrick A, Errington F, Milward K, et al. Immunosuppressive effects of radiation on human dendritic cells: reduced IL-12 production on activation and impairment of naive T-cell priming. *Br J Cancer*. 2005;92(8):1450-1458. doi:10.1038/sj.bjc.6602518

130. Tsai C-S, Chen F-H, Wang C-C, et al. Macrophages From Irradiated Tumors Express Higher Levels of iNOS, Arginase-I and COX-2, and Promote Tumor Growth. *Int J Radiat Oncol*. 2007;68(2):499-507. doi:10.1016/j.ijrobp.2007.01.041

131. Beyer C, Stearns NA, Giessl A, Distler JH, Schett G, Pisetsky DS. The extracellular release of DNA and HMGB1 from Jurkat T cells during *in vitro* necrotic cell death. *Innate Immun*. 2012;18(5):727-737. doi:10.1177/1753425912437981

132. Rubner Y, Wunderlich R, Rühle P-F, et al. How does ionizing irradiation contribute to the induction of anti-tumor immunity? *Front Oncol*. 2012;2:75. doi:10.3389/fonc.2012.00075

133. Rubner Y, Wunderlich R, Rühle P-F, et al. How does ionizing irradiation contribute to the induction of anti-tumor immunity? *Mol Cell Oncol*. 2012;2:75. doi:10.3389/fonc.2012.00075

134. Lee Y, Auh SL, Wang Y, et al. Therapeutic effects of ablative radiation on local tumor require CD8+ T cells: changing strategies for cancer treatment. *Blood*. 2009;114(3):589-595. doi:10.1182/blood-2009-02-206870

135. Yang Y, Crosbie JC, Paiva P, Ibahim M, Stevenson A, Rogers PAW. In Vitro Study of Genes and Molecular Pathways Differentially Regulated by Synchrotron Microbeam Radiotherapy. *Radiat Res*. 2014;182(6):626-639. doi:10.1667/RR13778.1

136. Bouchet A, Serduc R, Laissue JA, Djonov V. Effects of microbeam radiation therapy on normal and tumoral blood vessels. *Phys Medica*. 2015;31(6):634-641. doi:10.1016/j.ejmp.2015.04.014

137. Bazyar S, Inscoe CR, O'Brien III ET, Zhou OZ, Lee YZ. Minibeam radiotherapy with small animal irradiators; <i>in-vitro</i> and <i>in-vivo</i> feasibility studies. *Phys Med Biol*. 2017;62(23):8924-8942. doi:10.1088/1361-6560/aa926b

138. Dewan MZ, Galloway AE, Kawashima N, et al. Fractionated but not single-dose radiotherapy induces an immune-mediated abscopal effect when combined with anti-CTLA-4 antibody. *Clin Cancer Res*. 2009;15(17):5379-5388. doi:10.1158/1078-0432.CCR-09-0265

139. Fernandez-Palomo C, Schültke E, Smith R, et al. Bystander effects in tumor-free and tumor-bearing rat brains following irradiation by synchrotron X-rays. *Int J Radiat Biol*. 2013;89(6):445-453. doi:10.3109/09553002.2013.766770

140. Correa DD, Shi W, Abrey LE, et al. Cognitive functions in primary CNS lymphoma after single or combined modality regimens. *Neuro Oncol*. 2012;14(1):101-108. doi:10.1093/neuonc/nor186

141. Klein M, Heimans JJ, Aaronson NK, et al. Effect of radiotherapy and other treatment-related factors on mid-term to long-term cognitive sequelae in low-grade gliomas: a comparative study. *Lancet (London, England)*. 2002;360(9343):1361-1368. http://www.ncbi.nlm.nih.gov/pubmed/12423981. Accessed February 21, 2018.

142. Schültke E, Juurlink BHJ, Ataelmannan K, et al. Memory and survival after microbeam

radiation therapy. *Eur J Radiol*. 2008;68(3, Supplement):S142-S146. doi:10.1016/j.ejrad.2008.04.051

143. Welzel G, Fleckenstein K, Mai SK, Hermann B, Kraus-Tiefenbacher U, Wenz F. Acute neurocognitive impairment during cranial radiation therapy in patients with intracranial tumors. *Strahlentherapie und Onkol*. 2008;184(12):647-654. doi:10.1007/s00066-008-1830-6

144. Martišíková M, Ackermann B, Jäkel O. Analysis of uncertainties in Gafchromic® EBT film dosimetry of photon beams. *Phys Med Biol*. 2008;53(24):7013-7027. doi:10.1088/0031-9155/53/24/001

145. Bouchard H, Lacroix F, Beaudoin G, Carrier J-F, Kawrakow I. On the characterization and uncertainty analysis of radiochromic film dosimetry. *Med Phys*. 2009;36(6Part1):1931-1946. doi:10.1118/1.3121488

146. DeWerd LA, Ibbott GS, Meigooni AS, et al. A dosimetric uncertainty analysis for photon-emitting brachytherapy sources: Report of AAPM Task Group No. 138 and GEC-ESTRO. *Med Phys*. 2011;38(2):782-801. doi:10.1118/1.3533720

147. Palmer AL, Bradley DA, Nisbet A. Evaluation and mitigation of potential errors in radiochromic film dosimetry due to film curvature at scanning. *J Appl Clin Med Phys*. 2015;16(2):425-431. doi:10.1120/jacmp.v16i2.5141

148. Tello VM, Tailor RC, Hanson WF. How water equivalent are water-equivalent solid materials for output calibration of photon and electron beams? *Med Phys*. 1995;22(7):1177-1189. doi:10.1118/1.597613

149. Yamada S, Miyazaki M, Yamashita Y, et al. Influence of respiration on cerebrospinal fluid movement using magnetic resonance spin labeling. *Fluids Barriers CNS*. 2013;10(1):36. doi:10.1186/2045-8118-10-36

150. Serduc R, Bräuer-Krisch E, Siegbahn EA, et al. High-Precision Radiosurgical Dose Delivery by Interlaced Microbeam Arrays of High-Flux Low-Energy Synchrotron X-Rays. *PLoS One*. 2010;5(2):e9028. doi:10.1371/journal.pone.0009028

151. Dilmanian FA, Zhong Z, Bacarian T, et al. Interlaced x-ray microplanar beams: A radiosurgery approach with clinical potential. *Proc Natl Acad Sci*. 2006;103(25):9709-9714. doi:10.1073/pnas.0603567103

152. Bräuer-Krisch E, Requardt H, Régnard P, et al. New irradiation geometry for microbeam radiation therapy. *Phys Med Biol*. 2005;50(13):3103. doi:10.1088/0031-9155/50/13/009

153. Xu D, Gu P, Pan P-Y, Li Q, Sato AI, Chen S-H. NK and CD8+ T cell-mediated eradication of poorly immunogenic B16-F10 melanoma by the combined action of IL-12 gene therapy and 4-1BB costimulation. *Int J Cancer*. 2004;109(4):499-506. doi:10.1002/ijc.11696

154. Ugurel S, Röhmel J, Ascierto PA, et al. Survival of patients with advanced metastatic melanoma: the impact of novel therapies–update 2017. *Eur J Cancer*. 2017;83:247-257. doi:10.1016/j.ejca.2017.06.028

155. Hellmann MD, Rizvi NA, Goldman JW, et al. Nivolumab plus ipilimumab as first-line treatment for advanced non-small-cell lung cancer (CheckMate 012): results of an open-label, phase 1, multicohort study. *Lancet Oncol*. 2017;18(1):31-41. doi:10.1016/S1470-2045(16)30624-6

156. Reck M, Rodríguez-Abreu D, Robinson AG, et al. Pembrolizumab versus Chemotherapy for PD-L1–Positive Non–Small-Cell Lung Cancer. *N Engl J Med*. 2016;375(19):1823-1833. doi:10.1056/NEJMoa1606774

157. Wolchok JD, Chiarion-Sileni V, Gonzalez R, et al. Efficacy and safety results from a phase III trial of nivolumab (NIVO) alone or combined with ipilimumab (IPI) versus IPI alone in treatment-naive patients (pts) with advanced melanoma (MEL) (CheckMate 067). *J Clin Oncol*. 2015;33(18_suppl):LBA1-LBA1. doi:10.1200/jco.2015.33.18_suppl.lba1

158. Lumniczky K, Sáfrány G. The impact of radiation therapy on the antitumor immunity: Local effects and systemic consequences. *Cancer Lett*. 2015;356(1):114-125. doi:10.1016/j.canlet.2013.08.024

159. Patel KR, Lawson DH, Kudchadkar RR, et al. Two heads better than one? Ipilimumab immunotherapy and radiation therapy for melanoma brain metastases. *Neuro Oncol*. 2015;17(10):1312-1321. doi:10.1093/neuonc/nov093

160. Sharabi AB, Lim M, DeWeese TL, Drake CG. Radiation and checkpoint blockade immunotherapy: radiosensitisation and potential mechanisms of synergy. *Lancet Oncol*. 2015;16(13):e498-e509. doi:10.1016/S1470-2045(15)00007-8

161. Demaria S, Golden EB, Formenti SC. Role of Local Radiation Therapy in Cancer Immunotherapy. *JAMA Oncol*. 2015;1(9):1325. doi:10.1001/jamaoncol.2015.2756

162. Larson SM, Carrasquillo JA, Cheung N-K V., Press OW. Radioimmunotherapy of human tumours. *Nat Rev Cancer*. 2015;15(6):347-360. doi:10.1038/nrc3925

163. Reynders K, Illidge T, Siva S, Chang JY, De Ruysscher D. The abscopal effect of local radiotherapy: using immunotherapy to make a rare event clinically relevant. *Cancer Treat Rev*. 2015;41(6):503-510. doi:10.1016/j.ctrv.2015.03.011